Non-destructive testing and mechanical characterization of thermosetting polymers used in pipeline rehabilitation

Fraunhofer IZFP

Dissertation

zur Erlangung des Grades

des Doktors der Ingenieurwissenschaften

der Naturwissenschaftlich-Technischen Fakultät

der Universität des Saarlandes

von

Maryam Manavipour, M.Sc.

Saarbrücken

2018

Tag des Kolloquiums:	17.09.2018
Dekan:	Prof. Dr. rer. nat. Guido Kickelbick
Berichterstatter:	Prof. Dr.-Ing. Christian Boller
	Prof. Dr. rer. nat. habil. Marc Kreutzbruck
Vorsitz:	Prof. Dr. mont. Christian Motz
Akad. Mitarbeiter:	Dr.-Ing. Sebastian Suárez Vallejo

Preface

This dissertation is being submitted for the degree of Doctor of Engineering at Saarland University. The work described in this document was carried out between July 2011 and June 2018 under the supervision of Prof. Dr.-Ing. Christian Boller in the department of Non-Destructive Testing and Quality Assurance.

To the best of my knowledge the work described in this dissertation is original, except where reference has been made to the work of others, and has not been submitted, in part or entirety, for any degree or qualification at any other university.

Maryam Manavipour
Saarland University
September 2018

Acknowledgment

I am most indebted to Prof. Dr. Ing. Christian Boller for giving me the opportunity to start my graduation. I am very grateful for his endless support and guidance for both technical and non-technical issues. I would like to gratefully acknowledge my supervisors Dr. Klaus Szielasko and Dr. Jochen Kurz for their enthusiastic supervision, consistent support, advice, and managing.

I acknowledge the help of Dr. Christoph Sklarczyk for his technical support, relevant discussion, and general advice. Special thanks to Prof. Dr. Christian Motz and the department of Materials Science and Methods for supporting me and performing the Nanoindentation measurements.

I appreciate Prof. Dr. rer. nat. habil. Marc Kreutzbruck for serving on my review committee.

Furthermore, I would like to thank my colleagues and friends at the Fraunhofer Institute for Nondestructive Testing IZFP, especially Christopher Stumm, Martin Kurras, Fabian Weber, Dietmar Bruche, Rosemarie Bettinger and Prof. Dr.-Ing Ute Rabe for creating such a splendid atmosphere for carrying on my dissertation.

My heartfelt thanks to my husband Dr. Mohammad Zamanazde, I greatly appreciate his technical help and advice, relevant discussion, continual encouragement, love and harp editorial pencil. Without his support, this thesis could not reach the end; finally, I am always indebted to my parents and my brother for their blessing, encouraging and inspiration.

Danksagung

Zuerst möchte ich Herrn Prof. Dr. Ing. Christian Boller dankbar dafür danken, dass er mir die Möglichkeit zu dieser Dissertation gab. Ich bin sehr dankbar für seine endlose Unterstützung und Anleitung in technischen und nicht-technischen Fragen. Ich möchte meinen Vorgesetzten Dr. Klaus Szielasko und Dr. Jochen Kurz für ihre engagierte Betreuung, konsequente Unterstützung, Beratung und Leitung danken.

Ebenfalls danke ich Dr. Christoph Sklarczyk für seine technische Unterstützung, die fachliche Diskussion und seine allgemeinen Ratschläge. Mein besonderer Dank gilt Prof. Dr. Christian Motz und der Abteilung Materialwissenschaft und Methoden für die Unterstützung und Durchführung der Nanoindentationsmessungen.

Des Weiteren schätze ich Prof. Dr. rer. nat. habil. Marc Kreutzbruck für seine Mitarbeit im Prüfungsausschuss.

Außerdem möchte ich mich bei meinen Kollegen und Freunden am Fraunhofer-Institut für Zerstörungsfreie Prüfverfahren bedanken, insbesondere bei Christopher Stumm, Martin Kurras, Fabian Weber, Dietmar Bruche, Rosemarie Bettinger und Prof. Dr.-Ing. Ute Rabe für die Schaffung einer so angenehmen Atmosphäre während meiner Dissertation.

Mein herzlicher Dank gilt meinem Mann Dr. Mohammad Zamanazde, für dessen technische Hilfe und Rat, seine sachdienliche Diskussion, seine ständige Ermutigung, seine Liebe und seine kritische Anmerkungen. Ohne seine Unterstützung hätte diese Arbeit nicht fertig gestellt werden können. Abschließend bin ich meinen Eltern und meinem Bruder immer für ihren Segen, ihre Ermutigung und ihre Inspiration dankbar.

List of Abbreviations

a	magnitude
A_c	contact area
AFM	atomic force microscopy
As	arsenide
ASTM	american society for testing and materials
Ave.	average
δ_a	azimuth resolution
θ_a	half width at half maximum
B_e	bandwidth of antenna
c	speed of light
c*	concentration
c_0	speed of light in vacuum
CCTV	closed-circuit television
CIPP	cured in place pipe
CW	continuous wave
D	diffusion coefficient
d	distance
D^*	transmission coefficient
D_0	frequency of collisions
d_a	length of antenna
DIC	differential interference contrast
DMA	dynamic mechanical analysis
DSC	differential scanning calorimetry
DUT	device under test
E	elastic modulus
$\bar{\mathbf{E}}$	electric field strength
$\bar{\mathbf{E}}_0$	peak value of $\bar{\mathbf{E}}$
E'	storage modulus
E''	loss modulus
$\mathbf{E_l'}$	longitudinal storage modulus
$\mathbf{E_l''}$	longitudinal loss modulus

E(t)	envelope of the time pulse
E^*	complex modulus
E_a	activation energy for the reaction
E_r'	reduced storage modulus
E_r''	reduced loss modulus
E_T	elastic modulus of indenter
E_v	spring constant
δ_e	axial resolution
f	frequency
F(t)	function of time pulse
FBH	flat bottom hole
FFT	fast Fourier transform
FTIR	Fourier transform infrared
Ga	gallium
H	hardness
h	indent displacement
H	hydrogen
H(f(t))	Hilbert transform of the time pulse
h_0	initial penetration
HWHM	half width at half maximum
i	imaginary unit
IKT	Institut für Unterirdische Infrastruktur
J	diffusion flux
k	complex propagation factor
k′	real part of propagation factor
k″	loss factor of propagation factor
K_s	storage stiffness
α^{long}	longitudinal damping
L_{sa}	length of synthetic aperture
NDT	non-destructive testing
O	oxygen
O-NPG	Ortho Neopentyl glycol resins
P	maximum applied force

PE	polyethylene
PET	polyethylene terephthalate
PMMA	polymethylmethacrylate
PU	polyurethane
R	gas constant
r_0	liftoff
RF	radio frequency
SAR	synthetic aperture radar
θ_{sa}	beamwidth of the synthetic antenna
SEM	scanning electronic microscope
SRS	Stanford research systems
t	time
T	absolute temperature
T_g	glass transition temperature
TDS	time domain spectroscopy
TGA	thermogravimetric analysis
THz	terahertz
TOF	time of flight
u	strain
u_e	elastic strain
u_{in}	viscous strain
$\mathbf{\dot{u}_{in}}$	inelastic strain rate
UP	unsaturated polyester
UPRs	unsaturated polyester resin
US	ultrasound
UV	ultraviolet
V	sound velocity
V_l	longitudinal sound velocity
VNA	vector network analyzer
V_t	transverse sound velocity
W_0	conditioned weight
W_w	wet weight
x	thickness

x^*	position
Z	impedance
δ	damping
ΔTOF	time of flight in material subtraction time of flight in air
ε	complex permittivity
ε'	real part of permittivity
ε''	loss factor of permittivity
ε_0	permittivity in vacuum
ε_r	relative permittivity
ζ	characteristic of asymptotic regime
η_v	viscoelasticity
θ	phase
λ	wavelength
μ	permeability
μ_0	permeability in vacuum
μ_r	relative permeability
ρ	density
σ	stress
σ_e	stress applied to the spring
σ_{in}	stress applied to the dashpot
τ	characteristic time
υ	Poisson's ratio
υ_T	Poisson's ratio of indenter
ω	angular frequency
ωC_s	loss stiffness
Γ	reflection coefficient

List of contents

List of tables

Abstract

Cured in place pipe (CIPP) is one of the trenchless methods of pipe rehabilitation, by inserting a new polymeric liner inside the host pipe. Different abnormalities may occur during manufacturing, curing, inserting and operation in CIPP, which may reduce its efficiency; therefore regular inspection is necessary. Nowadays these inspections are only through destructive methods. In this thesis, the non-destructive testing (NDT) is applied, such as microwaves, terahertz and ultrasound immersion techniques for investigation these abnormalities.

As the CIPP is exposed to water after installation, the effect of hydrothermal aging was investigated here. The aging was performed by immersion of CIPP samples in double distilled water at 65 °C until the samples get saturated. The saturation process was controlled through weighing. The inspection of aging was performed via comparison of optical microscopic images before and after aging and also through nanoindentation tests. It was shown that the mechanical aging is the reason of the mechanical properties degradation. Moreover, microwaves and terahertz techniques could distinguish aged samples from the unaged ones. These methods and ultrasound technique could detect the insufficient curing and geometrical defects in CIPP. Besides, the thickness measurement through these methods was possible.

In summary NDT has a good outlook for analysis of CIPP and in the future it can be an alternative to destructive testing in this region.

Zusammenfassung

Cured in place pipe (CIPP) ist eine Rohrsanierungsmethode, bei der ein Polymerschlauch in das Altrohr eingeführt wird. Bei der Herstellung, Aushärtung, Einbringung und dem Betrieb von CIPP können verschiedene Auffälligkeiten auftreten, die die Effizienz von CIPP beeinträchtigen können und eine regelmäßige Überprüfung erforderlich machen. Heutzutage werden diese Inspektionen nur mit zerstörenden Methoden durchgeführt. In dieser Arbeit wurden zerstörungsfreie Methoden (ZfP) wie Mikrowellen, Terahertz und Ultraschall eingesetzt, um solche Auffälligkeiten zu untersuchen.

Da das CIPP nach der Installation Wasser ausgesetzt ist, wurden in dieser Arbeit unter anderem die Effekte der Alterung untersucht. Die hydrothermale Alterung erfolgte durch Eintauchen der CIPP-Proben in doppelt destilliertem Wasser bei 65 °C, um die Proben vollständig mit Wasser zu sättigen. Dieser Prozess wurde durch Wägen überprüft. Die Untersuchung der Alterung erfolgte durch Vergleich ihrer lichtmikroskopischen Bilder vor und nach der Alterung sowie durch Nanoindentationstests. Hierdurch konnte gezeigt werden, dass die mechanische Alterung der Grund für die Verschlechterung der mechanischen Eigenschaften ist. Terahertz- und Mikrowellenverfahren konnten die gealterten Proben von nicht gealterten Proben unterscheiden. Außerdem waren die Dickenmessung, der Nachweis der unzureichenden Aushärtung und der geometrischen Defekte im CIPP mittels dieser Techniken und dem Ultraschallverfahren möglich.

1 Introduction

1.1 Renewal systems of sewer pipelines

Buried pipelines may exhibit damage after a while because of pressure, corrosion, aging, erosion, etc.. The renewal process of pipes, regardless of their material and damage can be divided into replacement, repair and rehabilitation.

- **Replacement**

Replacement means exchanging the existing pipe with a new pipe. The new pipe offers a new canal that does not depend on the existing pipe for its structural performance [Allouche 2012; Sokoll 2009].

- **Repair**

Repair of sewer pipelines can result from gradual deterioration in localized areas of the sewer line, external damage or other unexpected and rapid deterioration of conditions within the sewer. The goal of repair actions is either to restore the sewer to an operating condition or to deal with localized deterioration. The main difference between repair and rehabilitation is that repair is temporary until a more complete rehabilitation or replacement can be carried out.

Repair of a damaged section or a failure of pipes usually focuses on taking only remedial action for one or two sections of the pipe. This solution is often in emergency conditions and then will be completed with rehabilitation [Allouche 2012; Sokoll 2009].

- **Rehabilitation**

Pipeline sewers rehabilitation represents a more extensive or deliberate effort to renew portions of a sewerage system. The focus of this discussion is on techniques that can be carried out without any trenching to expose the sewer line. As shown in Fig. 1, various rehabilitation methods could be used [Allouche 2012; Sokoll 2009].

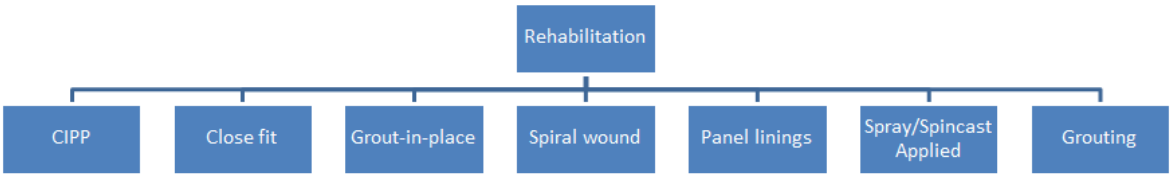

Fig. 1: Rehabilitation approaches for sewer pipelines

These trenchless methods are frequently used to rehabilitate deteriorated sewer mains, seal leaky joints, cracks and to repair service laterals [Manavipour 2014].

Cured in place pipe (CIPP) is a member of the family of trenchless rehabilitation methods that enables the renewal of a buried pipe without a full excavation of the ground. CIPP are mainly thermosetting

polymers, which are inserted into the host pipe by pulled in place method or by inverting method under water or air pressure when the resin is flexible. After that they will be cured in the pipe. Therefore it is named “cured in place pipe” [Matthews 2018]. Fig. 2 shows a CIPP liner during installation.

Fig. 2: Installation of CIPP in pipeline through pulled in place [Dilg 2007]

A project of CIPP includes a diversity of investigative, design, planning and execution phases. When a pipeline has been identified as needing rehabilitation, it is necessary to find out if the CIPP process is a suitable candidate for rehabilitation. CIPP is generally available in diameters of 0.1 to 3 m [Matthews 2011].

1.1.1 Historical background of cured in place pipe

The first known use of a CIPP lining was carried out in 1971 in the relining of 70 m length of the Marsh Lane Sewer in Hackney, East London. This 100 years old brick egg-shaped sewer had dimensions of 1.175 m×0.610 m (height × middle width).

Eric Wood, the inventor of this method, was supported by entrepreneurs Doug Chick and Brian Chandler. Following a successful trial, they established the company Insituform Pipes and Structures, Ltd. and continued to market the technology and made improvements in the materials, preparation and application of the technology [Allouche 2012].

1.1.2 Cured in place pipe materials

CIPP consists of two main parts: tube construction and resin.

Tube construction: CIPP tube construction makes of needled polyester felt, which serves only as a carrier for the resin. It means, the resin is the dominant contributor to the mechanical properties of the

system. Other forms of tube construction entered the marketplace in the U.S. during the 1990s. They involved inclusion of reinforcing materials such as fiberglass, aramid fibers or carbon fibers in some configuration. The reinforcement positions at selected points within the thickness of the tube wall or the wall may consist primarily of braided reinforcing layer(s). The needled felt tube is most commonly made of a non-woven needled felt fabricated with polyester fibers. The non-woven felt has little reinforcing capability. Therefore, the strength of a CIPP liner can be increased by using fiber-reinforced CIPP and woven CIPP [Westaway 2001; Zhao 2005].

Resin: There are three types of thermoset resins, which are well suited for usage in CIPP applications. These are unsaturated polyester (UP), vinyl ester and epoxy resins.

The most commonly used resin is UP, which is convenient and economic for most normal applications additionally it has good corrosion resistance to normal sewage conditions. Isophthalic polyester resins, used in more than 80% of the CIPP market worldwide, are the most frequently used type of unsaturated polyester resins (UPRs). These resins are usually with average value of reactivity, rigid, and corrosion-grade with a high viscosity when compared to standard laminating resins. They normally contain fumed silica to help prevent resin drainage from the upper portion of the CIPP during the curing process. Due to their lower cost in comparison with vinyl ester and epoxy resins and an acceptable level of water tightness and chemical resistance, they are a suitable choice for most municipal sewer applications. Iso-polyesters impregnate CIPP materials can be cured even when ambient temperatures drop to near or below the freezing point [Matthews 2011].

One of the other types of polyester resins used in CIPP is polyester resin based on terephthalic acid. It has higher tensile toughness and a higher heat distortion temperature than standard polyester resins. But their production requires higher processing temperatures, pressures and cycle times, which make it more expensive. Another type of polyester resin is orthophthalic anhydride, which has been used in Europe. Because this type of resin is viewed as a low quality resin choice and it is not capable of meeting the chemical resistance requirements of ASTM F1216, it is not currently used in CIPP applications in North America.

Polyester resins based on bisphenol fumarate offer outstanding resistance to caustic and oxidizing environments, applied for sewer lines requiring a high degree of chemical and temperature resistance [Allouche 2012]. Epoxy resins are also used in CIPP applications. The epoxy resins are more expensive, which is why they are mainly used in pressure pipes and potable water applications. They can also be used where it is important to avoid the release of styrene. Vinyl ester resins are typically used in harsh environment, which need improved chemical and temperature resistance. They can provide better initial and retained structural properties than the UPRs and they are significantly more expensive than the standard polyester resins. A less-used variant of the vinyl ester resin is a urethane-modified vinyl ester resin [Penders 2012].

In some CIPP there is a coating part, which is a sacrificial layer of polyurethane to hydrolyze over the time considered. Nowadays, diverse resistant coating layers are used such as different polyurethane (PU) or polyethylene (PE) materials [Allouche 2012; Penders 2012].

1.1.3 Installation of cured in place pipe

When the impregnated CIPP is ready, it is transported into the host pipe to be relined. In order to avoid thermal curing of CIPP during the transport to the site, they are kept in refrigerated storage or in a chilled condition [Sterling 2016].

The installation can be done either by inversion of the CIPP along the host pipe using water or air pressure or by pulling the CIPP into place and then inflating it to a close fit using water or air [Sterling 2010; Matthews 2011] (see Fig. 3).

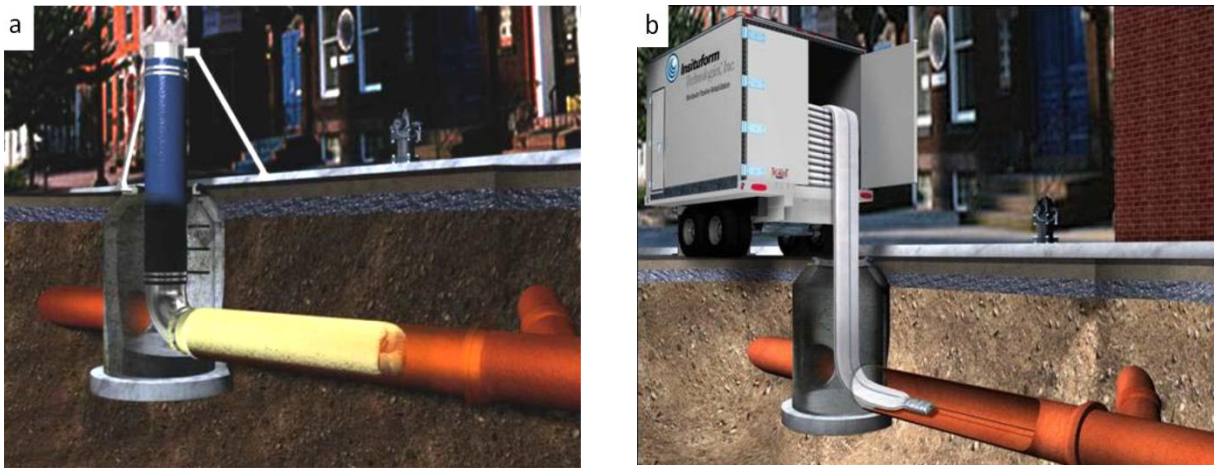

Fig. 3: CIPP Installation, a) inversion, b) pull-in [Allouche 2012]

After the uncured CIPP is in place and held tightly against the host pipe, the thermosetting polymer is cured using hot water, steam or ultraviolet (UV) light causing the crosslinking. The curing processes (e.g. time and temperature curves for thermal curing and UV light intensity for UV curing) are important to be certain that the full thickness of the CIPP becomes suitably cured [Matthews 2011; Sterling 2010].

In the next paragraphs, these two methods of curing will be explained in detail:

a. Thermal Curing

Thermal curing includes the use of heat via contact with hot water, steam, or hot air or also by allowing the CIPP to cure by exposure to ambient temperatures for small diameter pipes [Allouche 2012].

Hot water curing is the main curing method for CIPP and can be used for all range of host pipe diameters. Steam curing offers a more rapid cure than hot water and thus increasing the efficiency. This process increases safety issues but is only used in small to medium diameter pipes because the

evenness of curing conditions is harder to control in large diameter pipes and over long installation lengths. Since the steam has less “thermal mass” it makes the curing more risky, whereby either insufficient heat is provided to complete the curing or excess heat from the resin is not removed causing a resin to boil. Either using hot water or steam, the temperature is measured as the CIPP cures to check the exothermic reaction and to ensure complete cure of the resin [Sterling 2010].

b. UV Curing

The UV light curing is developed and used mainly for glass fiber tubes, which are impregnated with polyester or vinylester resins. The seamless CIPP has both an inner and outer film. The outer film blocks UV light. The inner film is removed after curing. The CIPP tube is winched into the existing pipe and inflated with air pressure (41.37 to 55.16 kPa) and then cured using a UV light train [Sterling 2010; Sterling 2016] (see Fig. 4).

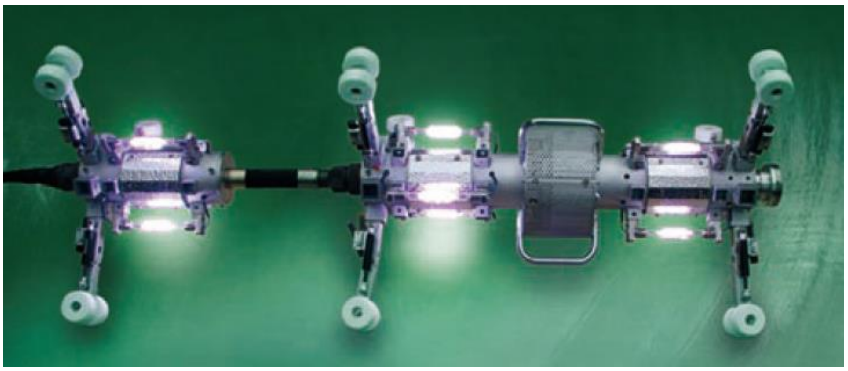

Fig. 4: UV light curing of CIPP in pipe [Dilg 2007]

1.1.4 Flaw types of cured in place pipe

Abnormalities in CIPP can be divided into different categories. In the following, some flaws are described:

I. Visible abnormalities

Wavy and folding CIPP surface, blister (Fig. 5a), cracks (Fig. 5b), discoloration, debonding or removing of the liner wall are categorized in visible abnormalities, which are detected and documented using video camera systems [Kampbell 2011].

The cracks, which make the CIPP leaky can be observed on the surface. These cracks can be inspected visually. The invisible cracks in the depth cannot be detected, although they affect the mechanical properties of CIPP [Kampbell 2011; Bosseler 2009].

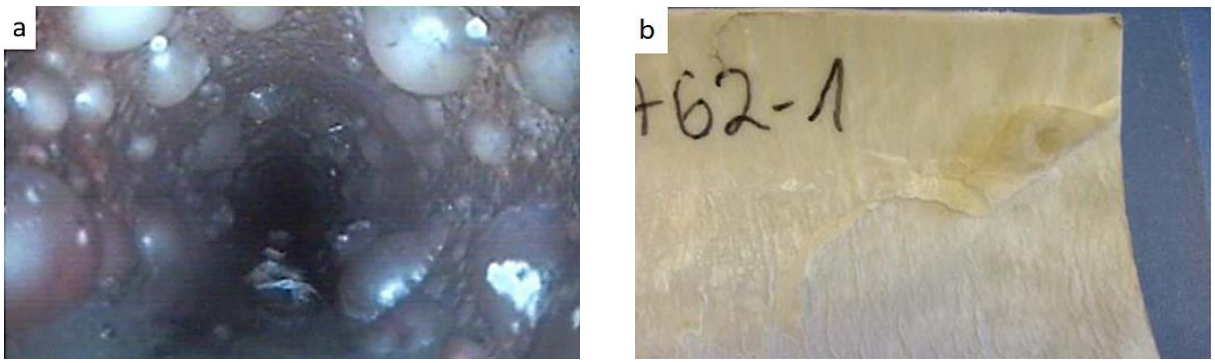

Fig. 5: Flaws on CIPP, a) blister, b) cracks on CIPP wall [Bosseler 2009]

II. Reduction of thickness

The thickness of CIPP changes during the installation and application because of various parameters e.g. curing, corrosive materials in wastewater, erosion, etc. (see Fig. 6). The reduction of the thickness is undesirable, because of the less resistance to the pressure, erosion, corrosion, etc. [Yousef 2006].

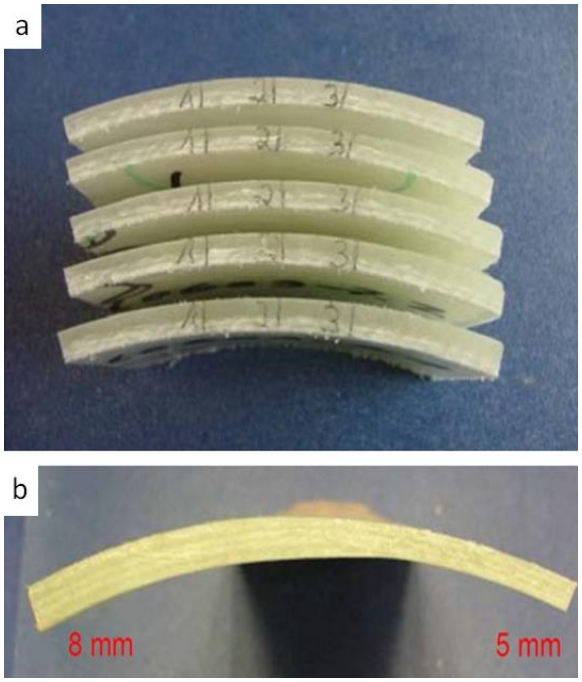

Fig. 6: a), b) Variation of CIPP thickness, which cannot be measured in situ [Bosseler 2009].

The gap between pipe and liner after curing is unavoidable. Although it is tried to calculate the suitable diameter of a CIPP according to the size of the pipe, but during the curing of liner in the pipe, since shrinkage occurs in a thermosetting polymer after crosslinking, an annular gap is unavoidable [Allouche 2014; Bakeer 2008]. Therefore it is important to measure this gap both after curing and during the inspection of the liner after some years of in service.

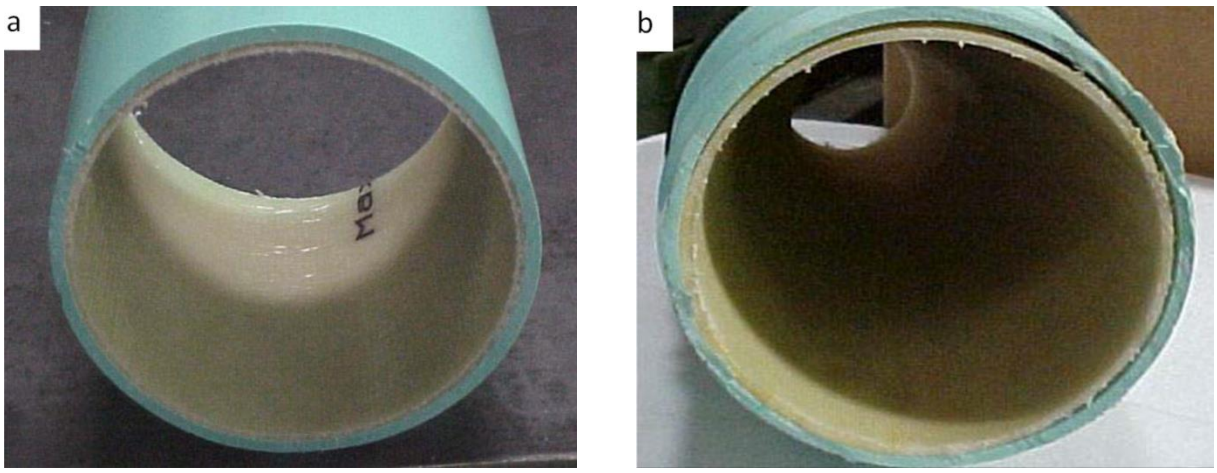

Fig. 7: Pipe segment with the CIPP, a) without annular gap, b) with annular gap [Doherty 2005]

For most cases, the space between the host pipe and the liner is either local or eccentric rather than a uniform ring. Therefore a uniform ring may not exist in CIPP installations [Bakeer 2008] (see Fig. 7, Fig. 8).

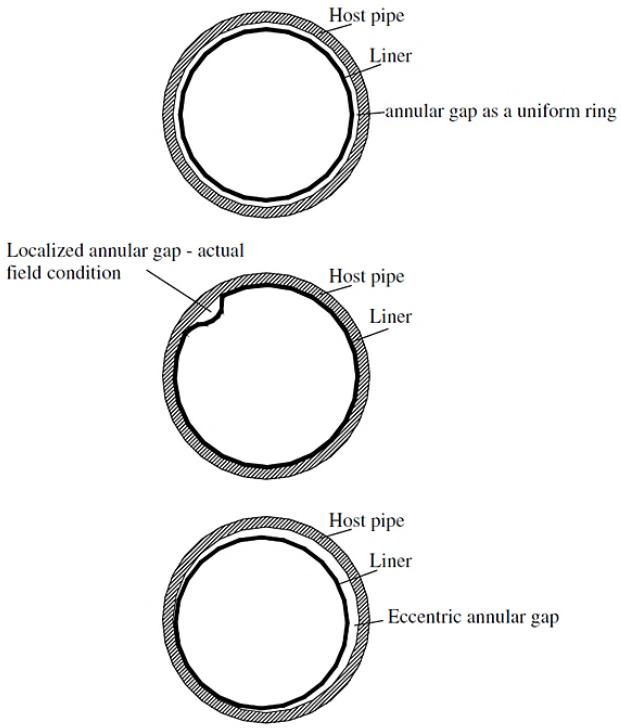

Fig. 8: Cross-section of a pipe lined (not to scale; the annular gap enlarged for the purpose of illustration)

The only way to measure the annular gap between the CIPP and the host pipe is using a caliper by removal of the host pipe plus the CIPP [Allouche 2014].

The measurement of the annular gap is of interest in liner performance because structurally, a tight liner with a small annular gap will have a better resistance to external buckling for the same thickness of the liner. It is also more likely to be locked a tight liner into place within the host pipe by negligible

irregularities and joints in the host pipe, which limits the potential longitudinal movement of the liner in the pipeline [Sterling 2010].

III. Insufficient curing

Curing insufficiently of the CIPP is rarely detected in the frame work of canal inspection. Discoloration can be a sign of this abnormality (Fig. 9). This discoloring is easier to distinguish in the laboratory in comparison to in situ. For UPR the smell of styrene is a sign of deficient curing. The insufficient curing decreases the mechanical properties, which are distinguishable through three point bending flexural tests [Penders 2012].

Fig. 9: Discoloration of liner due to insufficient curing [Bosseler 2009]

IV. Leakage

Penetration of water through the wall of CIPP with different forms e.g. drops on the wall (Fig. 10), as well as infiltration with clear detectable flow of water is possible [Allouche 2012; Penders 2012].

Fig. 10: Drops of water on the inside of the liner due to leakage [Bosseler 2009]

1.1.5 Flaw detection of cured in place pipe

The flaw detection of the CIPP nowadays is through the following methods:

i. Visual inspection

Using a closed-circuit television (CCTV) camera is not only to inspect the CIPP, but also to inspect the pipeline prior to the relining work and to find out any necessary additional measurements required (such as pipe diameter).

Most rehabilitated sections are only evaluated using CCTV immediately after the installation and then periodically using CCTV depending on the overall inspection, since in comparison to the other non-destructive techniques, this approach is cheaper. This means a regular CCTV inspection at intervals of a number of years [Allouche 2012; Sokoll 2009]. In this frame, it would be possible to detect different abnormalities such as discolored stain, blister, and local leakage. According to the size of CIPP, this inspection can be done manually or by robots [Navab-Kashani 2014].

ii. Tightness testing

In order to perform the tightness test, the interior coatings are cut and the outer films are taken away, if they exist. In three test areas with a diameter of 45±5 mm, red colored water e.g. Rhodamine B is applied on the inside surface of the liner. The outside of the liner is exposed to vacuum of 0.5 bars (Fig. 11). Samples are indicated as leaky, when the test liquid penetrates (drops, foam or moisture) at least from one test area. The laminate discoloration is permitted. The test duration is 30 minutes [Sokoll 2009].

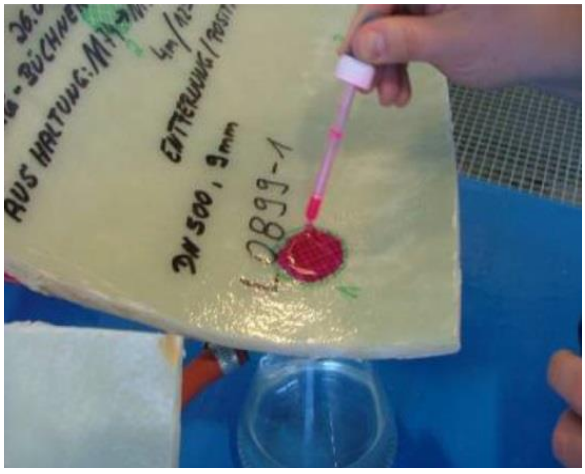

Fig. 11: Tightness testing in the IKT institute [Sokoll 2009]

iii. Three point flexural test

CIPP samples are cut from the crown, side and bottom of a liner using a router and a band saw and tested under three point flexural test according to standards DIN EN ISO 178 and DIN EN 761 as

shown in Fig. 12. The mechanical property like elastic modulus can be measured through this measurement [Allouche 2014].

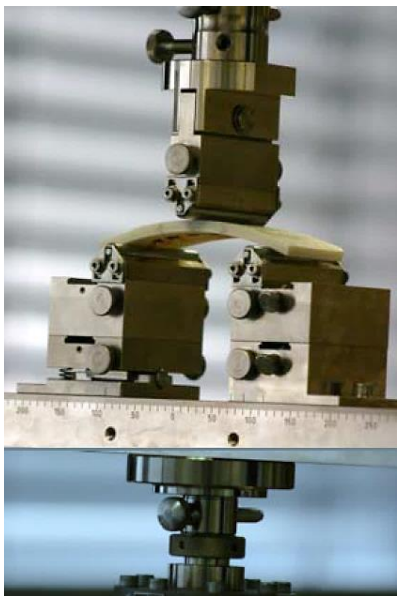

Fig. 12: Mechanical testing of three point flexural test [Muenchmeyer 2007]

iv. Thickness measurement

There is no in situ non-destructive testing (NDT) to measure the thickness of a liner. Nowadays the only applicable method carried out to measure the thickness of CIPP is using a caliper and micrometer. The ultrasonic testing equipment cannot work well on the liner field samples, because of attenuation of ultrasounds [Allouche 2012]. The results of CIPP thickness measurement through ultrasound echo test in the Institut für Unterirdische Infrastruktur (IKT) report [Sokoll 2009] are still pending and are not yet validated. In order to use a caliper, the liner sample should be cut out of the location in the pipe and tested in a laboratory (see Fig. 13). The removal place of the liner need to be repaired and filled in again either by a robot or manually [Sterling 2010].

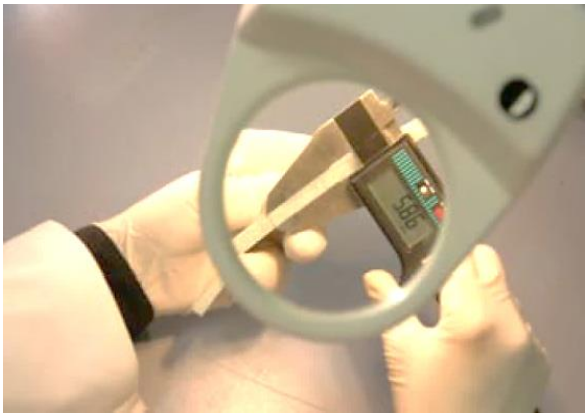

Fig. 13: Measurement of the thickness of CIPP [Muenchmeyer 2007]

v. Sample-based inspection

The sample of CIPP should be removed from the pipe depending on the location. There are two ways of sample taking. Samples from the liner in a manhole are removed manually. In the sites of the pipe, which are not accessible by hand, a cutting robot goes through the pipe and takes the sample to the manhole. It should be marked on the samples, from which part (top, bottom or the side) of the liner they are removed [Sterling 2010]. After that, the removed volume needs to be filled manually or by using a robot again (see Fig. 14).

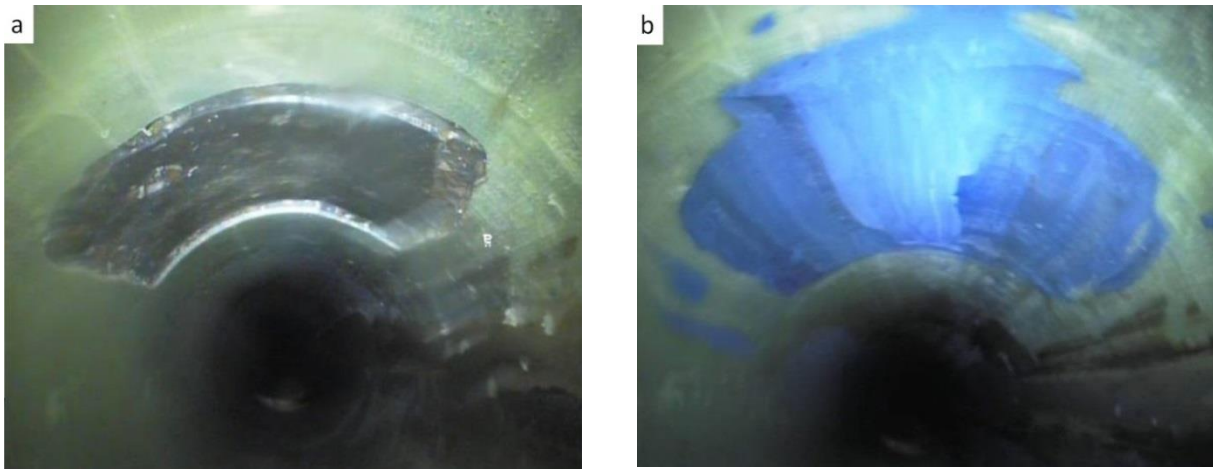

Fig. 14: Sample removal site, a) before filling, b) after filling [Sokoll 2009].

1.2 **Aging**

Since the CIPP is exposed to water and it is aged during the operation, it is necessary to investigate the aging process.

1.2.1 Types of aging

The aging process in polymer matrix composite materials is dependent on temperature. At temperatures above the glass transition temperature (T_g), molecules move rapidly where an increase or a decrease of temperature causes an increase or a decrease of volume in time in accordance to the temperature change. T_g represents the region in which the resin transforms from a hard, glassy solid to a viscous liquid. At temperatures lower than T_g, the molecules move slowly such that temperature changes are not instantly reflected by a corresponding change in the volume of the material. Therefore, there are three types of aging:

a. Chemical aging

This kind of aging relates to irreversible changes in the polymer matrix composite through mechanisms like crosslinking or chain scission. These mechanisms include thermo-oxidative, thermal

and hydrothermal aging. Crosslinking and oxidation are the dominant chemical aging mechanisms in polymer matrix composite operating temperatures. Chemical aging often leads an increase in crosslinking density. It can cause changes in material density and increase T_g, which as a result will influence the mechanical properties such as strength and stiffness [Martin 2008].

b. Physical aging

The physical aging occurs when a polymer is quickly cooled down below T_g and the material develops towards its thermodynamic equilibrium. Variations in the free volume, enthalpy, and entropy of the polymer are the results of this aging, which produces measureable changes in the mechanical properties. Physical aging is a reversible process. It means, if the polymer sets in the primary situation before the aging, the material will reach the previous physical and mechanical properties [Martin 2008].

c. Mechanical aging

Another irreversible process is mechanical degradation, which is observable also on the macroscopic scale. These aging mechanisms consist of matrix cracking, delamination, interface degradation, fiber breakage, and inelastic or plastic deformation. Hence, they have a direct effect on mechanical properties such as stiffness and strength [Martin 2008].

Hydrothermal aging on composites

In composite materials, hydrothermal aging affects the matrix through variation on chemical and physical properties, as well as the fiber/matrix interface which is the determining factor in the composites [Wang 2007]. Water enters a composite material principally by the mechanism of diffusion. Other mechanisms are possible such as capillarity along the fibers, the interface and transport by micro-cracks [Tsenoglou 2006]. Water entrance into a composite leads to plasticization of the polymer matrix and degradation of the fiber/matrix interface, which causes debonding. Plasticization is the phenomenon of diffusing a small molecule, called a plasticizer, blended with a glassy polymer results in a reduction of the T_g of the polymer and its elastic modulus. Such plasticization usually increases polymer flexibility or mobility [Wang 2007].

Furthermore, mechanical properties are sensitive to hydrothermal aging. For instance, a decrease in fracture toughness has been detected when a polymeric composite was simultaneously exposed to water and mechanical stress [Han 2003].

Indicators that are useful for tracking hydrothermal degradation are outlined below:

- *Weight changes*: Exposure to a moist environment may result in weight gain over time. For Fickian behavior, the proportion of weight gain and saturation level is proportional to relative moisture, although the time required to reach saturation is a function of temperature.
- *Physical changes*: An increase in crack density may be detected after exposure to moist environment. Anomalous weight change behavior may be noted during cyclic exposure with the time to saturation and drying shortened by orders of magnitude following micro-crack formation.
- *Mechanical properties*: The mechanical properties such as fatigue life, fracture toughness, and linear viscoelastic creep are mainly sensitive to hydrothermal degradation [Han 2003].

Plasticization:

Generally plasticization or softening, a reversible phenomenon, refers to a change in the thermal and mechanical properties of a polymer. A plasticizer has usually the desired properties of a polymer and used to have a compound that gives more extensibility, shock resistance and more flexibility by reducing elastic modulus. The principle function of the plasticizer is to be able to interpose itself between the polymer chains. Plasticization, on a molecular level, leads to increased intermolecular space or free volume, and may involve the weakening or breaking of selective interpolymer bonds. Plasticization implies intimate mixing, such that a plasticizer is dissolved in a polymer or a polymer is dissolved in a plasticizer. Efficiency of the plasticization can be measured by the lowering of T_g and also by typical dynamic mechanical properties such as decrease in fracture toughness and elastic modulus. Adding the plasticizer to the polymers will also lower the temperature at which the maximum of the damping occurs. The shift of the temperature shows the plasticizer efficiency. The temperature of the maximum damping depends on the frequency. The higher the frequency, the higher the temperature [Immergut 1965; Marais 1999].

Water is the most universal plasticizer in the world. Viscoelastic properties such as creep may also be responsive to moisture-induced degradation and can provide a good method for determining long-term influence on stiffness related degradation.

Many so called 'water-soluble' polymers, including the polymers with:

- A very high cationic charge (H-bonding), to neutralize the negative charges of the colloids
- A relatively low molecular weight, to allow rapid diffusion in the medium and around the particles (10,000 to 1,000,000 g/mol).

The plasticization by water affects the T_g of many synthetic and natural amorphous polymers (particularly at low moisture contents), and that T_g depression can be advantageous or disadvantageous to material properties, processing , and stability [Levine 1988].

Most other synthetic and natural polymers, which are more hydrophobic, less polar, or lesser H-bonders, are not highly water-soluble, but are water sensitive to some extent, especially at low moisture. For these, water is a plasticizer, but not a good solvent [Immergut 1965; Levine 1988].

Theory of diffusion

Penetration of moisture into composite materials is explained relatively by diffusion, which means transport of water molecules into the matrix and in some cases into the fibers [Bao 2002; Srivastava 1999]. Water can diffuse along the fiber–matrix interface in composites. This capillary flow prefers to occur along the interface, if wetting of the fibers by the matrix is incomplete [Tsenoglou 2006]. Crack propagation is the result of flow and storage of water in micro-cracks in the matrix through the osmotic pressure [Gautier 2000].

Consequently, it is concluded that the mechanisms of moisture penetration in composites are much more complex than in the case of the unreinforced matrix [Thomason 1995]. Composites typically absorb more water than unreinforced polymers, depending on the total volume of the polymer.

Numerous diffusion models have been proposed over the years for modeling hydrothermal effects in polymer composites. The one most frequently used model by researchers is the Fick's law, which is:

$$J = -D\frac{\partial c^*}{\partial x^*} \qquad \text{Eq. 1}$$

where

J is the diffusion flux [mol.m^{-2}/s] to measure the amount of substance that will flow through a unit area during a unit time interval,

D is the diffusion coefficient or diffusivity [m^2/s],

c* is the concentration, amount of substance per unit volume [mol/m^3], and

x* is the position [m].

Some researchers have proposed that the deviation can be explained by a two-stage Fickian process [Carter 1978; Gurtin 1979]. Others claim that the diffusion process in a composite is non-Fickian.

Higher temperatures raise the water absorption in reinforced polymers, following Fick's second law of diffusion (Eq. 2) [Christian 2012], where debonding of the fibers from the matrix is clearer and induces localized water entrapment [Lassila 2002].

$$\frac{\partial c^*}{\partial t} = D\frac{\partial^2 c^*}{\partial x^2}$$ Eq. 2

where

t is time [s].

The diffusion coefficient increases with increasing temperature according to the Arrhenius equation:

$$D = D_0 e^{-E_a/RT}$$ Eq. 3

where

D_0 is the maximal diffusion coefficient [m^2/s],

E_a is the activation energy for the reaction [$J.mol^{-1}$],

T is the absolute temperature at which diffusion is occurring [K], and

R is the universal gas constant (8.3144598 [$J.mol^{-1}.K^{-1}$]) [Christian 2012].

It is known, when moisture enters the matrix and fiber, that it can plasticize the polymer and reduce the hardness. The question being raised in this thesis is if the diffusion of water molecules deteriorates the mechanical properties of CIPP after hydrothermal aging.

1.3 **Mechanical properties of polymers**

Polymers contain long molecules which are mostly bonded covalently. At the temperatures about some few Kelvin, application of strain may cause strain of the intermolecular bond while the molecular chains are fixed in their positions [Rösler 2007]. In this situation the materials behave elastically linear and in most cases they break brittle. Increase of temperature (even at room temperature) changes the behavior of polymers due to the thermally activated rearrangements and movements within and between the chains, which are partly reversible. These processes are mainly responsible for the observed viscoelastic behavior of polymers [Ahmad 2010; Chen 2013; Cheng 2000; Dub 2008]. Viscoelastic effects can occur at temperatures well below the T_g and thus have to be considered when designing with polymers. Therefore, the time-dependency of the mechanical properties has a strong technical importance. There are two approaches for evaluation of the viscoelastic properties of materials which are as follows:

1: The strain in a specimen is kept at constant stress, after a fixed loading time is measured. This technique is called retardation.

2: The strain is kept fixed instead of the stress. In this case, the stresses decrease with time. This technique is called relaxation. It is due to the decrease of measured stress if we apply a constant strain.

For technical applications, retardation curves are usually more important because in most cases the load on the component is known and it has to be checked, whether the permissible maximum strain is exceeded. However, evaluation of the time dependency of the mechanical properties with application of constant strain is also widely used.

Fig. 15 shows the impacts of time, temperature and applied stress on the mechanical properties of polymethylmethacrylate (PMMA) with a glass transition temperature of about 100 °C. The isochronous stress-strain (σ-u) curves are taken in retardation experiments. Clearly enough, in contract to the "ordinary" σ-u curves, each value of the stress requires its own experiment. Following general conclusions could be driven based on the curves:

1: A linear viscoelastic region at small strains, with stress and strain being proportional could be observed.

2: The slope of the linear region is time-dependent in contrast to the ordinary σ- u curves. It generally decreases with increasing loading time.

3: At strains larger than approximately 0.5%, a deviation from linear behavior is observed. The material becomes non-linear viscoelastic and, at even larger strains, flow viscoplastically. If the strain is increased further, plastic behavior dominates, and the slope of the curves decreases.

4: If the loading time is increased in the viscoelastic region, the strain increases proportionally [Rösler 2007].

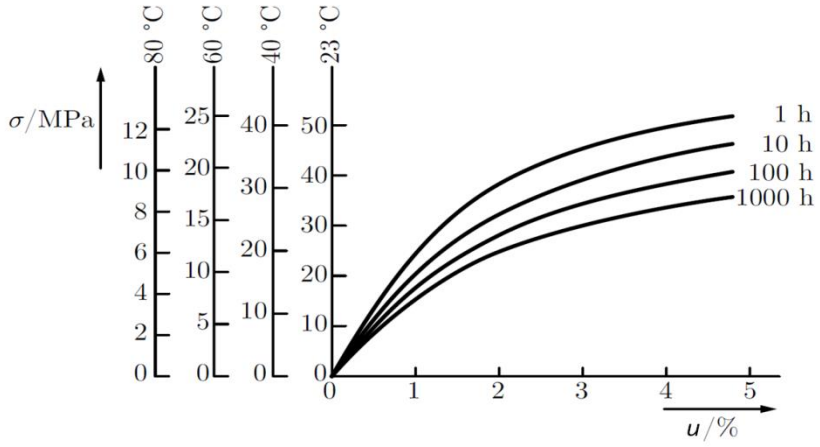

Fig. 15: Isochronous stress-strain curves of amorphous polymethylmethacrylate with a glass temperature of approximately 100 °C [Rösler 2007]

Water as a plasticizer acts as a mobility enhancer whereas the hydrothermal aging. Its low molecular weight causes a huge increase in molecular mobility of amorphous and partially crystalline polymers due to an increased free volume. The water uptake has influence on mechanical properties for example, an overall reduction in the tensile properties at break can be observed. Generally, the main degradation occurred in the earlier stages of diffusion. A possible saturation of the stronger hydrophilic groups with a reduction of the water–polymer interactions could take into account this

relative stabilization for higher water contents. Losses in the tensile, elastic modulus and in the indentation hardness are the results by the plasticizing effect of water [Nogueira 2001].

It is a function of the plasticizer to insert itself between the polymer chains. The main obstacle to this endeavor are the attractive forces between the polymer molecules, which are influenced by the chemical and physical structure of the polymer. This means a change of the chain molecules. It should be noticed that when a low molecular weight material like water compound penetrates the crystalline regions, certain properties which depend on crystallinity such as the mechanical properties will deteriorate [Immergut 1965].

Generally the purposes for using a plasticizer in the polymer are the following:

1) Increase the elasticity of the polymer.
2) Decrease the glass transition temperature.
3) Improve the properties such as non-flammability, thermal stability, shock resistance, antistatic properties, etc..

Besides, softening in mechanical properties during plasticization is unavoidable, such as reduction of elastic modulus and hardness correlating with molecular mobility. The lower the viscosity of the plasticizer is, the more the rigidity in the polymer drops. According to the structure of the polymer and plasticizer, the plasticizer can act as:

i. A lubricant, which reduces the intermolecular friction and by this increases the deformability of a polymer. This is a reversible phenomenon.

or as

ii. A substance, which breaks the intermolecular bonds in a polymer network. According to these inferences the role of the plasticizer is amounted to the screening of centers of intermolecular forces in the course of selective solvation of these points. This phenomenon is irreversible [Shtarkman 1983].

1.3.1 Formalisms for quantifying the viscoelastic properties

In general, the modulus of a viscoelastic material (or complex modulus E^*) has two components:

a) A real component E′ which is also often called the storage component and describes the linear elastic behavior of a material.
b) The second component is the imaginary part of modulus E″, which is often called loss component that describes the material's viscous behavior. In a polymer the loss modulus presents actually the energy loss during a test in heating, while the real part of the elastic modulus relates to the volume change of the material [Gottstein 2007].

In general, the complex modulus is described as follows [Gottstein 2007]:

$$E^* = E^{'} + jE^{"} \quad \text{Eq. 4}$$

and [Cohen 2013]:

$$|E^*| = \sqrt{E'^2 + E''^2} \quad \text{Eq. 5}$$

For formulating the time response or mechanical properties in terms of known mechanical elements, a spring (to present the in-phase deformation) is combined to a dashpot (for off-phase deformation) either in series (Maxwell model) or in parallel (Voigt model), shown in Fig. 16a, b. In general, the Maxwell model is more appropriate to a viscoelastic fluid [Rösler 2007]. The Voigt model is more suitable for a viscoelastic solid [Cohen 2013]. This model describes the behavior of a purely viscoelastic material i.e. the deformation just depends on time and not the applied stress. Based on Voigt configuration, the total strain (u) is equal to the elastic strain (u_e) and viscous strain (u_{in}):

$u = u_e = u_{in}$

Furthermore the applied total stress (σ) is equal to the stress applied to the spring (σ_e) in addition to the stress applied to the dashpot (σ_{in}):

$\sigma = \sigma_e + \sigma_{in}$ [Gottstein 2007].

For the spring we basically apply Hooke´s law:

$$u_e = {}^{\sigma_e}/_{E_V} \quad \text{Eq. 6}$$

where

E_V is the spring constant in the Voigt model [Pa].

For a dashpot a Newtonian flow rule can be applied, which relates the inelastic strain rate ($\dot{u_{in}}$) to the σ_{in} and viscoelasticity (η_V):

$\dot{u_{in}} = {}^{\sigma_{in}}/_{\eta_V}$ [Gottstein 2007].

The total applied stress can be written as follows:

$$\sigma = \sigma_e + \sigma_{in} = E_V u + \eta_V \dot{u_{in}} \quad \text{Eq. 7}$$

or alternatively one can write:

$$u = \frac{\sigma}{E_V}\left[1 - exp\left[-\frac{E_V}{\eta_V}t\right]\right] \quad \text{Eq. 8}$$

A constant load strains the spring, but the friction within the dashpot element provides a large initial resistance to the strain, causing the strain to increase with time. Both the E_V and the damping parameter η_V are temperature-dependent. If a constant stress (σ =constant) is applied in accordance to the Voigt-Kelvin model, the model predicts inelastic behavior of samples but in the case that $\frac{\delta u}{\delta t} = 0$, the model predicts a pure elastic behavior. In other words, for load control measurements, like creep tests performed via nanoindentation the model could be used successfully. However, if a constant strain is applied for a defined time and measures the reduction of the stress, like a standard creep test via an atomic force microscopy (AFM) test, the method could not be used for the evaluation of the results. The oversimplified mentioned models are important tools to qualitatively evaluate the physical

properties of a polymer. Therefore this simple model is only qualitatively, but not quantitatively, correct. More sophisticated evaluation of the results is possible with a combination of Voigt and Maxwell elements, for example using a generalized Voigt model as shown in Fig. 16c, which consists of two parallel Voigt components. This latter model is widely used for evaluation of the creep tests performed via the nanoindentation method. However, this model ignores the stress-dependence of the deformation. If the stress is sufficiently large, a polymer can deform plastically even below the glass transition temperature. In Fig. 16c parameters K_1, K_2 and C_1, C_2 refer to storage and loss stiffness.

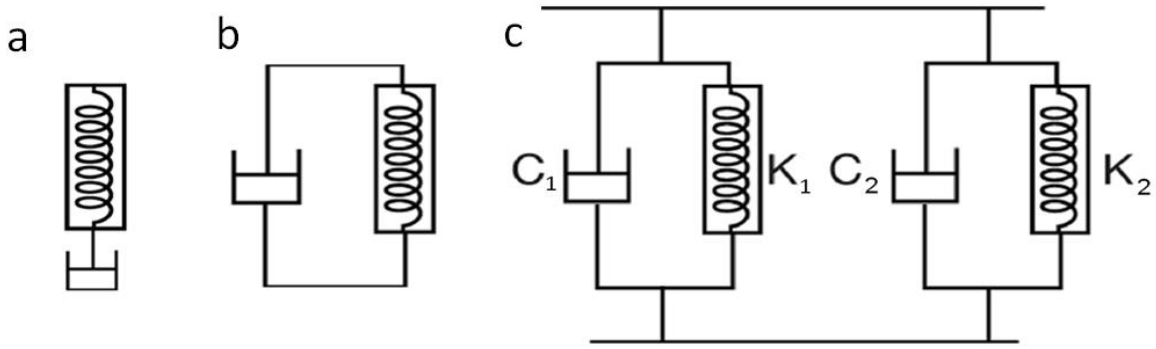

Fig. 16: A schematic representation of a) Maxwell, b) Voigt and c) generalized Voigt model

1.3.2 Experimental approaches for evaluation of the viscoelastic properties

As it was discussed, both elastic and plastic properties of polymers are time-dependent even at room temperature. Viscoelastic effects can be neglected only if strains and loading times both are small. Though, the way of performing the test (selected loading function) will have a strong impact on the measured properties. Hence, the quantitative comparison between the results of different working groups is very difficult. For more exact evaluation of the viscoelastic properties, dynamic mechanical analysis (DMA) is much more suitable to use. It gives the opportunity to quantify the storage and loss modulus of polymers.

DMA is designed for testing on the macroscopic scale, typically with specimens on centimeter size scales and has been successfully proven effective. Various dynamic techniques with the capability of applying cyclic stress and/or strain could be performed. The most typical methods are:

i) Using a parallel plate test fixture. In this setup, a specimen is placed between the parallel plates as shown in Fig. 17a. This technique measures a shear modulus as the plates are rotated at different angular frequencies and with different rotational amplitudes. The effects of the testing frequency can be observed by the amount of force that is necessary to accomplish the rotation desired [Hysitron 2014].

ii) A sample can be tested uni-axially through a tension test, as in a typical dog-bone tensile test (Fig. 17b).

DMA has the capability of testing frequencies over several orders of magnitude, beginning from the mHz range and going well into the hundreds of hertz. However, DMA is most successful at accurately characterizing macroscopic materials under 50 Hz [Hysitron 2014]. By the way, the macroscale DMA measurements are very time consuming to accurately quantify the complex modulus of polymeric materials using quasistatic techniques, requiring numerous tests and copious amounts of analysis. One other important drawback of the macroscopic testing methods is their inability to collect mechanistic information especially in the case of inhomogeneous materials. For example, a process like aging could cause debonding. It affects significantly the results of macro-mechanical testing methods. Hence precise interpretation of the macroscopic mechanical tests will be more complicated because the results are not influenced just by water absorption but also contribution of the debonding. To overcome the problems mentioned, it has been decided to locally characterize the mechanical properties via the nanoindentation technique. Detailed information about the technique is therefore provided in chapter 4.3.3, including its features and limitations.

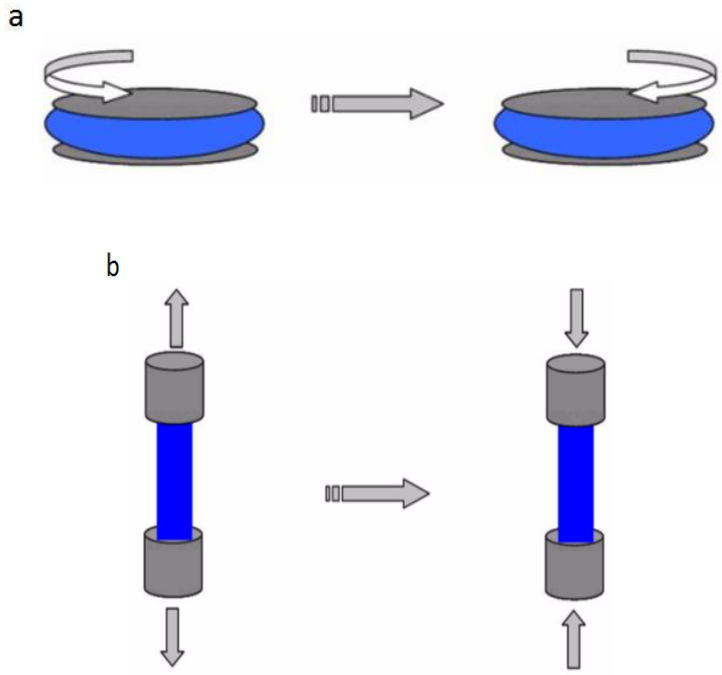

Fig. 17: Macroscopic testing methods for evaluation of the viscoelastic properties of materials, a) a parallel plate test fixture, b) uni-axial testing method [Hysitron 2014].

2 State of the art

Even after about 40 years of the life of the first CIPP, recognition and verification of cured in place pipes is still limited to destructive testing in the laboratory. The key aspect of this work is focusing on the application of the non-destructive testing methods on CIPP analysis. In order to have a better investigation of this term, the concentration should be on a certain material of CIPP and the methods of its recognition and verification.

Material of samples

The material studied in this thesis is UPR combined with unwoven polyethylene terephthalate (PET) fibers as carrier material.

UPRs are thermoset polymers with a relatively low molecular weight. There is a difference between UP and unsaturated UPR. Due to brittleness at room temperature and the difficulty to handle, UPs are rarely sold as such. Instead, they are mixed with a vinyl monomer in the molten state, whenever polyester is freshly synthesized in a plant. Therefore, materials that are viscous at room temperature, with a styrene content of ca. 60% are sold. This mixture of an UP with the vinyl polymer is referred to as an UPR [Ma 1993].

UPRs contain double bonds (ethylenic groups) along the polymer chain. Unsaturated polyester resins are cured by cross-linking the long linear chains by means of vinyl monomers such as styrene, diallyl phthalate, methyl methacrylate, vinyl toluene, divinylbenzene, or combinations of these. Coating formulations generally contain the polyester resin dissolved in the vinyl monomer, which is subsequently cross-linked and cured by stirring in a catalyst (here peroxide as initiator) just before use (see Fig. 18).

The polymerization mechanism involves free radical addition across the double bonds; hence, no volatile by-products are evolved. This is a distinct advantage over condensation polymerization, where water or other by-products that degrade electrical properties are produced during the cure. Free radicals may be initiated by thermal energy, ultraviolet light, or chemicals notably the organic peroxides [Kandelbauer 2014].

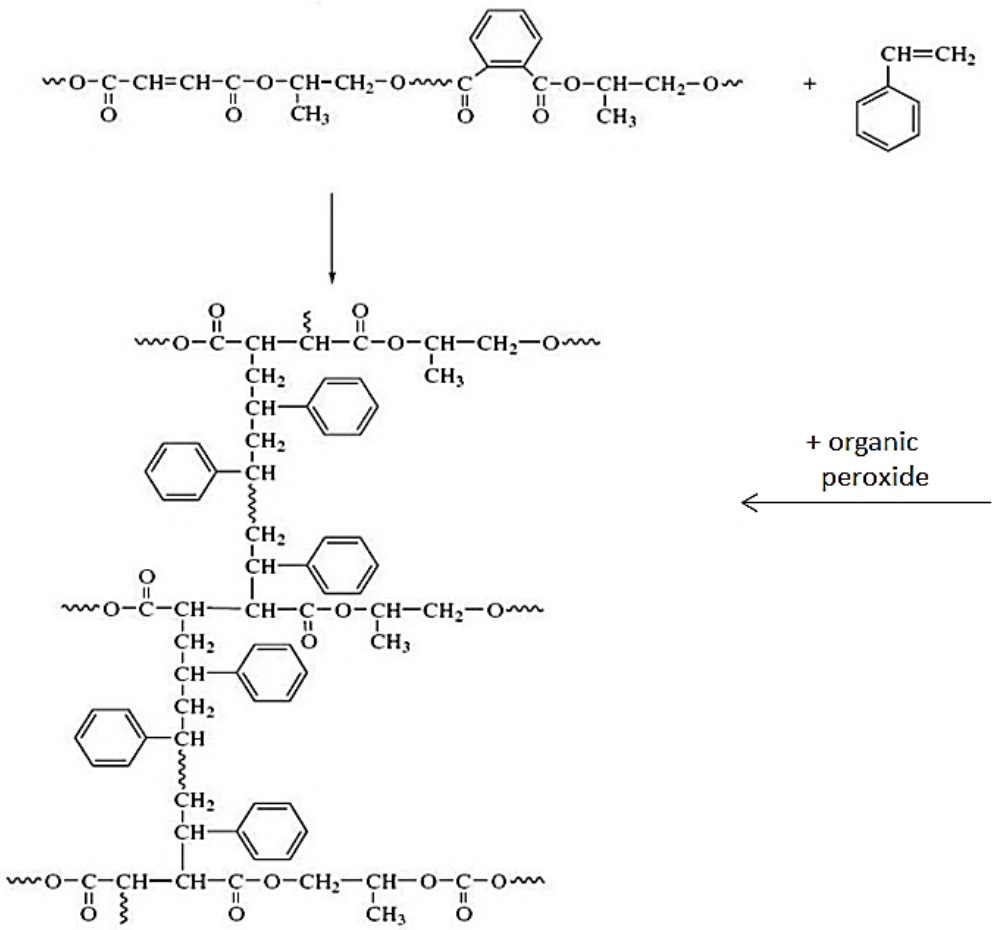

Fig. 18: Synthesis of the UP and subsequent crosslinking of UP chains with styrene as the co-monomer [Fink 2013].

According to this fact, UPR consists of two polymers: short chain polyester containing polymerizable double bonds and a vinyl monomer. The curing reaction defines as copolymerization of the vinyl monomer with the double bonds of the polyester [Fink 2013].

PET is a thermoplastic polyester, possessing excellent thermal and mechanical properties. PET has substantial fraction by volume in the waste stream and high resistance to the atmospheric and biological agents. It is formed by polycondensation reaction between terephthalic acid and ethylene glycol, which may exist as amorphous and semi-crystalline material [McKeen 2014]. Its structure is shown in Fig. 19.

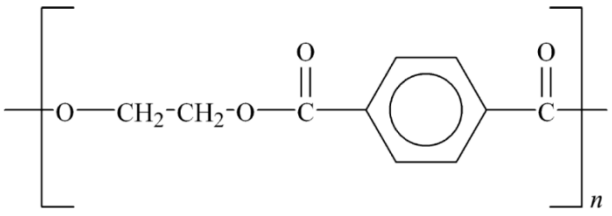

Fig. 19: Chemical structure of PET polyester [Potiyaraj 2007]

The most important properties of PET are:

- High mechanical properties,
- High thermal properties,
- Good electrical properties,
- Dimensional stability,
- Excellent chemical resistance, and
- Flame retardancy [McKeen 2014].

2.1 Curing of unsaturated polyester resins

Crosslinking agents for addition polymers are molecules that contain two or more double bonds per molecule, for example styrene. Crosslinking of linear chain polymers causes them to stiffen and retain their shape and makes them insoluble in solvents that dissolve the linear chain polymer.

In order to prepare the crosslinking units, unsaturated polyesters are dissolved in a polymerizable monomer such as styrene. The curing process of thermosets consists of two main phases: the heating period of the liquid resin (either pure or in the form of composites with fillers) and the cure reaction in the mould [Hanemann 2010; Yang 1991].

Styrenated unsaturated polyester resins can be cured by either room temperature or heat curing methods. Diallyl phthalate or isophthalate monomers do not respond well in room temperature cures and are generally only used in such heat curing applications as prepreg and molding compounds.

The crosslink density, residual unreacted styrene monomer content and unreacted ester C=C bond content can be determined by Fourier Transform Infrared Spectroscopy (FTIR) [Fink 2013] but in this thesis the electromagnetic waves are used to figure out if it is cured or not.

The unreacted ester C=C bond of UP and styrene bond C=C bond in comparison to reacted bond C-C can differ by electromagnetic waves microwaves and terahertz (THz). It shows that these bonds have different permittivity and therefore different absorption of waves [Kandelbauer 2014].

This difference can be also determined by FTIR. The absorption of ester C=C bond at the wave number λ^{-1} =982 cm^{-1} used to determine the unreacted ester C=C bond concentration and the absorbance of styrene C=C bond at λ^{-1}=912 cm^{-1} shows the residual styrene monomer concentration. The absorption of C=O bond at λ^{-1} =1731 cm^{-1} used as an internal standard the absorbance of styrene vinyl C=C decreases while the degree of curing increases [Ma 1993].

2.2 Characterization of aging effects in UPR and PET materials

PET fibers with unsaturated polyester resin in CIPP are used in order to carry the resin material. PET fibers do not reinforce the UP resin. They only help the resin to become more stable and to form easier into the CIPP. There is no reinforced polymer considered as UPR/PET. Consequently, the aging behavior of UPR and the related testing methods have been investigated where the approach and the results are described below.

2.2.1 Hydrothermal aging of unsaturated polyester resins

It is known that polyester resins are sensitive to moisture through water absorption leading to chain scission by ester hydrolysis and thus to embrittlement. The degradation of polyester resins in water at different temperatures contains water uptake, swelling, ester hydrolysis, osmotic cracking and leaching of small molecules. Nevertheless, in reality, the most important aging process is cracking, originally described for polyester matrix and composites exposed in hot water [Bélan 1997; Bellenger 1995]. The osmotic cracking nucleation is formed by a phase separation between the polymer and water-soluble organic molecules subsequent. Depending on the initial state of the polymer and water-soluble molecules system (heterogeneous or homogeneous), the osmotic cracking is sudden or crack induction time is observed depending on the water-soluble fraction and temperature. Major parameters promoting matrix cracking were identified including:

1. High fraction of monomeric and catalyst residues,

2. High fraction of ester functions in dangling chains, and

3. High reactivity of ester functions.

As any cracking phenomenon, this process can be described in terms of initiation (defect nucleation), propagation and arrest. The mechanism of propagation is relatively well understood: it results from osmosis linked to the difference in chemical potential of water in the cracks and in the bath. The polymer layer separating the crack from the bath behaves as a semipermeable membrane and one observes the build-up of an osmotic pressure in the cavity. Microscopic observations allow detecting the cracks [Gautier 2000].

The nucleation mechanism can be assumed as follows: Hydrolysis proceedings on dangling chains (initially present or created by hydrolysis on elastically active chains) produce tiny organic molecules such as monomeric glycols or acids [Mortaigne 1999]. Due to a very low diffusivity (compared to water diffusivity and to their build-up rate), the acid molecules accumulate in the network. Since they are significantly more polar than the polymer, their equilibrium concentration must be low. Therefore, after a definite time, depending on the hydrolysis rate, the system becomes oversaturated and undergoes a phase separation. The excess of organic molecules leads to the build-up of micro pockets. Corresponding to the water affinity for those hydrophilic solutes, the entrance of water flux due to

micro cavity up to a certain limit increases the osmotic pressure, and osmotic crack propagation occurs. This mechanism is based on two major assumptions, which should be experimentally checked:

- the generation from hydrolysis of sufficient quantities of organic monomeric species to induce demixing;
- the low diffusivity of these organic molecules into the polyester, which must act as a semi permeable membrane [Gautier 2000; Mortaigne 1999].

2.2.2 Hydrothermal aging of PET

PET is known as a thermoplastic polyester with relative high stiffness, temperature performance and dimensional stability. The inherent hydrothermal fragility of the ester link motivates the scientists in analysing PET aging in water or humid atmospheres [Launay 1999].

Hydrothermal aging dependence on the water temperature and time of immersion induces a rapid and drastic decrease of the mechanical strength of PET.

The absorbed water induces not only a slight plasticization but also causes hydrolysis of the polymer chains in the amorphous phase by a random scission mechanism. Hydrolysis produces oligomers that either diffuse slowly out of the material or crystallize in the inter spherulitic zone. Therefore, the existence of oligomers modifies not only the hydrophilicity of PET but also its crystalline morphology, both features being likely to interfere with the absorption process.

Hydrolysis may affect even the crystalline of PET in too long aging time. Besides, formation of cracks or voids that induces an additional uptake of water and osmotic cracking is responsible for the material fracture [Foulc 2005].

2.3 **Characterization of unsaturated polyester resin and PET**

Polyethylene terephthalate polyester, PET, is known as the most common thermoplastic polyester and is often called just “polyester”. PET is both available as an amorphous (transparent) and as a semi-crystalline (opaque and white) thermoplastic material. The properties of semi-crystalline PET can be characterized by strength, ductility, stiffness, and hardness in comparison. Amorphous PET has better ductility but less stiffness and hardness [McKeen 2014].

The main methods to characterize UPR and PET consist of: thermogravimetric analysis, dynamic mechanical analysis, Fourier transform infrared, mechanical tests, morphological analysis and differential scanning calorimetry.

2.3.1 Thermogravimetric analysis (TGA)

To understand the pyrolysis and study the thermal stability of the UP resin, a thermogravimetric analysis (TGA) in dynamic conditions can be carried out, which is executable at different heating rates for example 10 °C/min. The experiment runs at room temperature under an argon atmosphere. This analysis is used to describe the weight loss of the sample as it is heated to show the temperatures at which degradation takes place [Ridzuan 2016].

2.3.2 Dynamic mechanical analysis (DMA)

The DMA is a thermomechanical method to measure the viscoelastic properties of materials. It expresses the T_g of the material and allows to have an idea about the behavior of a material when it is subjected to mechanical and thermal stresses simultaneously.

This method can be also used to measure temperature-dependent properties, such as the storage modulus (E′), loss modulus (E″), and damping factor tan(δ) of polymers [Ridzuan 2016].

2.3.3 Fourier Transform Infrared (FTIR)

Fourier transform infrared (FTIR) spectroscopy is employed to investigate the degradation behavior and chemical structure of UPRs and PET, providing insight into the degradation mechanism like thermal degradation, moisture degradation, etc.. This method identifies the nature of chemical bonds and the crystalline phases that are formed in the material [Dai 2013].

FTIR is an instrumental technique, which measures the amount of infrared radiation reflected from or transmitted through a specimen. It is used mainly to solve the composition of organic compounds. Polymers degraded by different parameters through crosslinking, free radical formation, permanent bond cleavages, etc., subsequently experience breakup of molecules and formation of saturated and unsaturated groups. All these processes introduce so-called defects inside the material that are accountable for change in the optical, electrical, mechanical and chemical properties of the material [Al-Kadhemy 2016].

Basis of the FTIR analysis is, how well a sample absorbs light at each wavelength. When a beam of infrared energy with at spectrum 750 nm to 1 mm passes through a sample, the energy at certain frequencies is absorbed by the sample. The optical absorption spectrum is the property of the certain molecule and its molecular motions and can be used for quantitative investigation of molecular systems.

2.3.4 Mechanical tests

In order to characterize the mechanical properties Izod impact strength, three point bending and tensile tests are applied [Bergeret 2009; Foulc 2005; Laoubi 2014; McKeen 2014].

Through tensile testing directly and indirectly these properties can be measured:

- tensile stresses,
- ultimate tensile stresses,
- elongation, and
- modulus properties [Bergeret 2009]

2.3.5 Morphological analysis

The morphology of UPR and PET with regard to cracks, debonding, fiber distribution is analyzed through an optical microscope [Sawpan, Holdsworth 2012; Sawpan, Pickering 2012].

In order to investigate the morphology with higher magnification in the nanoscale, a scanning electronic microscope (SEM) can be used. To do that the UPR and PET specimens need to be coated by evaporation of gold in vacuum in order to make them conductive [Chieruzzi 2013].

2.3.6 Differential scanning calorimetry (DSC)

DSC is a technique to perform thermal characterization investigation on thermosetting resins. Since the components in a resin system cure, the evolving heat is measured by the DSC. If no significant heat of cure is observed, it is assumed that the resin sample is completely or 100% cured. The T_g or softening temperature of a thermoset resin can be measured also by DSC. When a thermosetting resin cures, the T_g increases and the heat of cure decreases. These changes are used to characterize and quantify the degree of cure of the resin system [Kattan 2002; Mafi 2005; Nava 2003; Romanzini 2015].

3 Challenge and motivation

The main problem of using CIPP in wastewater pipes consists in the possible occurrence of abnormalities and damage during manufacturing, installation and operation. These flaws include visible damage on the surface, physical defects in the material, thickness variation, annular gap between CIPP and pipe and deterioration of mechanical properties. Therefore, the CIPP should be inspected at manufacturing, installation and regularly during operation in order to distinguish if they are applicable or not. To do that, a sample of CIPP material has to be taken from a location in the pipe to be tested through destructive methods in a laboratory, such as bending tests and tightness experiments (see 1.1.5). The vacancy of CIPP resulting after sample removal, should be filled in again with liner material. This process is expensive, and the results of only few removed samples are not representative for the overall CIPP liner.

Even 40 years after the production of the first CIPP, the inspection of CIPP through non-destructive testing is still a challenging issue. The only applicable non-destructive testing up to now is CCTV inspection of the liner to detect the defects, discolorations, etc.. However many abnormalities of CIPP are not visible with this technique.

So far few preliminary tests have been made with regard to NDT tests. According to a report from the IKT [Sokoll 2009], the following NDT techniques have been tested in the context of CIPP:

- 3D laser scanning,
- Temperature measurement through glass fiber cables,
- Heat flow thermography,
- Impact echo measurement,
- Local resonance spectroscopy, and
- Ultrasound echo measurement.

Nevertheless, the problem is, for all measurements with these techniques the validation of the test results are still pending. The tests have been applied in situ, but they have not been validated through testing in a laboratory on CIPP samples and compared with conventional experimental results. For example in the results of heat flow thermography, some irregularities have been seen, which are supposed to be delamination or pores [Sokoll 2009]. Since this part of the CIPP was not ever taken from the pipe to be tested in the laboratory, a proof of detecting delamination or pores is still pending. Therefore, these measurements should be completed and respective conclusions should be drawn as to how NDT could obtain a valuable role for quality control of CIPP after manufacturing, installation and during operation.

In this thesis for the first time the use of other NDT techniques based on microwaves, terahertz waves and also water immersion ultrasound is explored to figure out if these techniques are able to measure the properties, which are until now only measured through destructive testing. The advantage of microwaves and terahertz techniques are their contactless application. Therefore, no couplant is needed and it makes the inspection easier and faster. These methods are sensitive to moisture and allowing detecting even a small amount of water. Their penetration depth is much larger than infrared radiation and permits the probing of a significant volume of material in a pipe. Microwaves and terahertz methods are relatively insensitive to environmental conditions and in contrast to ionizing radiation, these methods are much safer and faster.

The samples of CIPP are tested through the NDT methods before and after hydrothermal aging, which correspond to test the CIPP after installation and in operation. In contrast to IKT [Sokoll 2009] and Allouche [Allouche 2012; Allouche 2014], which used the ultrasound technique only on dry samples, here the ultrasound technique does not only apply on dry but also on wet samples being saturated with water, because in reality the CIPP is exposed to water. It is seen that the existence of water in samples plays an important role in measurements, which has been ignored before.

The results obtained with different techniques have to be validated not only among themselves but also compared to results obtained with other characterization methods such as nanoindentation and optical microscopy.

4 Experiments

4.1 Required equipment and theoretical background

4.1.1 Furnace

In order to reach the desired temperature during the hydrothermal aging, a furnace is required. The furnace controller B150 shown in Fig. 20 is an electronic programmable controller which enables the precise control of heat treatment processes with the verification value of 1 °C . This controller has:

- 9 programs, each with 18 segments, which can be individually programmed and saved,
- Two extra functions which can be switched on during a process,
- Automatic timer for a programmable start time,
- LCD display with 4 lines of text,
- Programming of date and time, and
- Highest temperature up to 650 °C.

Fig. 20: Nabertherm furnace with controller B150

4.1.2 Electrical balance

For a precise weight measurement of CIPP samples during hydrothermal aging a balance model PCE-AB 200C has been used in this thesis.

Analytical balances of PCE-AB xxxC series are designed for laboratories and applications that require a high accuracy in the range of 0.1 mg. It includes an internal calibration feature that ensures the user of this analytical balance to be at a very high accuracy as well as the control of weighing. Fig. 21 shows the balance PCE-AB 200C.

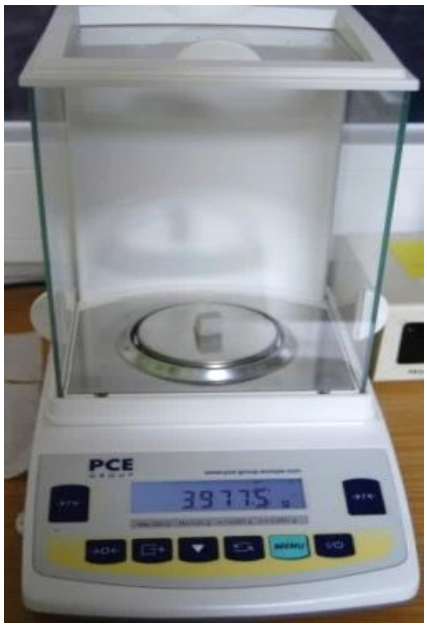

Fig. 21: Balance PCE-AB 200C

The technical properties of the balance PCE-AB 200C are shown in Table 1.

Table 1: Technical specifications of balance

Balance type	PCE-AB 200C
Weighing range (max)	200 g
Minimum load	10 mg
Readability	0.1 mg
Verification value	1 mg
Calibration class	I
Permissible ambient temperature	+18 to +30 °C
Transit time	<5 s
Overall balance (with feet)	215(235)×345×350 mm
Weighing space	175×140×230 mm
Connection	~230 V 50 Hz 9 VA / =12 V 300 mA
Total weight	6.5 kg

Water uptake was first measured by weighing the samples periodically at ambient temperature. The relative weight gain of the matrix was plotted versus the square root of time (Fig. 83).

4.1.3 Optical microscope

The Leica DM6000 (Fig. 22) is a research system microscope with motorized and automated functions for electrophysiological applications. The following contrast methods come into use:

- Bright field,
- Phase contrast,
- Simple polarization contrast,
- Differential interference contrast (DIC), and
- Fluorescence.

The features, adjustments of diaphragms and filters as well as adjustments of luminous intensity to the magnification and contrast methods can be carried out and reproduced automatically. The fluorescence illuminator, including filters, diaphragms and shutters, is completely automated. All motorized functions are controlled and displayed using the Leica STP6000 touch panel.

The optical microscope Leica DM 6000 consists of:

1) Stand base,
2) Rear side,
3) Focus,
4) Guide plate,
5) Upper part of stand,
6) 1" motorized fluorescence axis,
7) Tube change interface, and
8) Two slide holders for filters or boosters.

Fig. 22: Optical microscope Leica DM 6000

4.1.4 Nanoindenter

Nanoindentation tests were performed with a Hysitron TI 900 TriboIndenter (shown in Fig. 23) equipped with a Performech controller, Stanford Research Systems (SRS) 830 DSP lock-in amplifier and National Instruments USB-GPIB adaptor. The internal digital feedback loop rate and data acquisition rates were 78 kHz and 38 kHz, respectively. In this thesis a one-dimensional, nanoDMA III compatible transducer was used. With this transducer, performance of the dynamic measurements was possible. Load and displacement resolution of the transducer was 1 nN and 0.04 nm respectively and the thermal drift was less than 0.05 nm/s. Additionally, the TriboIndenter utilizes an active anti-vibration system, an acoustic enclosure, a stage controller, optic and optic electronics.

Fig. 23: Hysitron TI 900 triboIndenter nanoindentor

Theory:

Nanoindentation, a mechanical testing technique, which is often considered to be non-destructive in the sense that the indentations are in general, too small to be observable by the naked eye and the test does not impair the structural integrity of the specimen. Different types of tests can be performed with the nanoindenter including quasistatic nanoindentation and nanoDMA indents. Quasistatic nanoindentation was traditionally used to quantitatively measure the mechanical properties, like hardness and elastic modulus of materials with linear elasticity like metals or ceramics. With the quasistatic nanoindentation method one can collect the applied load vs. displacement data and measure the hardness and elastic modulus at one single depth of indentation, with the presumption that the material deformation is purely linear elastic/plastic.

As it was discussed earlier, the magnitude of the real part of the elastic modulus depends heavily on temperature, while the magnitude of the imaginary part depends on both temperature and time. Therefore, the quasistatic measurements are not suitable and hence the nanoDMA method was used for studying systematically the time-dependent mechanical properties. With the aid of dynamic measurement, a sinusoidal loading could be applied in addition to the quasistatic loading. With this technique one can define the load amplitude and frequency (10 Hz - 200 Hz) in addition to the routine controllable parameters for the quasistatic condition, such as the maximum load, load rate, number of segments, data acquisition rate etc. The nanoDMA technique offers the advantage of significantly decreased testing time by examining mechanical properties over a range of frequencies. Additionally the required materials for the samples comparing to the macroscopic DMA measurements is less. The viscoelastic characterization of polymers can be experimentally studied by several means, the most common methods are:

a) Creep, in which the indenter is rapidly brought to a given force/stress and the change in displacement required to maintain the defined force is monitored. A conventional quasistatic creep test is the application of a constant stress (or force) for a defined time period and measurement of the strain (or displacement). During the long time of test, and for keeping the force constant, a constant voltage will be applied to the transducer and hence it may warm up with time. Increase of the temperature may influence the validity of the measured displacements. One important shortcoming of this technique is the inability of separating the creep behavior of the material and the thermal drift of the device. A dynamic reference creep test is similar to a creep test performed with standard indentation, however, with the use of reference frequencies the test time can be much longer and because of the dynamic components, the test will continuously measure hardness, stiffness, modulus, etc. (see Fig. 24). A reference creep test is a test with an initial reference frequency segment followed by a long constant force dynamic segment. The first reference frequency segment will be used to calculate the contact area and the second (longer) reference frequency segment will be analyzed as the creep segment [Herbert 2008].

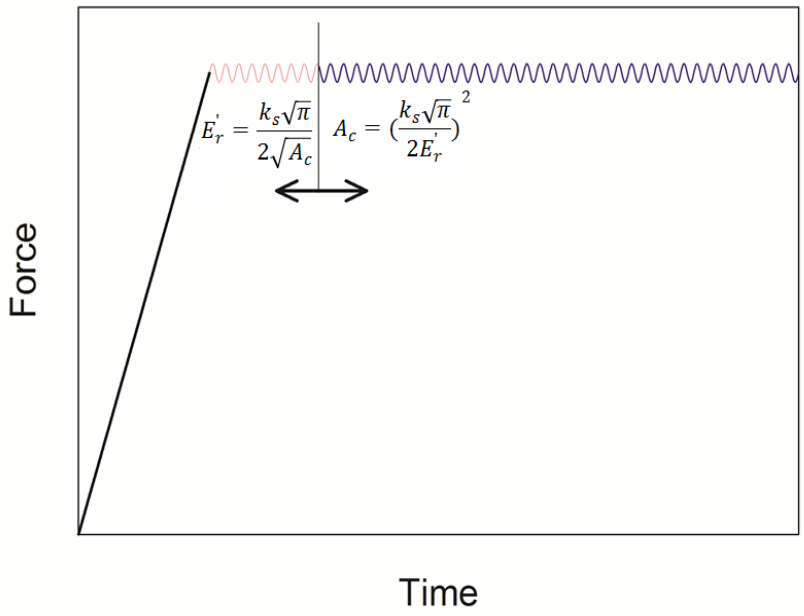

Fig. 24: Typical load function used for a creep test in addition to the method used for drift compensation during the test

b) Frequency sweep test, which is applying a sinusoidal force with a defined amplitude at various frequencies (f), while $t = 1/(2\pi f) = 1/\omega$ (ω is the angular frequency). For a sweep test the frequency is varied in each progressive step. During this type of test, a fixed quasistatic load is chosen as well as a fixed dynamic load amplitude. Mechanical properties of viscoelastic materials often vary when tested at different frequencies. A ramping frequency test is used to determine mechanical properties as a function of frequency. This is the typical form of test performed by a DMA instrument at macroscale. The frequencies may be ramped from 10 Hz up to 200 Hz. When testing at lower frequencies (below 10 Hz), the test can take a very long time, so it is recommended that lower frequency tests utilize the reference frequency functions to minimize drift effects. When testing is performed over 200 Hz, the amplitude can become quite small and it may be difficult for the lock-in amplifier to measure the phase and amplitude of the displacement signal. The user must be sure that the amplitude is large enough at higher frequencies to ensure quality data. Fig. 25 shows the load function test [Oliver 2004].

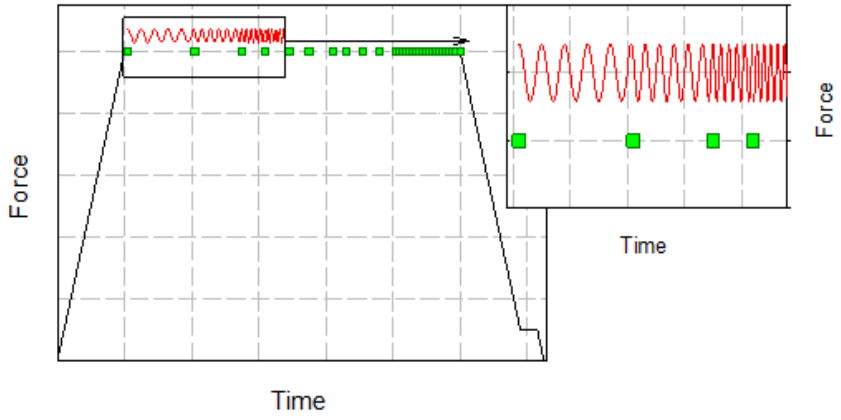

Fig. 25: A typical load function used for a frequency sweep test

For detailed evaluation of the mechanical properties it has been decided to use local techniques because the required materials and time for performing experiments will be reduced. More importantly, the macroscopic scale of tests is sometimes not very successful in obtaining mechanistic information especially in the case of inhomogeneous materials. For example, a process like aging could cause debonding, which influences significantly the results of macro-mechanical testing methods. Hence precise interpretation of the macroscopic mechanical tests will be more complicated because the results are not influenced just by water absorption but also contribution of the debonding in interface and cracks in the matrix.

The attractive feature of local tests is the ability to characterize the mechanical behavior of small volumes of matrix and fibers with spatial resolutions in the nano to micrometer range. The mechanical properties determined through local tests (including AFM or nanoindentation) are therefore not affected by osmotic cracks and debonding. What can change the mechanical properties such as hardness and elastic modulus is the material structure of the matrix and fibers. However, there are some challenges for local measurements, which are descried below:

i) A proper location on the surface requires great precision [Deuschle 2007]. It is due to the fact that the force resolution of the device is in the range of micro Newton. In the case of soft polymers with an elastic modulus of some few MPa this force may cause deformation.

ii) Some polymers are coated and hence surface properties may be different from the bulk properties. More importantly, polymer surfaces may exhibit markedly different viscoelastic behavior than their bulks due to differences in the microstructure and molecular chain mobility [Chakravartula 2006].

iii) Getting knowledge of the exact contact geometry is critical at nanoscale even after precise sample preparation and device calibration, while the presumptions of a smooth surface

may not hold. To get rid of the influence of sample roughness, it is very common to enhance the depth of indentation and it reduces the lateral resolution of the measurements and also increases the contribution of adhesion on the results while the contact surface will increase [Cohen 2013].

Local techniques

It is difficult to obtain meaningful and accurate data using quasistatic testing. It is due to the large impact of the loading function on the measured properties of polymers. Therefore performing dynamic local measurements is necessary in order to gain systematic information about their viscous behavior. AFM was used intensively for studying the mechanical properties of polymers mainly due to the low thermal drift of the system and hence its stability over time and thus accurate measurements especially at low frequencies (between 0.1 and 1000 Hz). However, the main drawbacks of AFM could be listed as below:

i) The AFM tips are normally installed tilted with an angle of about 15°. Hence the applied forces are not restricted to the surface normal.

ii) In polymers, it is more convenient to use tips with low stiffness (less than 5 Nm) and hence the cantilever may twist during the indentation, especially at the start of the indentation, because of a torque arising from the imperfect vertical loading of the tip owing to the sample roughness, and the alignment of the sample or the tip. This can lead to either a flexural or a torsional force.

iii) The maximum applied force and depth of indentation is mostly limited. Although more recent progress has been achieved with modern AFM devices (e.g. PeakForce measurements with the aid of Bruker devices), which overcomes this shortcoming.

The nanoindentation technique could solve all these problems mentioned. However, the stiff diamond tip in addition to the lower force resolution when compared to the AFM technique could destroy the surface during scanning or alternatively during the tip approach. Therefore, it is more convenient to use a blunt tip (with a radius of some hundreds of nanometers) instead of a sharp tip for polymers.

The nanoDMA technique (which performs DMA measurements at nanoscale) was used recently to study locally the mechanical properties of materials with time-dependent deformation and recovery behavior. In the classical dynamic test at the macroscale the phase lag is measured from the strain response to a sinusoidal tensile or flexural stress, while the phase lag in nanoindentation is controlled by the displacement response of the indenter to sinusoidal loading. In this thesis, the discussion is limited to linear viscoelastic behavior, which means that the strain depends only on time and not on the magnitude of stress. This holds when the stress is kept small.

4.1.5 Vector network analyzer

A vector network analyzer (VNA) is an instrument used to measure impedance. It is possible to measure impedance at lower frequencies with relatively simple tools, including a sine wave generator, a volt meter, a current meter, and a calculator [HP8510 2001].

At radio frequency (RF) and microwave frequencies, measurements of voltage and current become more complex. As a result, a VNA uses a more complex design to measure incident and reflected waves. In many ways, the VNA combines the principles of the basic impedance measurement with hardware appropriate for microwave frequencies. When using a VNA to measure the impedance or the reflection factor, a sine generator stimulates the device under test (DUT). In addition, two receivers take the place of the combination of a volt meter and current meter. These receivers, with the help of signal separation hardware, characterize the response of the device by measuring the phase and amplitude of signals that are both incident to and reflected from the DUT. Finally, calibration capabilities are required to eliminate systematic errors and compute the appropriate ratios (similar to the impedance) necessary to produce S_{11}, which is one part of the S parameters (see 4.3.4.2) [HP8510 2001].

Vector network analyzer systems, such as the HP 8510, measure the magnitude and phase characteristics of networks and of components such as filters, amplifiers, attenuators, and antennas.

The HP 8510 Network Analyzer is a fully integrated vector network analyzer system. The minimum configuration consists of a source, a test set, and the network analyzer [HP8510 2001].

Source: The source provides the RF signal. An HP 8360 Series synthesized sweeper, or an HP 834x Series synthesized sweeper, or an HP 835x-Series sweep oscillator with an appropriate HP 835xx Series plug-in, may be used.

Test set: The test set separates the signal produced by the source into an incident signal, sent to the device under test and a reference signal against which the transmitted and reflected signals are later compared. The test set also routes the transmitted and reflected signals from DUT to the receiver (IF/detector). Any HP 851x Series test set may be used.

Network analyzer: An HP 8510C network analyzer, which includes the HP 8510 Display/Processor and the 85102 IF/Detector (Receiver). The receiver together with the display/processor processes the signals. Using its integral microprocessor, it performs accuracy enhancement and displays the results in a variety of formats.

Peripherals: Additional system components can include HP-IB peripheral devices such as a printer, a plotter, and a disc drive. Measurement results and other kinds of information can be sent to a printer or plotter, or to a disc driver. These system instruments are controlled with the network analyzer front panel keys [HP8510 2001].

To obtain a high spatial resolution image of the liner samples microwaves in the frequency range of 75 to 100 GHz corresponding to the wavelengths of 4 to 3 mm were used in a contactless manner (free-space) in the reflective mode. Fig. 26 shows the VNA HP 8510 used in this thesis**.**

Fig. 26: Vector network analyzer HP 8510 (75-100 GHz)

Theory:

Like with all electromagnetic radiation, microwave propagation depends on the interaction between time-varying electric and magnetic fields. These fields oscillate in waves that are called travelling waves because energy is transported from one position to another. According to the medium through which the electromagnetic waves propagate, the velocity of propagation changes. Microwaves lie within a broad frequency range from 300 MHz up to 300 GHz, corresponding to wavelengths of 100 – 0.1 cm. Electromagnetic microwave radiation has been used in the determination of water content in various materials for at least four decades. One of the most important applications of microwave sensors is measurement of moisture [Zoughi 2000].

The propagation of a plane electromagnetic wave along the x-axis in a lossy medium can be described by:

$$\bar{E} = \bar{E}_0 exp(-jkx) \qquad \text{Eq. 9}$$

where

$\bar{E}$ is the electric field strength [V/m].

$\bar{E}_0$ is the peak value (vector) of $\bar{E}$ [V/m],

while

$$k = k' - jk''$$ Eq. 10

where

k is the complex propagation factor,

k′ is the real part, and

k″ is the loss factor by which the propagation losses in the medium are taken into account.

Dielectric spectroscopy determines the dielectric properties of the sample as a function of frequency. The complex permittivity ε is the dielectric property that describes how the material under an electromagnetic field influences the electric field.

$$\varepsilon = \varepsilon' - j\varepsilon''$$ Eq. 11

where

ε′ is the absolute permittivity or real part of permittivity [F/m], and

ε″ is the absolute loss factor or imaginary part of permittivity [F/m] [Zoughi 2000].

Absolute permittivity reflects a material's ability to store energy of the external electrical field during the polarization in the material, and the loss factor is related to the absorption and dissipation of the electromagnetic energy and the resistance of the material to the polarization by conversion into other kinds of energy (such as the thermal kind). Polarization is an ordering in space of an electrically charged unit under the presence of an external electric field. The charges become polarized to compensate for the electric field such that the opposite charges move in opposite directions. The external field causes the formation of an electric moment in the entire volume of the dielectric material in each polarizing units namely an atom, an ion or a molecule. There are three basic mechanisms of polarization in dielectric materials [Zoughi 2000; Zoughi 1995]:

- Electronic polarization: it is observed in most dielectrics, in which the centroid of the negative charges (electrons) and the nucleus (positive charges) in an atom experience a slight displacement in the influence of an electric field.
- Orientational (dipole) polarization: materials such as water or some polymers are composed of molecules that naturally possess a non-zero electric dipole moment. These materials are known as polar materials. These dipole moments are randomly oriented until an electric field becomes present, where they align and give rise to a net polarization vector.
- Ionic (molecular) polarization: some materials consist of negative and positive ions. In the presence of an external electric field, similar to the electronic polarization, a displacement occurs and the material polarizes [Zoughi 2000; Zoughi 1995].

The propagation factor is related to the permittivity by

$$k = 2\pi f\sqrt{\mu\varepsilon}$$ Eq. 12

also

$$c = \frac{1}{\sqrt{\mu\varepsilon}}$$ Eq. 13

where

μ is the magnetic permeability [H/m] and

c is speed of light [m/s].

The values for permittivity, permeability and speed of propagation in vacuum are:

$\varepsilon_0 = 8.854 \times 10^{-12}$ [F/m]

$\mu_0 = 4\pi \times 10^{-7}$ [H/m]

$c_0 = 2.998 \times 10^{8}$ [m/s]

In any medium other than vacuum, the constants obtain higher values and are usually expressed relative to the values in vacuum:

$$\varepsilon = \varepsilon_r \varepsilon_0$$ Eq. 14

$$\mu = \mu_r \mu_0$$ Eq. 15

where

r stands for relative.

For para-/diamagnetic materials $\mu_r \approx 1$. Therefore [Nyfors 1989]:

$$c = \frac{1}{\sqrt{\mu\varepsilon}} \cong \frac{c_0}{\sqrt{\varepsilon_r'}}$$ Eq. 16

The reflection coefficient (Γ) of electromagnetic waves at an interface is given by:

$$\Gamma = \frac{\sqrt{\varepsilon_1} - \sqrt{\varepsilon_2}}{\sqrt{\varepsilon_1} + \sqrt{\varepsilon_2}}$$ Eq. 17

where

ε_1: Permittivity of the first medium, e.g. air, and

ε_2: Permittivity of the second medium, e.g. specimen [Born 1980].

In the microwave range, free water (i.e. chemically non-bonded) exhibits a much higher permittivity (both real and imaginary part) than most solid materials [Nyfors 1989]. Therefore, by adding water to the solid, its moisture is increased, resulting in a substantial effect on permittivity. This difference in permittivity can be detected by microwave sensors. Therefore a change in permittivity will affect the velocity and attenuation of microwaves in a material.

Signal processing:

Signal processing is concerned with the representation of the signals by sequences of numbers or symbols and the processing of these sequences. The aim of this processing is to estimate characteristic parameters of a signal or to transform a signal into a form which is in some sense more desirable. A complex analog signal is a function of time, x(t), and it is formed by the real and imaginary parts (Fig. 27):

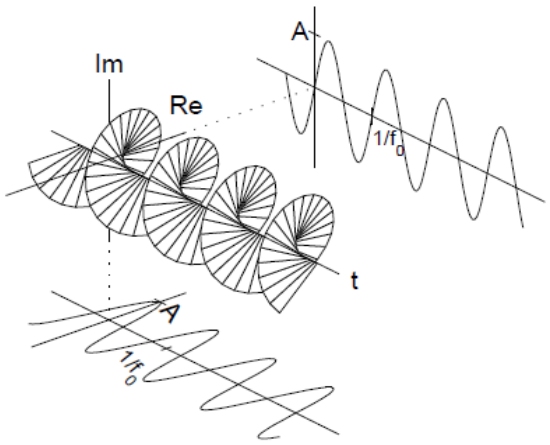

Fig. 27: Three-dimensional view of real and imaginary parts

The relationship between these two parts is given by:

$x(t) = x_R(t) + jx_I(t)$ Eq. 18

where

$j = \sqrt{-1}$

the signal can be also represented by magnitude and phase (Fig. 28):

$x(t) = a(t)exp(j\theta_a(t))$ Eq. 19

where

a is the magnitude [V],

θ is the phase [deg.], and

“a” can be calculated from:

$$a(t) = \sqrt{x_R^2(t) + x_I^2(t)}$$ Eq. 20

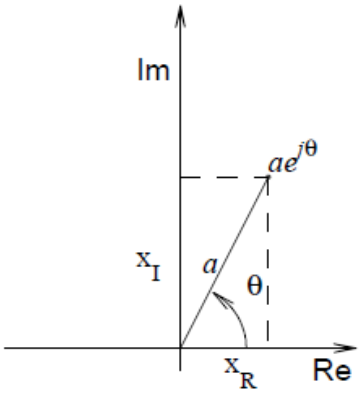

Fig. 28: Diagram of the relationship between the real and imaginary parts of the complex number x and its magnitude and phase.

4.1.6 Terahertz system

The measurements presented here were performed with a compact terahertz system made by Fraunhofer ITWM. The system is shown in Fig. 29. The system is operating in transmission mode with two antennas being the emitter and the detector. The samples to be inspected are placed on the x-y scanner axis carriage and are measured non-destructively in transmission mode.

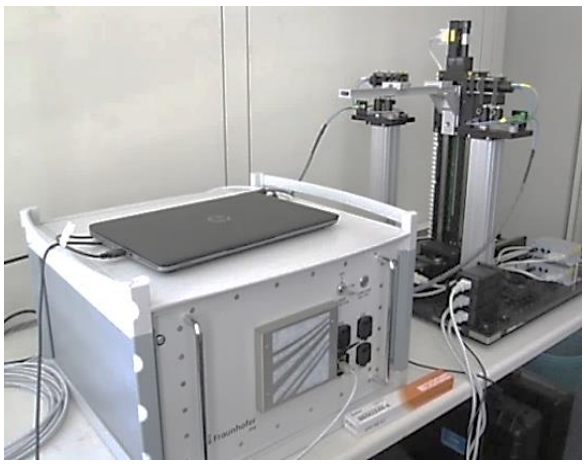

Fig. 29: THz system set up, transmission mode

The terahertz pulse transmitted through the sample experiences attenuation in amplitude, time delays to the reference pulse, scattering with comparing the width of the pulse in relation to the reference pulse and providing information about the spectral characteristics of the sample.

Theory:

The gap in electromagnetic waves between microwaves and infrared is the THz region of the electromagnetic spectrum frequency from 0.1 THz to 10 THz corresponding to the wavelengths from 3 mm to 30 µm respectively. This "terahertz gap" has historically been defined by the relative lack of suitable and inexpensive sources, detectors and systems for THz waves. Within the last 15 years, many new THz techniques have been pioneered, motivated in part by the vast range of possible applications for THz imaging, sensing, and spectroscopy [Carey 2002; Fitzgerald 2005].

THz today are with continuous wave (CW) and pulsed sources readily available. There is a difference between the CW THz radiation and pulsed form of THz radiation. In this thesis, the pulsed type of terahertz is used to characterize the materials [Liu 2013; Tredicucci 2004]. The terahertz sources can be categorized into thermal, electrical and optical/laser based. The THz system used in this thesis was laser based [Brückner 2010]. Fig. 30 [Kolano 2010] shows the schematic of the generation of a THz pulse through a photoconductive switch.

A split antenna structure is applied on a III-V group semiconductor of gallium (Ga) arsenide (As) substrate. A DC bias is placed across the antenna and an ultrashort pump-laser pulse (< 100 fs) is focused in the gap in the antenna. Irradiation of the gas with an optical pulse, whose energy is greater than the band-edge distance between the valence band and conduction band of the semiconductor, causes that the electrons and holes are generated. The result is a conductive channel. The externally applied field causes the separation of the electron-hole pairs, representing themselves, each a dipole moment. The integral over all dipole moments results in the source of the electric field. The strength of the electric field of the THz pulse depends on both the number of charge carriers and the electrical voltage [Chan 2007].

Fig. 31 shows the principle of a time domain spectroscopy in transmitted mode [Brückner 2010]. In this figure TDS refers ro time domain spectroscopy.

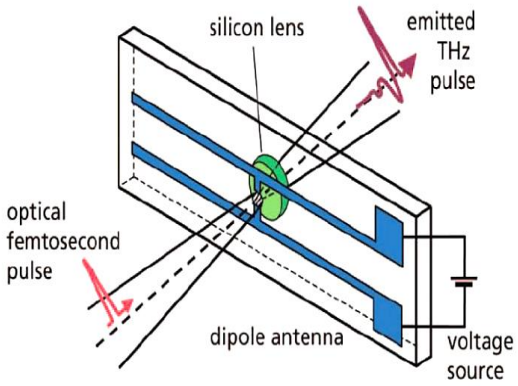

Fig. 30: Generation of a THz pulse through the photoconductive switch

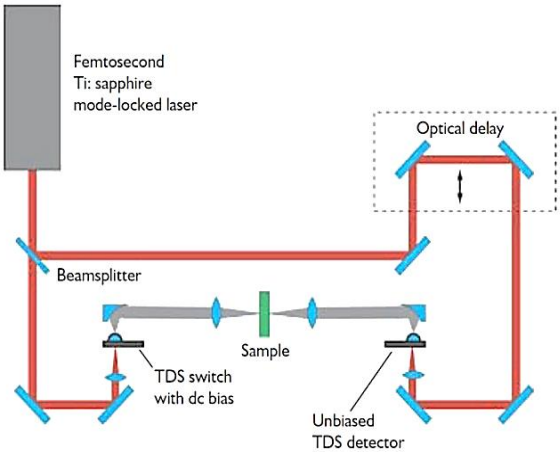

Fig. 31: Time domain spectroscopy, an image of the sample is built up based on selective absorption, which causes delays in arrival time at the detector

4.1.7 Ultrasound system with water immersion technique

In ultrasound testing a couplant is needed to transfer the acoustic energy between the transducer and the sample. Immersion in water is a suitable way of maintaining transducer coupling to the specimen surface. This method offers the advantages of:

- Uniform sensitivity from uniform coupling, and
- Suitable for automated scanning.

The reflection technique in pulse-echo mode is the most commonly used method in ultrasound immersion inspection. A single ultrasound transducer transmits and receives signals so that only single-sided access is needed. A pulse generator creates a signal to the transmitter that provides an acoustic wave. The wave spreads from the transducer face into the sample and back using water as an impedance transition medium. Through this round trip travel, the wave may cross several boundaries with different acoustic impedances that reflect the wave. The first reflection is at the front surface of the sample (front-wall echo). If there is any inclusions within the sample, the wave reflects again, when it interacts with internal surfaces of defects (defect echo). The last reflection occurs at the boundary of the test object and surrounding medium (water in this case). The reflected signal can be represented in several ways, namely as an A-scan, B-scan and C-scan [Cartz 1995].

The A-scan represents a time signal, which is the Hilbert transformation of the raw signal and shows the variations in amplitude of the ultrasound signal as it crosses a path from the transducer face to the sample back-wall and back. It means, A-scan signals give us the information of the thickness of the

material at a single point (x_0,y_0) at time t. A B-scan displays a scanning across the sample and mapping several A-scans parallel to the wave propagation. On a typical B-scan, the abscissa represents the position along the scanning direction and the values of time of flight (TOF) or distance are shown on the ordinate axis. The signal amplitude can be mapped to a color map scheme to display changes in amplitude owing to defects in a visual context. Usually the front and back-wall echo will have higher signal amplitude than the defect echo. This is visually represented by different colors mapped to the highest signal amplitude. If there is any defect in the path of the ultrasound wave, the back-wall echo amplitude at the x-position of the potential defect is weaker. The C-scan image represents a view of the sample as seen from above and therefore shows a cross section of the sample and defect parallel to the scanning surface. The C-scan image includes a series of parallel A-scans, which are operated over a surface, and the pulse echoes are limited to those returning during a fixed time interval. The reflected signals from the back-wall are "gated", and its peak value provides data for the C-scan image. To obtain a C-scan image, the sample is scanned in a raster pattern and the transmitted wave amplitudes are gated and mapped over the x–y plane within a certain time range. This type of data analysis helps us to track a defect through the thickness of the sample due to changes in amplitude [Cartz 1995].

In this thesis, a high frequency ultrasonic imaging system of the Hillger Company had been used for carrying out the tests, including probes, pan and a manipulator from the I-Deal company (see Fig. 32).

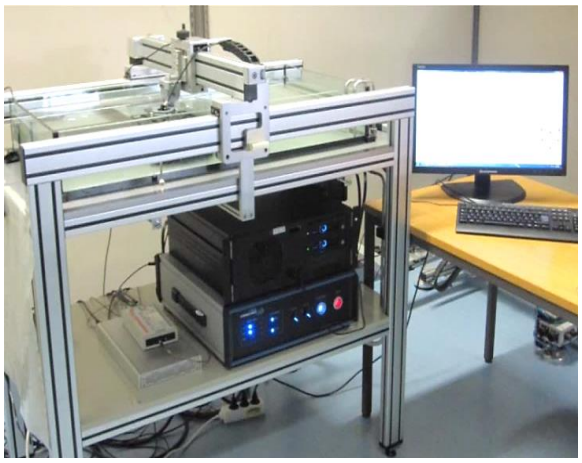

Fig. 32: The ultrasound system specified and constructed by the company I-Deal

IDealviewer is a tool for visualization and analysis of two and three-dimensional data sets. The IDealviewer software is a tool for visualization and analysis of two and three-dimensional datasets. This viewer offers the following built-in features:

- 3D volume view,
- Cut planes,
- Texture mapping,

- Ray casting,
- Maximum intensity projection,
- Marching cubes,
- BDC projections, and
- Amplification and threshold.

The IDealviewer supports datasets, measured by A1040 MIRA based on ultrasonic tomography for non-destructive testing.

The measurement can be performed with conventional or sampling phased array technique.

Theory:

Ultrasound is sound of a pitch too high to be detected by the human ear of the frequency greater than about 18 KHz. Ultrasound waves are mechanical oscillations being transferred into the surrounding area in contrast to electromagnetic waves. Any mechanical wave is composed of oscillations of discrete particles of a material. If the oscillation of the particles have the same direction with the spreading of the wave, it is called a longitudinal wave and the spatial distance between two successive oscillation is called wavelength (see Fig. 33a).

In case of the direction of the oscillation and the propagation are perpendicular to each other, the wave is called a transverse wave (see Fig. 33b). [Blitz 1997; Blitz 1996; Krautkrämer 1990]. This type of wave can only exist in solid materials, while the longitudinal wave can also exist in fluidic and gaseous materials [Krautkrämer 1990].

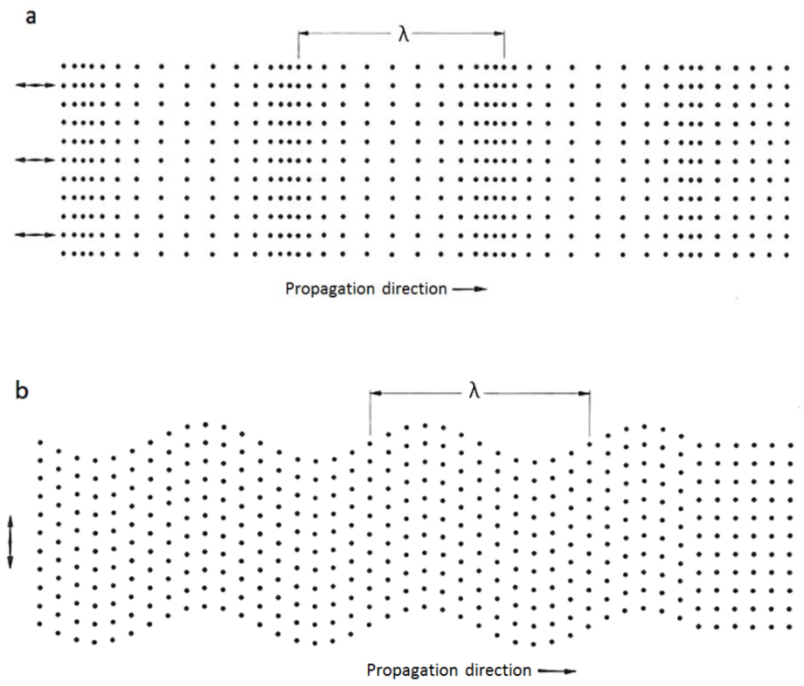

Fig. 33: Mechanical waves, a) longitudinal wave, b) transverse wave [Krautkrämer 1990]

These mechanical waves require a carrier material and cannot exist like electromagnetic waves within a vacuum or any other surrounding without matter. The frequency range being used for ultrasound technical measurement is usually far above the upper human audible limit. Usually frequencies between 1-20 MHz are used but some exceptions apply.

These waves penetrate any material with a speed specific for the material. This is a specific characterization for each material with the same molecular structure. Nevertheless, this value is varying with temperature and is mainly valid for gases and fluids with external pressure.

The sound velocity of the longitudinal wave V_l and the transverse wave V_t can be calculated from the material properties, mostly density which represents mass of the material in relation to its volume [Bolt 1995].

The elastic properties of a material, elastic modulus or Young's modulus (E) and the transverse contraction, Poisson's ratio (υ) and density (ρ) affect the sound velocity.

The sound velocities are calculated by the following equations:

$$V_l = \sqrt{\frac{E}{\rho}} \times \sqrt{\frac{1-v}{(1+v)(1-2v)}} \qquad \text{Eq. 21}$$

$$V_t = \sqrt{\frac{E}{\rho}} \times \sqrt{\frac{1}{2(1+v)}} \qquad \text{Eq. 22}$$

The relation between sound velocity and frequency can be obtained [Krautkrämer 1986]:

$$V = \lambda f \qquad \text{Eq. 23}$$

where

V is the sound velocity [m/s],

f is the frequency [Hz], and

λ is the wavelength [mm].

An ultrasound wave propagates from a surface simulated by a vibration into the interior of the test sample. During the propagation, the existing wave is weakened by internal friction. This phenomenon is called absorption. The highly absorbing materials are used for acoustic damping and vice versa the materials with low absorption do not weaken the ultrasonic wave very much and are well-suited for ultrasonic measurements. Absorption is frequency-dependent. It is increasing with rising frequency on nearly all materials. Besides, mostly in metallic materials, the scattering phenomenon is responsible

for a decrease of amplitudes, i.e. sound attenuation. This scattering means the development of circular waves at obstacles in the dimension of wavelength, e.g. crystal structure or also inhomogeneity.

When an ultrasonic wave arrives at the boundary area of another material, it is principally split into a reflected and a through-transmitted part. The simplest case of perpendicular incidence is shown in Fig. 34.

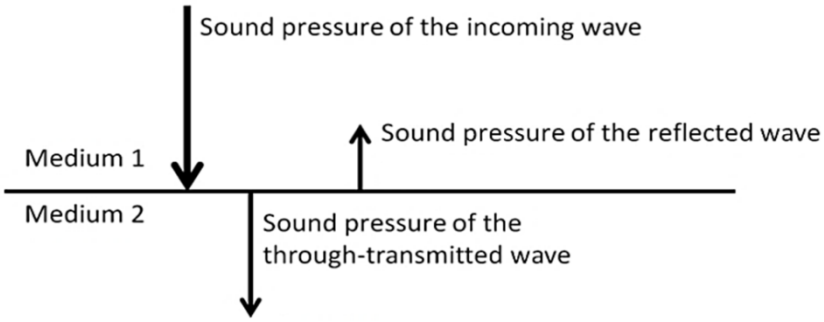

Fig. 34: Ultrasound wave travelling perpendicularl towards a boundary of two media [Deutsch 2002]

The amplitude of the incoming wave is mostly described by the expression of sound pressure. Reflection coefficient Γ and transmission coefficient D^* can be calculated from the acoustic impedance Z of both materials, where the impendence is defined in accordance to Eq. 24:

$$Z = \rho V \qquad \text{Eq. 24}$$

where

ρ is the density of the material [g/m^3], and

V is the speed of sound [m/s].

The other factors being the reflection and transmission ratios are [Bolt 1995]:

$$\Gamma = \frac{Z_2 - Z_1}{Z_2 + Z_1} \qquad \text{Eq. 25}$$

$$D^* = \frac{2Z_2}{Z_2 + Z_1} \qquad \text{Eq. 26}$$

4.2 **Samples**

In order to characterize different properties of CIPP through different methods, various samples are required.

4.2.1 Aging samples

i. Material properties

As mentioned in 1.1.2, UPR and PET materials were examined in this thesis. The UPR for aging samples is the classical isophthalic-based polyester resin MAXPOL[1] (Ortho Neopentyl glycol resins, O-NPG). PET fibers with a diameter about 40 µm and a melting point about 252 °C were used.

MAXPOL is developed for the production of CIPPs in the pipe rehabilitation industry. Fully cured polymer is characterized by high chemical resistance, good mechanical properties and an excellent, long-lasting retention of the properties. The material properties of aging samples are shown in Table 2. These samples have the thickness of 20.5 mm.

Table 2 : Physical and mechanical properties of samples

Materials	Flexural E-Modulus [MPa]	Flexural strength [MPa]	Sealed	Glass transition temperature [°C]	Fiber volume fraction	Density [g/ml]	Profile
UPR/PET	3247	32	yes	120	25%	1.31	DN 1000

ii. Sample preparation

One of the aims of this thesis is to investigate the CIPP samples after manufacturing, installation and during operation. As the CIPP here is completely cured it is not possible to test the samples in condition after manufacturing, because the CIPP is first cured during installation. Since the CIPPs are exposed to water after installation and during operation, in order to investigate the effect of water aging on CIPP samples, a hydrothermal aging process has been applied on the samples. To accelerate the hydrothermal aging, high temperature has been applied. Since the temperature of wastewater in reality may not exceed 70 °C and the high temperature has extra chemical effect on the polymers (depends on the T_g of materials), a temperature of 65 °C has been applied in this thesis.

[1] Maxpol is a thixotropic, filled, not pre-accelerated, UPR based on isophthalic acid / neopentylglycol low exothermic used in liner of the “RS Technik” factory.

As aging samples, three samples 1, 2 and 3 with dimension of 20.0 mm×20.0 mm×20.5 mm were cut into plates (Fig. 35). In order to have a better comparison, one unaged sample as a reference was cut from the CIPP in the same dimension. The unaged sample corresponds to the CIPP after installation and the aged samples correspond to the CIPP during operation.

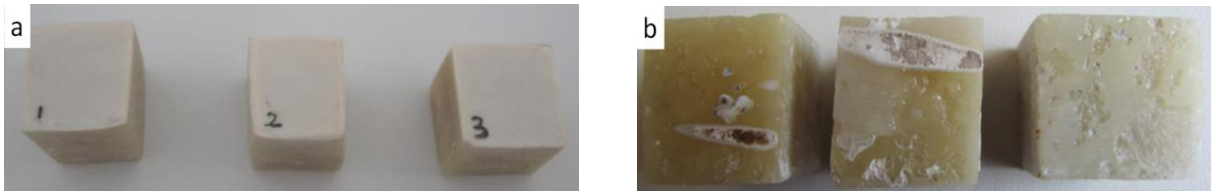

Fig. 35: Aging samples, a) front-side, b) back-side

4.2.2 Nanoindentation and optic microscope samples

i. Material Properties

The same material was used as mentioned in 4.2.1.

ii. Samples preparation

In order to use the nanoindenter and optic microscopy, the surface of the CIPP samples had to be grinded and polished. For this purpose three samples with ground and polished surface have been prepared (Fig. 36). These samples were considered with nanoindenter and optical microscopy once before and once after aging.

Fig. 36: Polishing of CIPP sample

4.2.3 Geometrical defect sample

To check out whether defects in CIPPs can be recognized by microwaves, terahertz and ultrasound methods, some geometrical defects were machined on a CIPP sample.

i. Material properties

The material of the defect samples is the same as mentioned in Table 2 with the thickness of 20.5 mm.

ii. Sample preparation

Flat bottom holes (FBHs) with 10, 5 and 3 mm diameter and depth of 18, 15, 10, 6 and 2 mm were drilled on the back-side of the CIPP UPR/PET sample. Fig. 37 shows the FBHs on the sample. The front-side of the CIPP is available for any tests in the pipe and it is in contact with water. The red circles indicate the positions of the holes on the other side.

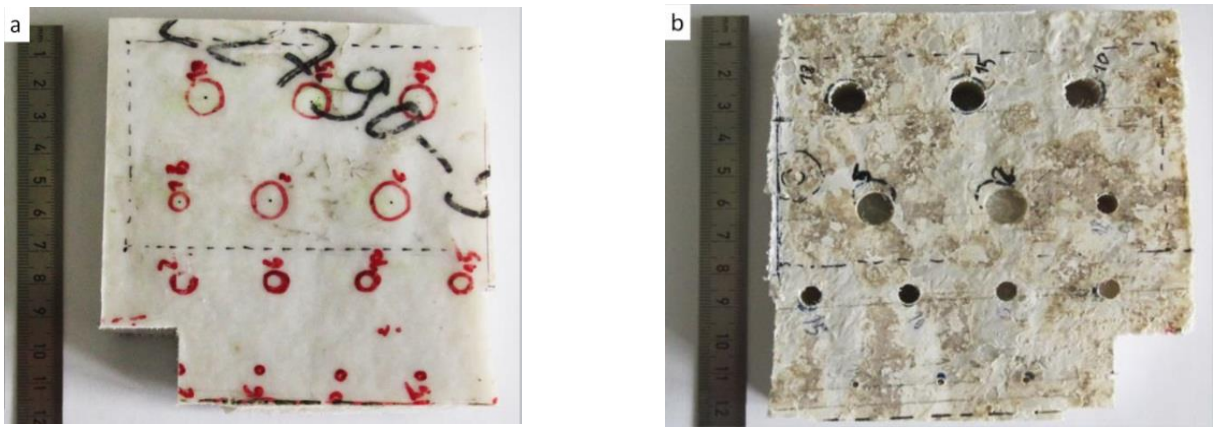

Fig. 37: Flat bottom holes machined on the back-side of a CIPP sample, a) front-side of the CIPP, b) back-side of the CIPP

Fig. 38 with a schematic sketch of the FBHs, shows the diameter and depth of the FBHs. The details of the FBHs can be found in Table 3.

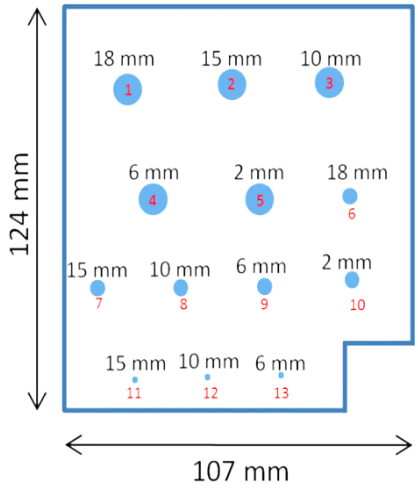

Fig. 38: Schematic sketch of the bottom holes on UP/PET liner

Table 3: Details of geometrical FBHs in CIPP sample

Defect	Diameter [mm]	Depth [mm]
1	10	18
2	10	15
3	10	10
4	10	6
5	10	2
6	5	18
7	5	15
8	5	10
9	5	6
10	5	2
11	3	15
12	3	10
13	3	6

4.2.4 Partially Cured sample

A sufficient curing process on the CIPPs has an important role on their chemical and mechanical properties. The curing and crosslinking process can change the dielectric permittivity and speed of sound in thermoset polymers. Since microwaves and terahertz testing are sensitive to variation of dielectric property and ultrasound testing with respect to the variation of speed of sound, it is reasonable to investigate this property of CIPPs.

i. Material properties

The partially cured sample in this section is made of UPR with carrier material PET as mentioned in Table 2 with a thickness of 8.5 mm. The sample is inhomogeneous and partially cured. This sample is flat and is not manufactured to be used as CIPP, but useful to inspect the process of the curing.

ii. Sample preparation

The sample for this section (see Fig. 39) is partially cured. For microwave measurement a line test was performed in reflection mode. Tests have been done in a line scan from the uncured to cured area. For the terahertz measurement a surface including the cured and uncured area has been scanned. For ultrasound measurement both the line scan and area scan has been done.

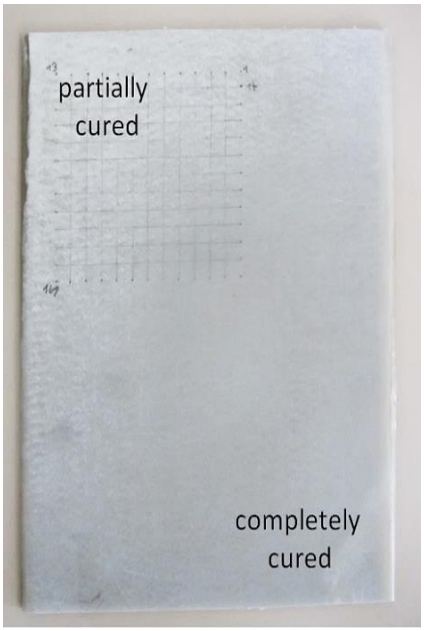

Fig. 39: The partially cured sample

4.3 **Experimental**

4.3.1 Weighing experiments

Due to the exposure of CIPPs to water in reality, they are aged and saturated with water. This is the reason why the samples should become water-saturated. At first the samples were dried in the Nabertherm Controller B150 oven for one hour at 108±3 °C until all initial moisture was removed. The samples were then cooled in a desiccator and immediately weighted with the balance model PCE-AB 200C. This weight recorded refers to the conditioned weight (W_0). Then the samples were immersed in double distilled water at 65 °C. The samples were removed from the water after 24 hours, gently wiped free from surface moisture with a dry cloth and weighted immediately. This weight refers to wet weight (W_w) again. The weighing has been repeated at the end of the first week and every two weeks thereafter until the increase in weight per two-week period by the three descending consecutive weighing reached less than 1% of the total increase in weight average [ASTM International D 570 – 98]. The samples were then considered substantially saturated. After testing the samples in wet state, they were dried again in the oven for 1 hour and cooled down in a desiccator.

4.3.2 Optical microscopy experiments

The samples in 4.2.2 were observed by the Leica DM6000 M once before and once after aging. It was tried to capture the same area of the sample before and after aging to make the comparison easier.

4.3.3 Nanoindentation experiments

Hysitron TriboIndenter® with the Performech™ controller and a Berkovich diamond tip has been used in this thesis to perform nanoDMA measurement for studying the creep resistance and viscoelastic

properties of the samples. The tip area function was defined with the conventional method of fused quartz calibrations. All nano indents, creep and sweep, were performed with the same initial loading rate of 200 μN/s followed by a holding time at the maximum force of about 200 μN and unloading rate of −200 μN/s.

Conditions of creep test:

Hold time: 300 seconds, load amplitude: 3-5μN, displacement amplitude: 1-2 nm, frequency: 220Hz

Conditions of sweep test:

Load amplitude: 3-5μN, displacement amplitude: 1-2 nm, frequency: 10 Hz to 200 Hz

4.3.4 Microwave experiments

A VNA allows an accurate and broadband microwave measurement of the phase and amplitude or real and imaginary parts. A horn antenna (aperture approximately 6 mm×9 mm) was used both as transmitting and receiving antenna. The distance between the sample and the antenna was 50 mm.

4.3.4.1 *Aging experiment through microwaves*

The aging samples (see 4.2.1) were characterized with microwave in time domain (75 – 100 GHz) in reflection mode before aging and immediately after aging when the samples are still wet (Fig. 40). After that, the samples were placed in the oven at 108±3 °C for one hour. They were allowed to cool down in a desiccator, and then they were characterized with microwaves one more time. Every sample is tested on different 20 points.

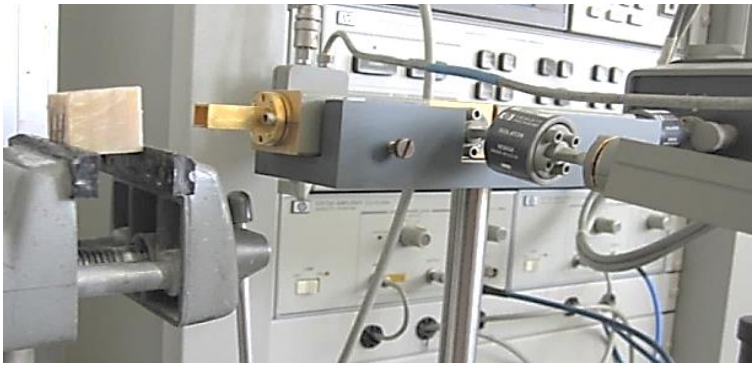

Fig. 40: Set up of VNA test of aging samples in reflection mode

4.3.4.2 *Geometrical defects experiment through microwaves*

The test procedure was performed with a two-axis scanner across the fixed antenna (see Fig. 41) with a scan area 110 mm×90 mm in reflection mode. A computer program controlled the measurement data acquisition of the VNA and the movement of the sample in the x- and y-axis. The control parameter S_{11} has been applied to each measurement position for 201 frequencies between 75 and 100 GHz. The

measurement data have been stored on a computer and then processed using C++ programs. In this case, the evaluated volume starts with the scan surface at the location of the antenna aperture and ends in the beam direction beyond the sample back-wall. The technique of the synthetic aperture radar (SAR) was used to increase the lateral resolution [Moll 2013].

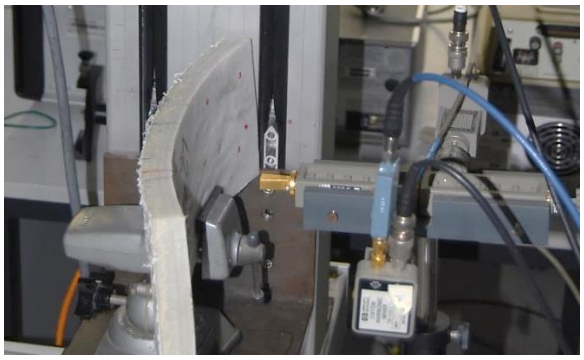

Fig. 41: Set up of VNA test of CIPP sample with FBHs in reflection mode

S Parameter

S parameters are used predominantly in the context of microwave frequencies because they provide a simple notation with exact data regarding the device performance in achievable environments. They are a ratio of two complex quantities, which means magnitude and phase. The S parameter numbering convention is: $S_{out\ in.}$ where the first number (out) refers to the port where energy is emerging and the second number (in) names the port of incidence. In Fig. 42 "a" is the incident wave and "b" is the emerged wave and the numbers refer to reflection or transmission mode (1 is reflection and 2 is transmission). The energy in this graph can only be applied at the a_1 node. S_{11} refers to the reflection mode (b_1/a_1) and S_{21} is the parameter of transmission mode (b_2/a_1). Fig. 42 shows a_1 as the incident wave, b_1 as the reflection of a_1 and b_2 as the transmission of a_1.

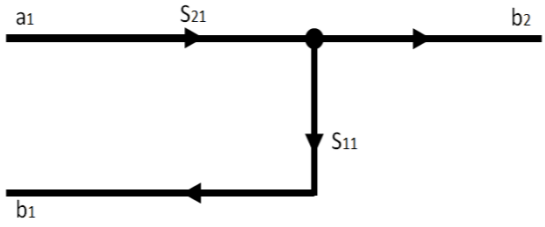

Fig. 42: S parameter flow graphs, reflection/transmission test set

Theory of SAR algorithm

The geometric resolution is a measure of the separability of two nearby objects with the same radar cross section and is given as the minimum distinguishable distance in space, angle or speed. These variables determine the resolution cell [Soumekh 1999].

In radar, the axial resolution δ_e depends on the bandwidth or pulse duration of the transmitted signal [Duersch 2004]:

$$\delta_e = \frac{c}{2B_e} \qquad \text{Eq. 27}$$

where

c is the speed of light [m/s], and

B_e is the bandwidth of antenna [Hz].

The azimuth resolution δ_a depends on the azimuth size of the antenna and increases with liftoff (distance between target and radar) [Duersch 2004].

$$\delta_a = \theta_a r_0 = \frac{\lambda}{d_a} r_0 \qquad \text{Eq. 28}$$

where

θ_a is the half width at half maximum (HWHM),

r_0 is the liftoff [m],

d_a length of antenna [m], and

λ is the wavelength [m].

An improvement in the azimuth resolution of an aperture is only possible within limits with a predetermined distance to the target and the wavelength of the measured signal by increasing the antenna aperture, which is specified by the application and installation situation. Synthetic aperture radar is a moving aperture radar along an imaginary aperture and all received echoes are stored in magnitude and phase (Fig. 43).

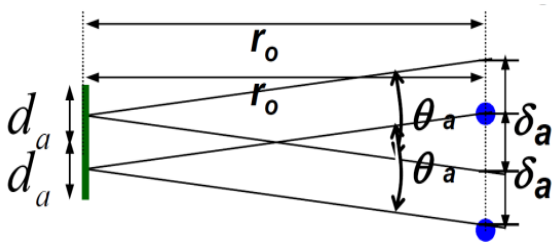

Fig. 43: Schematic of synthetic aperture

The synthetic aperture is created by the fact that a point shaped target is within the lobe of a real antenna, which moves along the flight path (Fig. 44), is illuminated and all received echoes are stored in magnitude and phase. This covered during the illumination of the target flight path is called synthetic aperture. Because of the thereby changing distance between the antenna and target, the received echo signal with respect to the transmission signal to a Doppler frequency shift is calculated. Each target is identified by its characteristic Doppler frequency response and can in principle be distinguished from adjacent locations.

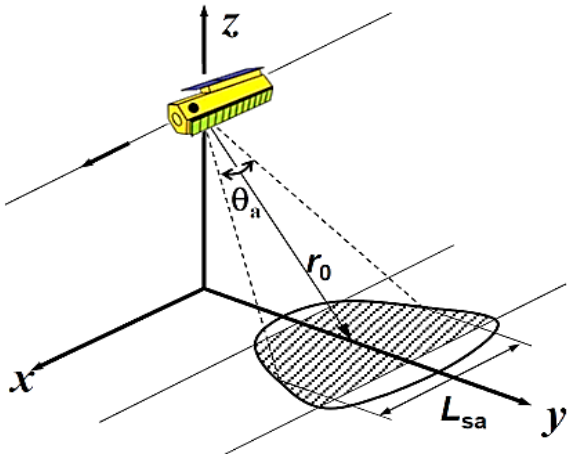

Fig. 44: Schematic of azimuth resolution and length of synthetic aperture

$$L_{sa} = \theta_a r_0 = \frac{\lambda}{d_a} r_0$$ Eq. 29

where

L_{sa} is length of the synthetic aperture [m].

$$\theta_{sa} = \frac{d_a}{2r_0}$$ Eq. 30

where

θ_{sa} is the beamwidth of the synthetic antenna.

$$\delta_a = \frac{d_a}{2}$$ Eq. 31

where

δ_a is azimuth resolution of a synthetic aperture radar [m].

Therefore the azimuth resolution of a radar with synthetic aperture is independent of wavelength and the range [Duersch 2004; González-Partida 2008; Soumekh 1999].

According to the Eq. 27 the axial resolution of the VNA in this project follows:

$$\delta_e = \frac{c}{2B_e} = \frac{2.998 \times 10^8}{2 \times 25 \times 10^9} \approx 6mm$$

The best lateral resolution is equal to the wavelength. In this case in the W-band up to 100 GHz, the wavelength corresponding to resolution is 3 mm.

4.3.4.3 *Curing experiment through microwaves*

Along the 11 points of the blue line being stepwise 1.41 mm apart (see Fig. 45) measurements were taken through the VNA in reflection mode. The control parameter S_{11} (reflection mode) at each measurement position has been applied for 201 frequencies.

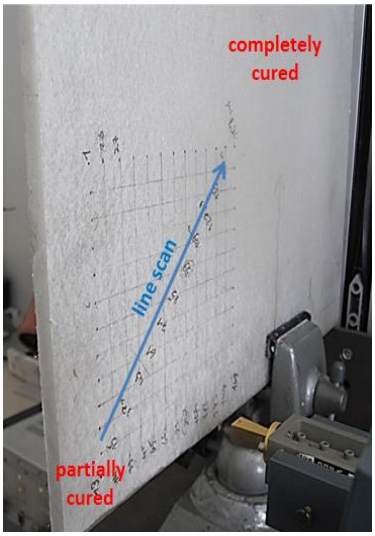

Fig. 45: VNA measurement on partially cured CIPP in reflection mode with horn antenna

4.3.5 Terahertz experiments

All THz measurements have been done in transmission mode. In the THz measurements the axial resolution according to the 2 THz bandwidth is equal to 0.075 mm. The best reachable lateral resolution is equal to the wavelength, which means 0.1 mm in this case.

4.3.5.1 *Aging experiment through THz*

Three wet aged samples in comparison with one unaged sample were scanned through the THz system (see Fig. 46), in steps of 1 and 0.6 mm. The lateral resolution in this test is therefore equal to 1 and 0.6 mm.

After that, the experiment was repeated with the aged dry samples (the wet samples dried in furnace and cooled down) and one unaged sample.

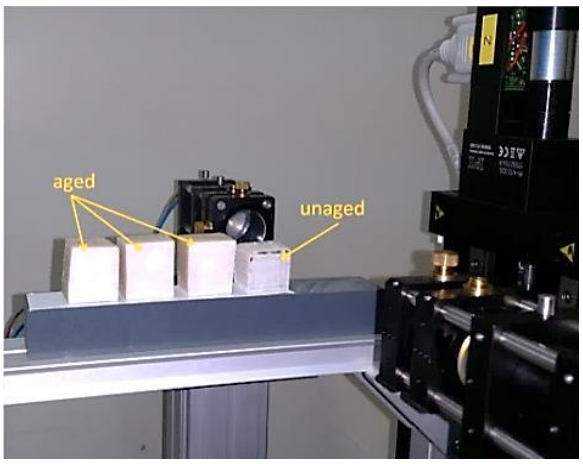

Fig. 46: Three aged samples left and one unaged sample right on x-y scanner of THz system in transmission mode

4.3.5.2 *Geometrical defects experiment through THz*

The sample explained in 4.2.3 was tested with the THz system in transmission mode in a scan area of 127 mm×118 mm in steps of 0.25 mm. The best possible lateral resolution is therefore in the range of 0.25 mm. The question is if one can reach this resolution or not, which will be answered in a test. The sample was set on the x-y scanner such that the FBHs were to the side of the detector (see Fig. 47).

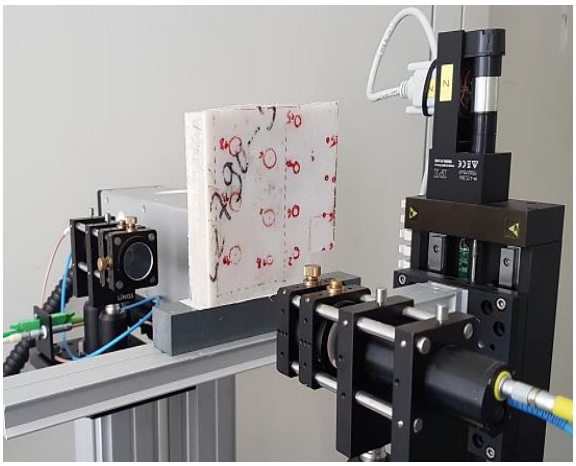

Fig. 47: The machined flat bottom holes sample on the x-y scanner of the THz system in transmission mode

4.3.5.3 *Curing experiment through THz*

An area of 140 mm×220 mm including a cured and an uncured area was scanned in steps of 1 mm with the THz system transmission mode to detect an insufficient curing process on the sample (see Fig. 48).

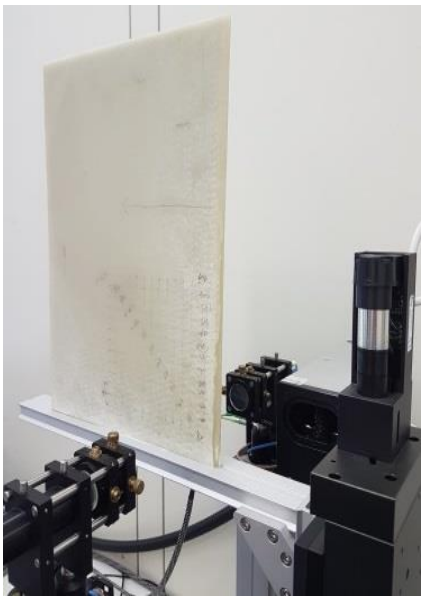

Fig. 48: The partially cured sample on the x-y scanner of the THz system in transmission mode

:

4.3.6 Ultrasound experiments

4.3.6.1 *Aging experiment through US*

Three aging samples and one unaged sample of CIPP explained in 4.1.2 were immersed in water to be tested with ultrasound in reflection mode (Fig. 49). The measurement was done on aged samples once wet and once dry. In these measurements the conventional method with the 2.25 MHz transducer was used.

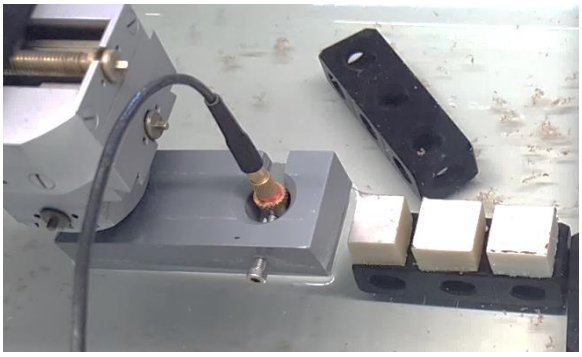

Fig. 49: Set-up of immersed in water high-frequency ultrasonic measurement, testing the aging samples

The speed of sound in the material should be known and this parameter needs to be entered in the system at the beginning of the scanning. In order to calculate the speed of sound, one should calibrate the system with the known thickness and measure the time of flight to calculate the speed. In aging experiment the speed of sound was calculated to be 2600 m/s.

4.3.6.2 *Geometrical defects experiment through US*

The CIPP sample with flat bottom holes was immersed in water at room temperature and tested in reflection mode at 2.25 MHz scaning area of 120 mm×120 mm with the same speed of sound in 4.3.6.1 (Fig. 50).

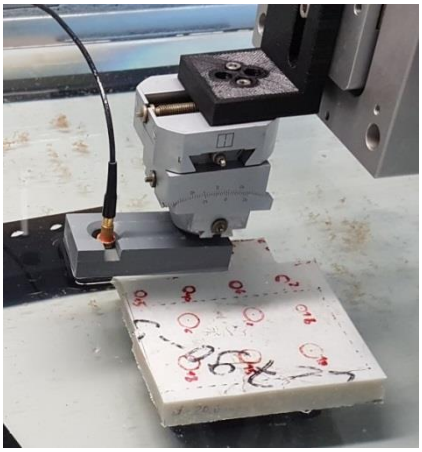

Fig. 50: Set-up of immersed in water high-frequency ultrasonic measurement, testing the sample with FBHs

4.3.6.3 *Curing experiment through US*

The curing process of thermosetting polymers follows the variation in the storage modulus and loss modulus. The sound velocity of a longitudinal wave and damping of this wave in the medium are connected with the longitudinal storage modulus and the longitudinal loss modulus as follows:

$$E_l^{'} = (V_l)^2 \rho \quad \text{Eq. 32}$$

$$E_l^{''} = 2(V_l)^3 \rho \alpha^{long} / \omega \quad \text{Eq. 33}$$

where

$E_l^{'}$ is longitudinal storage modulus [g/m.s^2],

$E_l^{''}$ is longitudinal loss modulus [g/m.s^2],

V_l is longitudinal velocity [m/s],

ρ is density [g/m^3],

ω is the angular frequency [Hz], and

α^{long} is the longitudinal damping [1/m].

It can be summarized as the complex longitudinal modulus E^*:

Eq. 34

$$E_l^* = E_l^{'} + jE_l^{''}$$

In order to monitor the curing process through an ultrasonic system, two parameters are needed: the sound velocity and the damping. To calculate the sound velocity, one should know the thickness of the material and the traveling time [Karbhari 2013]. The partially cured sample was immersed in water at room temperature and tested in reflection mode with 5 MHz with the scan area of 170 mm×190 mm marked in Fig. 51. In addition, the sound velocity at the different 11 points was measured.

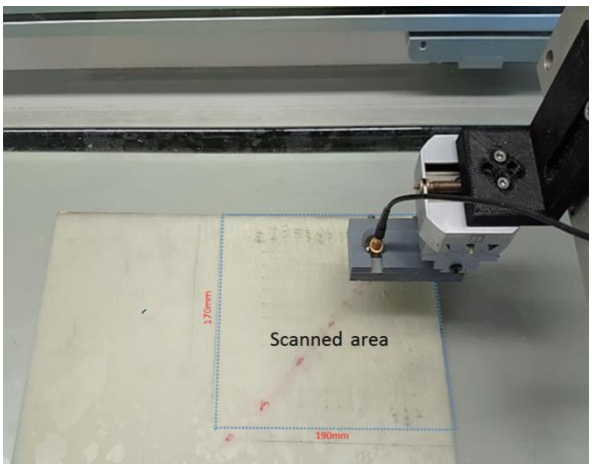

Fig. 51: Set-up of immersed in water high-frequency ultrasonic measurement, testing the partially cured sample

5 Results

5.1 Results of weighing

The determination of the mechanism and the level of degradation on composites are dependent on the hydrothermal conditions. They include, for example, the duration of a hydrothermal test, the chemicals contained in the water and its temperature. To simplify the chemical conditions of water, double-distilled water has been used, and the hydrothermal aging was performed until the samples reached the saturation level. It is assumed that the samples shall then be considered substantially saturated when the increase in weight per two-week period by the three consecutive weighing averages (Ave.) is less than 1% of the total increase in weight. This level of saturation was reached after 8 weeks (1344 hours) of hydrothermal aging. Fig. 52 shows the total increase in weight measurements. W_w is the wet weight and W_0 is the conditioned weight.

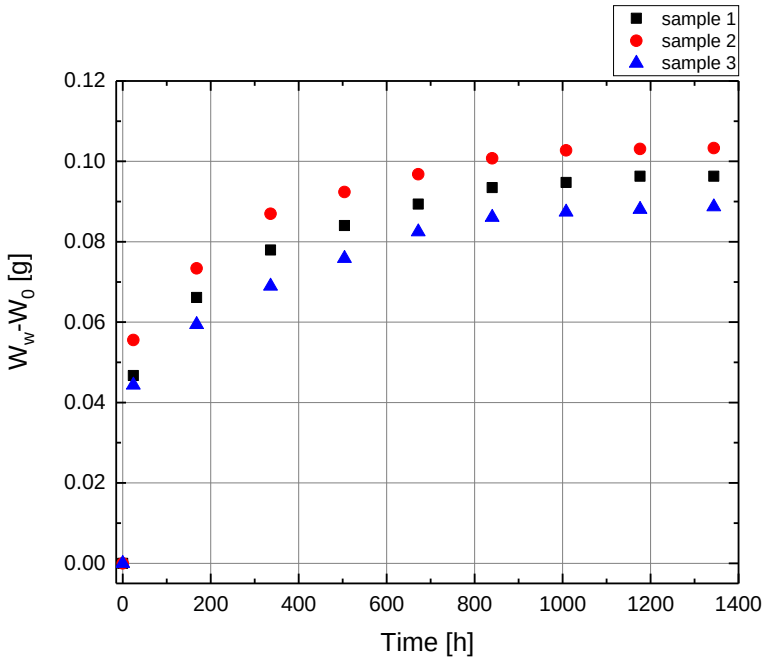

Fig. 52: Weight gain curves at 65 °C of three aging samples, showing total weight gain vs. time

5.2 Results of optical microscopy

With the help of optical microscopy, degradation after hydrothermal aging is detectable. Fig. 53a, b show the CIPP surface before the aging and Fig. 53c, d after aging in different magnification. In order to investigate the changes in the matrix, fibers and interfaces, it was tried to inspect the same area of the surface before and after aging. The black parts in the fiber area in Fig. 53a, c and d marked in red

circles appeared after polishing the sample with a black textile. Even after cleaning with water and alcohol, some of these color-changes stayed in the fiber area.

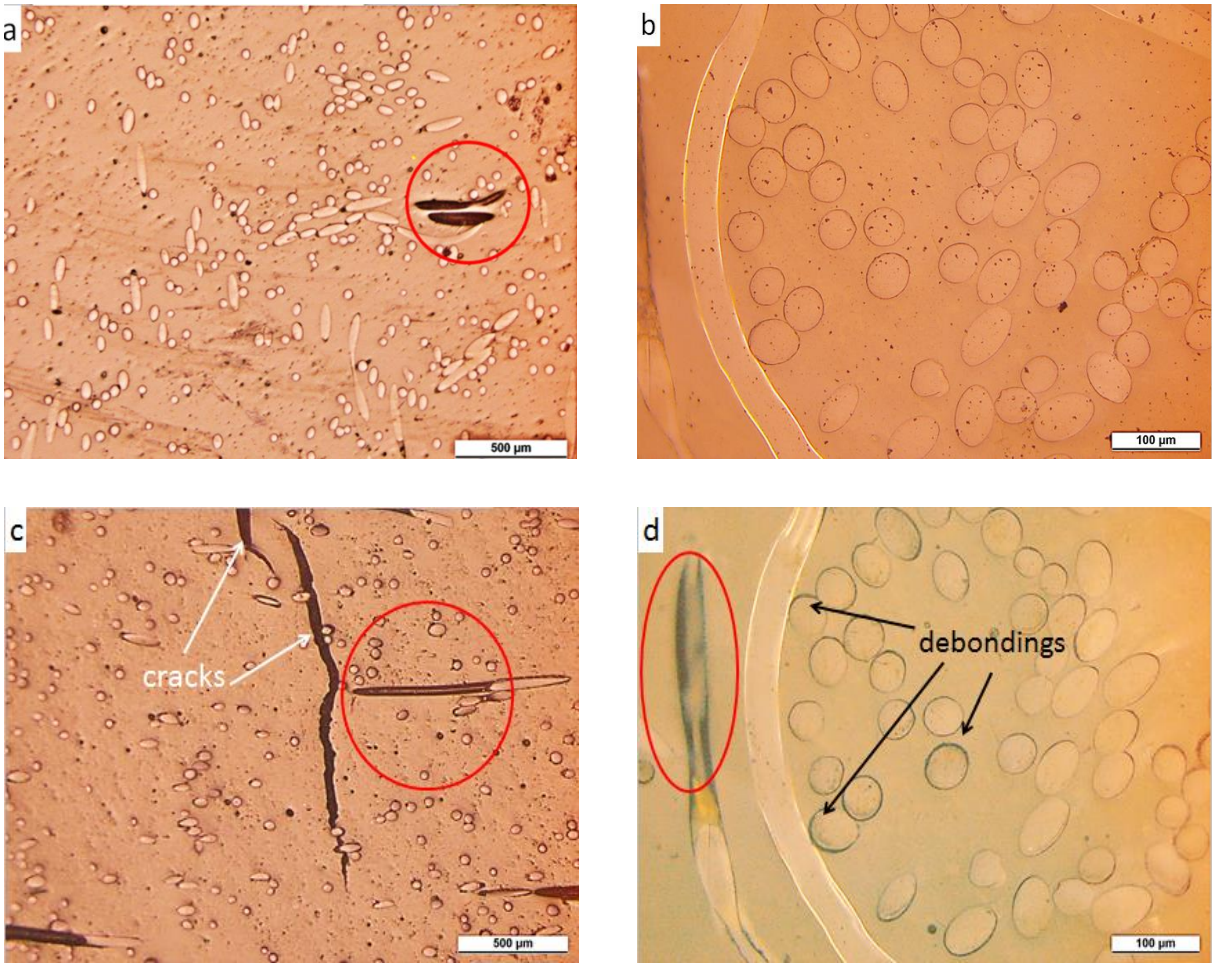

Fig. 53: Optical microscopic observation, a), b) before aging, c) matrix osmotic cracking after aging and d) interfacial debonding after aging

5.3 **Results of nanoindentation**

In the introduction, different models were mentioned for characterization of the tip-viscoelastic material interactions. However, during this work the generalized Voigt model was used for analysis of the data due to its successive results referenced in other publications [Cohen 2013; Sahu 2018)]. Based on the Voigt model, the reduced storage modulus ($E_r^{'}$), the reduced loss modulus or energy loss ($E_r^{''}$) and the damping (δ) in the dynamic mechanical analysis method is calculated as follows [Zamanzade & Barnoush 2014)]:

$$E_r^{'} = \frac{K_s\sqrt{\pi}}{2\sqrt{A_c}} \qquad \text{Eq. 35}$$

$$E_r^{"} = \frac{\omega C_s \sqrt{\pi}}{2\sqrt{A_c}}$$ Eq. 36

$$tan\,\delta = \frac{E_r''}{E_r'} = \frac{\omega C_s}{K_s}$$ Eq. 37

where

K_s is the storage stiffness of the sample [N/m],

A_c is the contact area [m^2],

ω is the angular frequency [Hz], and

ωC_s is the loss stiffness of the sample [N/m].

The $E_r^{'}$ relates to the stiffness of the material, or the in-phase response of the material to the applied force. This modulus relates the elastic recovery of the sample, which is the amount of energy recovered from the sample subsequent to a loading cycle. The Young's modulus (which is the slope of the initial part of a stress-strain curve) and storage modulus are conceptually similar but they are not the same. Therefore, Young's modulus has not necessarily been the same value as the storage modulus similar to other elastic concepts like shear, bulk and compressive moduli. In the case of linear elastic materials (e.g. metals or ceramics) the term elastic modulus is used which is similar to the storage modulus in the viscoelastic materials. Additionally, the term reduced elastic modulus (not elastic modulus) is commonly used in the case of nanoindentation tests, because the elastic deformation of the diamond tip should be considered as well, for exact definition of the elastic modulus of the samples. The measured $E_r^{'}$ of the samples could be related to its storage modulus and Poisson's ratio (0.38-0.40) and the indenter (E_T and υ_T) according to the following equation:

$$\frac{1}{E_r^{'}} = \frac{1-v^2}{E^{'}} + \frac{1-v_T^2}{E_T}$$ Eq. 38

Dissipation of energy in a material under cyclic load is called damping. It basically represents the ability of a material on absorbing energy. It varies with the state of the material, its temperature, and with the frequency. The $E_r^{"}$ relates to the damping behavior of the material and is observed by the time lag between the maximum force and the maximum displacement. This damping is the amount of energy put into the sample during the indentation that is dissipated by various processes that facilitate energetic losses, primarily heat generation [Zamanzade, Vehoff 2014].

The calculated storage and loss moduli are the broadly used model-dependent quantities that could be used for describing material mechanics [Dokukin 2015]. There is a strong demand for a DMA

technique capable of measuring the dynamic moduli of polymers. Polymer databases of the storage and loss moduli used in industry are mostly limited to 200 Hz [Dokukin 2015].

After this, the terms of elastic modulus, storage modulus and loss modulus refer to the reduced one. In all the presented nanoindentation results in creep and sweep tests, each point represents the average of three tests among the 50 indents in the matrix, fiber and interphase (Fig. 54).

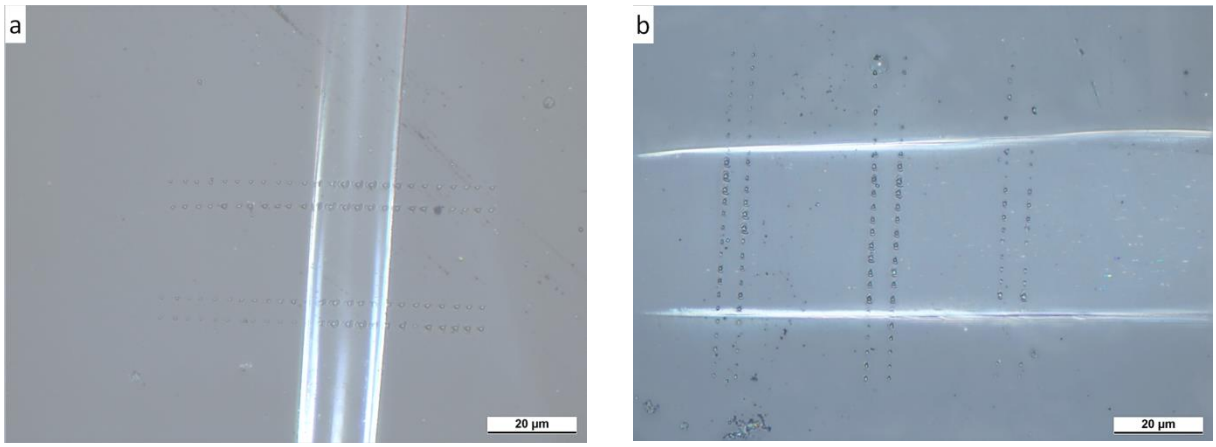

Fig. 54: Optic microscopic image of the creep and sweep test on the matrix and fiber and interphase of the CIPP sample, a) horizontal test, b) vertical test

5.3.1 Frequency sweep test

The modulus-frequency plots are important because they explain how a material changes as frequency changes. For viscous materials, this can give useful information about its flow. Fig. 55 shows the changes of storage modulus of matrix as a function of the applied dynamic frequencies. Over the frequency range tested, the storage modulus in matrix and fiber decreases after aging in wet condition and it reverses back to the initial amount after drying (Fig. 55a, b).

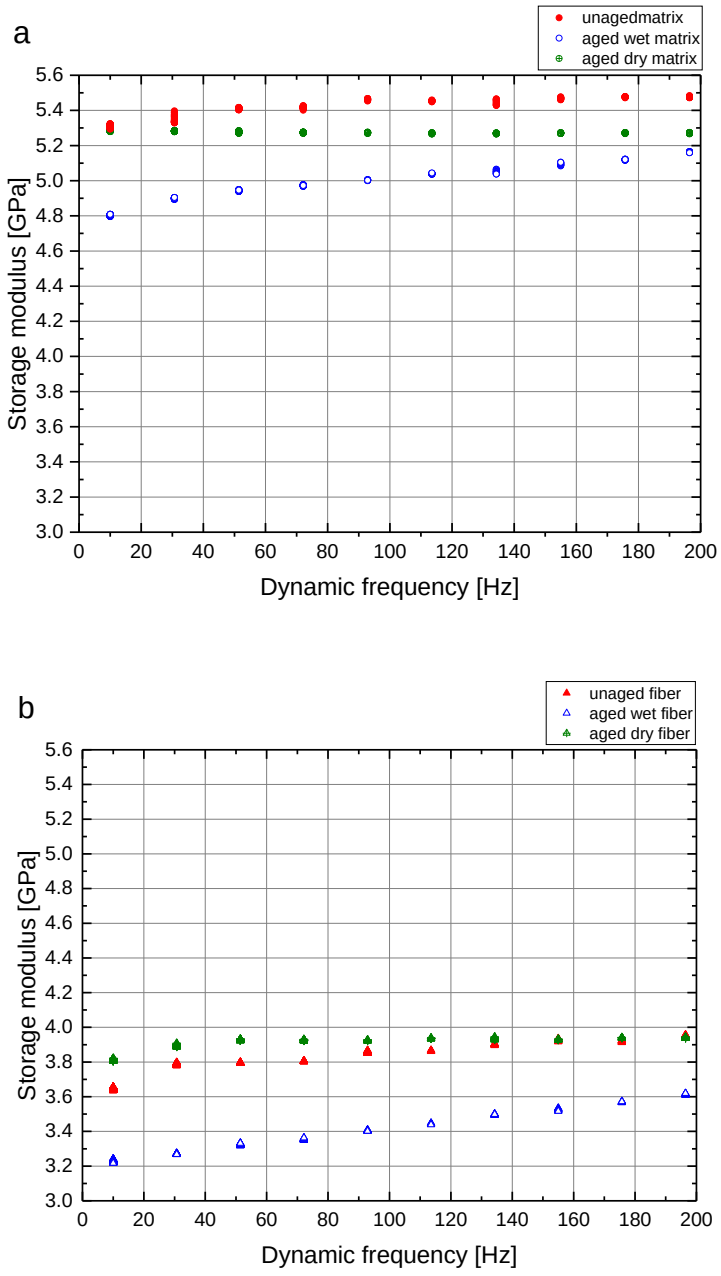

Fig. 55: Sweep test, average of storage modulus of three tests vs. frequency at three conditions: unaged, aged wet and aged dry a) matrix and b) fiber

On the contrary, in Fig. 56a, b the aging increases the loss modulus in wet condition and after drying the E″ reverses back to the primary amount.

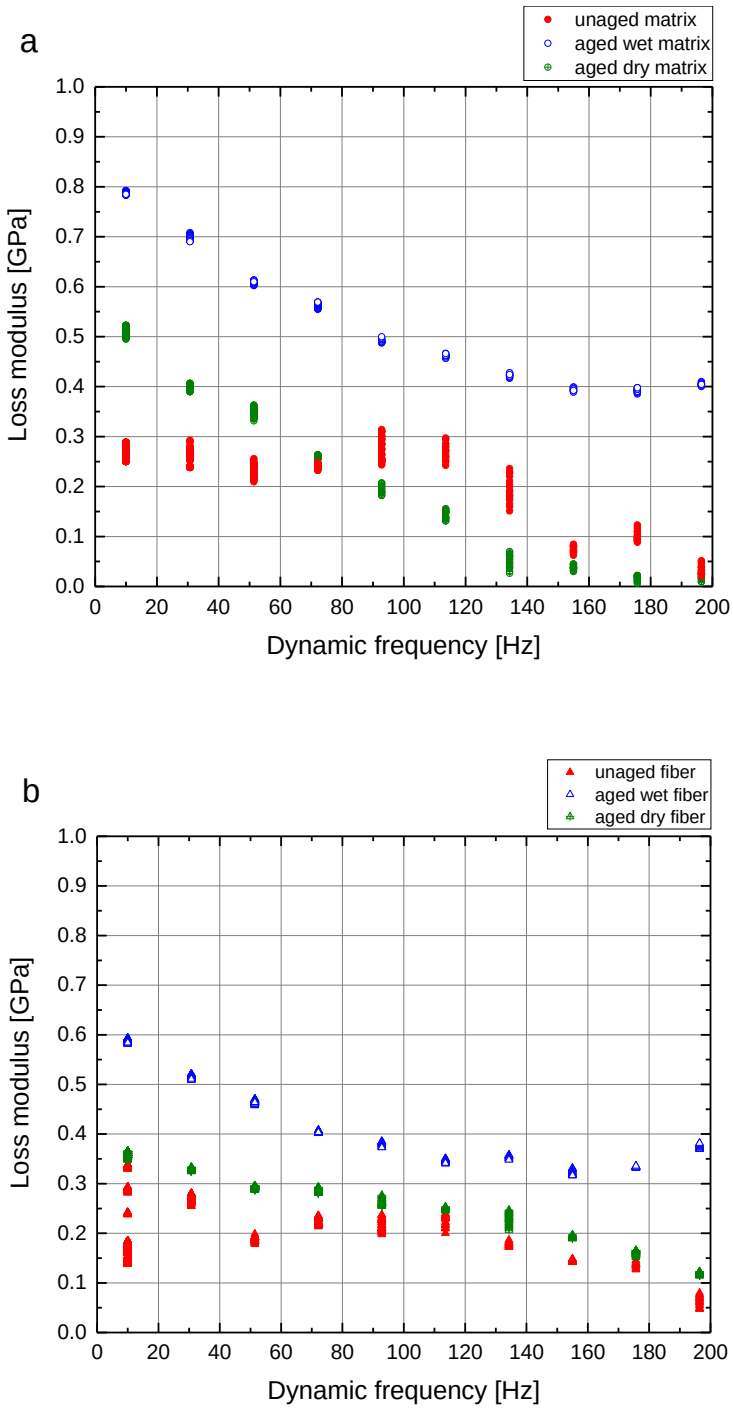

Fig. 56: Sweep test, average of loss modulus of three tests vs. frequency at three conditions: unaged, aged wet and aged dry, a) matrix, b) fiber

High values of tanδ at low frequencies in all cases in Fig. 57 indicate high energy dissipation at low frequencies. This figure shows higher damping in wet condition, but almost the same damping in unaged and aged dry condition in both matrix and fiber.

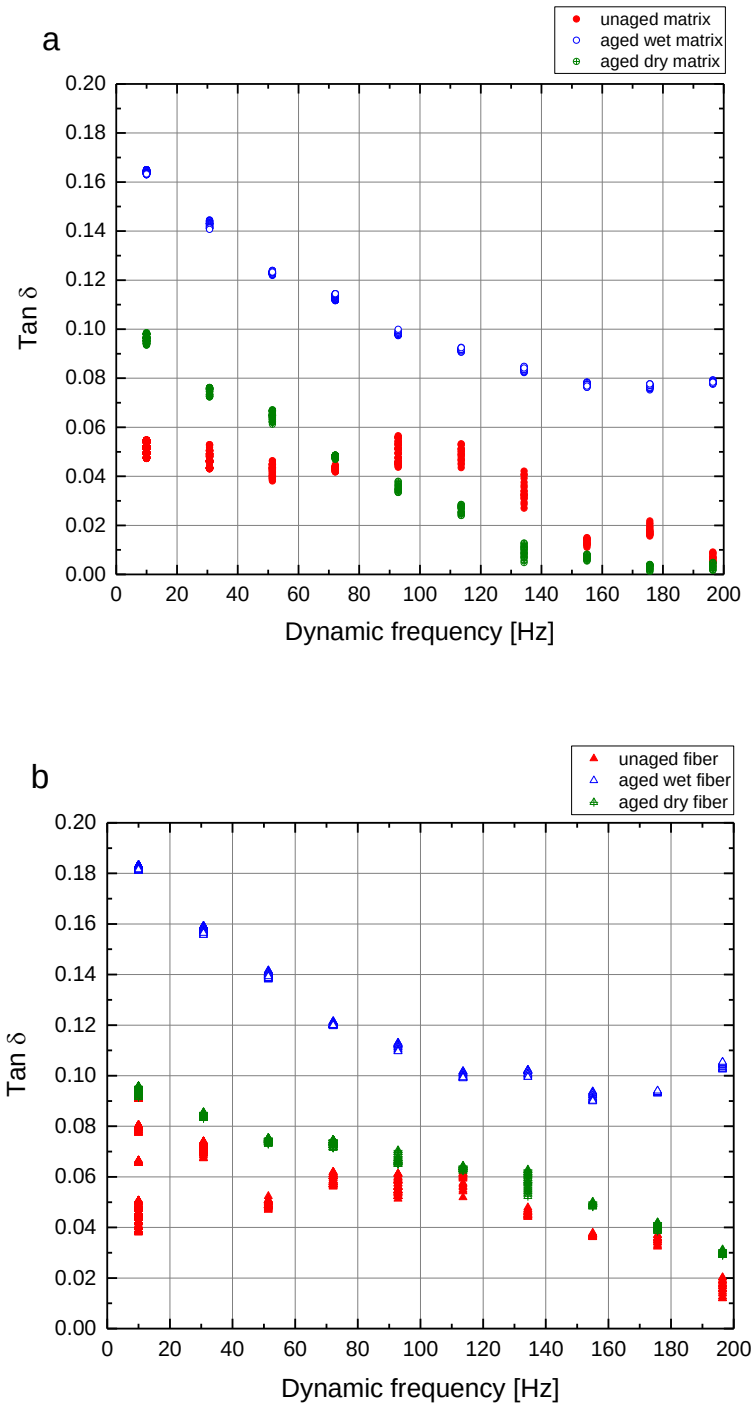

Fig. 57: Sweep test, average of tanδ of three tests vs. frequency at three conditions: unaged, aged wet and aged dry, a) matrix, b) fiber

5.3.2 Creep test

The creep property of materials is a time dependent process which depends on the applied load and temperature. To study the creep behavior of fibers and matrix, a 300 seconds reference creep test was

performed at room temperature at a constant force of 200 μN. Fig. 58 and Fig. 59 show some representative creep curve at three different states i.e. unaged, aged wet and aged dry. In all cases, three distinct regions are clear: primary or transient, secondary or steady-state stage and tertiary or stable stage. In Fig. 58a, b, the primary stage could be defined by rapid increase in displacement and hence reduction of the calculated hardness (Fig. 59a, b). The secondary stage in Fig. 58a, b shows a constant creep strain rate $\frac{\Delta(\text{indent displacement})}{\Delta t} = \text{constant}$ value till it reaches zero in the stage three. Creep behavior of a polymer depends on many different material features like viscoelastic properties, bond rupture and chain slippage [Spathis 2012].

The relation between the indent displacement and the hardness in Fig. 58 and Fig. 59 can be explained with the aid of the following equation:

$$H = \frac{P}{A_c} \qquad \text{Eq. 39}$$

where

H is the hardness [Pa],

P is the maximum applied force [N], and

A_c is the contact area [m^2].

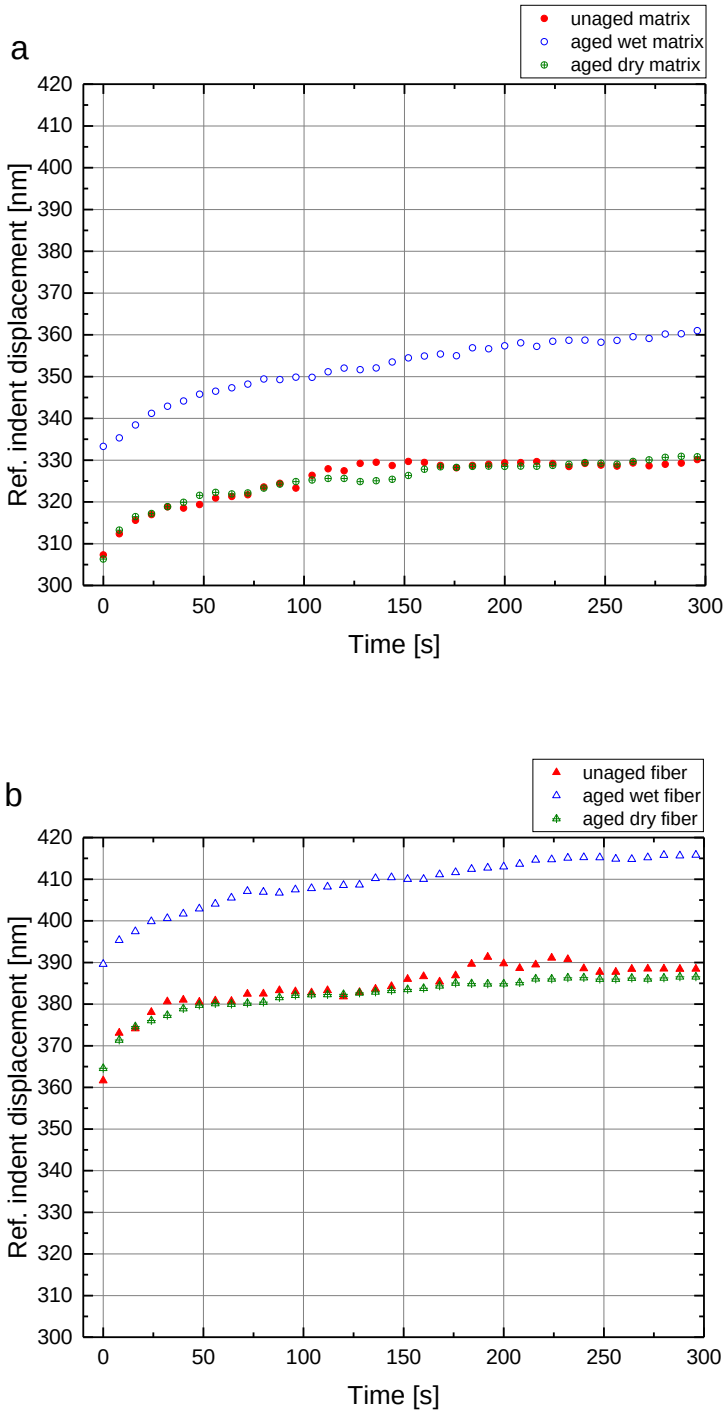

Fig. 58: Creep test, average of ref. indent displacement of three tests vs. time at three conditions: unaged, aged wet and aged dry, a) matrix, b) fiber

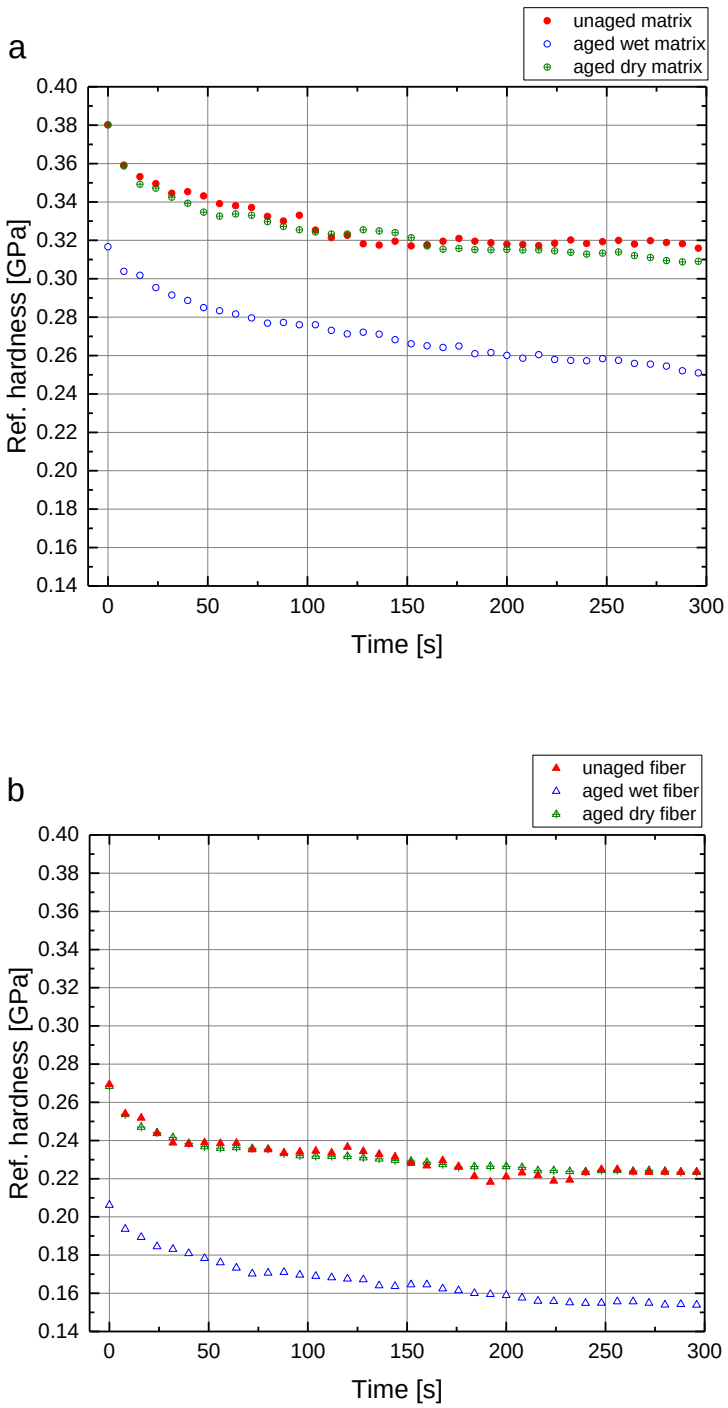

Fig. 59: Creep test, average of ref. hardness of three tests vs. time at three conditions: unaged, aged wet and aged dry, a) matrix, b) fiber

5.4 **Results of microwaves**

5.4.1 Aging

Fig. 60a shows the time domain reflectometry signal of three samples before aging and after aging once moist and then after drying in oven. Each signal represents an average of 20 measurements of every sample. Every signal contains 4 peaks. The two first peaks belong to the begin and the end of

the horn antenna, which are unchangeable in every measurement. The third peak refers to the front-wall and the last one to the back-wall of the sample. Fig. 60b shows the average of 3 samples in every aging condition. The curves have been plotted from the time 400 ps because the first peak of the antenna appears at 450 ps. During 0 to 450 ps, microwaves propagate in the waveguide, therefore the signal gives no useful information.

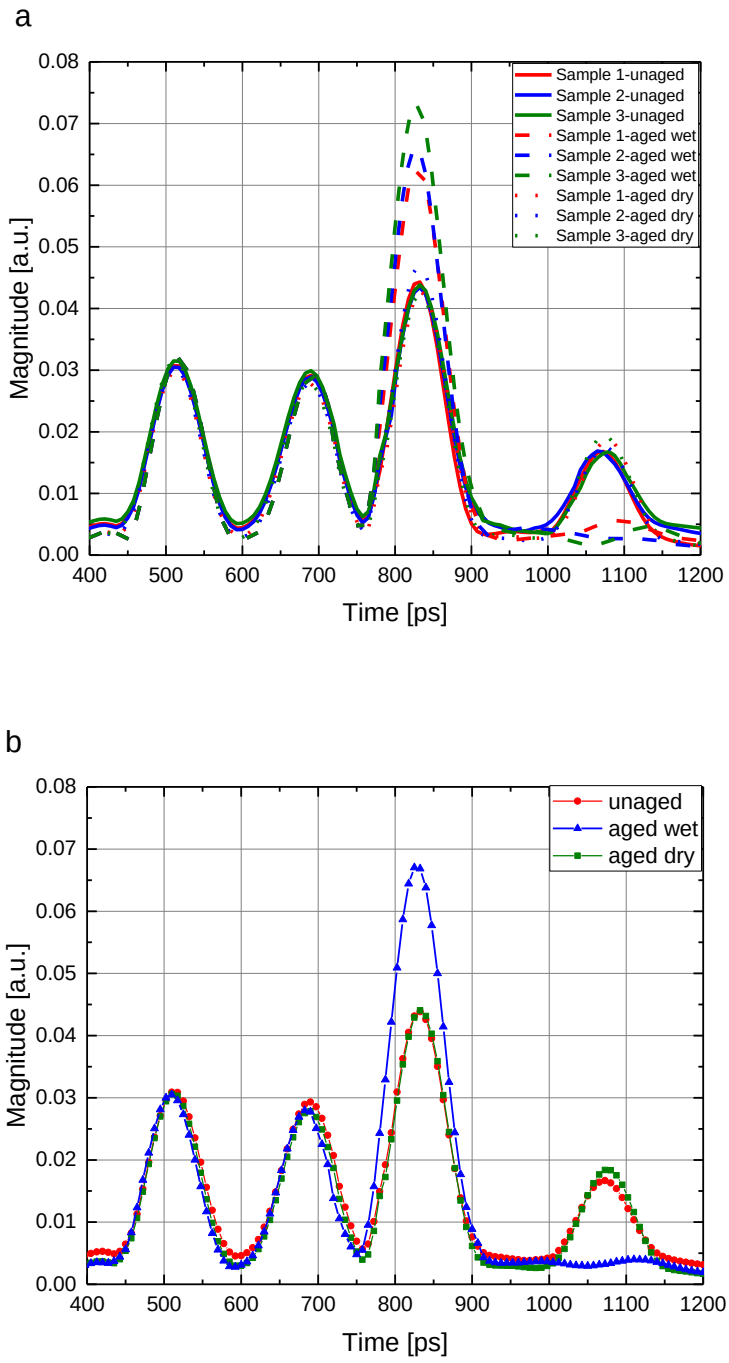

Fig. 60: Reflection measurement in time domain mode, a) three samples unaged, aged wet and aged dry, b) the signal average of three samples in three different conditions. The values are displayed in arbitrary units.

It is seen that the existence of water in wet condition is obvious in both front and back-wall echoes of the samples.

5.4.2 Geometrical defects

The geometrical defects on a CIPP sample have been tested through the microwave method. Fig. 61a shows the front-side of the sample, which faces to the microwave antenna. The flat bottom holes are marked in the image with numbers from 1 to 10 to distinguish them better in the signal imaging. The signal amplitudes in the form of cross sectional images of the captured volume parallel to the scanning surface, and thus parallel to the sample surface (Fig. 61), are analogous to a C-scan in the ultrasonic test. The amplitudes in the region of the sample are beginning from the front-wall surface in the perpendicular direction to the back-wall surface. At first the deepest FBHs with 18 mm depth in the Fig. 61b are seen, then the FBHs with 15 mm in Fig. 61c, after that the FBHs with 10 mm in the Fig. 61d are observed. At the end in Fig. 61e, f the FBHs with 6 mm and 2 mm depth are detected with passing the time. toward the back-side (Fig. 61f).

In the deeper layers, close to the back-wall, increasing noise appears due to the roughness and superimposed signals in the displaying of the FBHs (Fig. 61e, f). These FBHs with lower depths are more difficult to be detected because of the noise of the roughness of the back-wall and also the more attenuation of the signals due to the more damping in the material.

With the help of the SAR technique and improvement of the lateral resolution, the FBHs with 10 mm diameter are well detectable, except for the FBH with 2 mm depth which is not visible well because of the back-wall roughness (Fig. 61f). The 5 mm diameter FBHs are just detectable with 18, 15 and 10 mm depths. The clarity of the amplitude signal analysis is good enough to represent the diameters of the FBHs with the exception of FBHs with 6 and 2 mm depth (Fig. 61e, f).

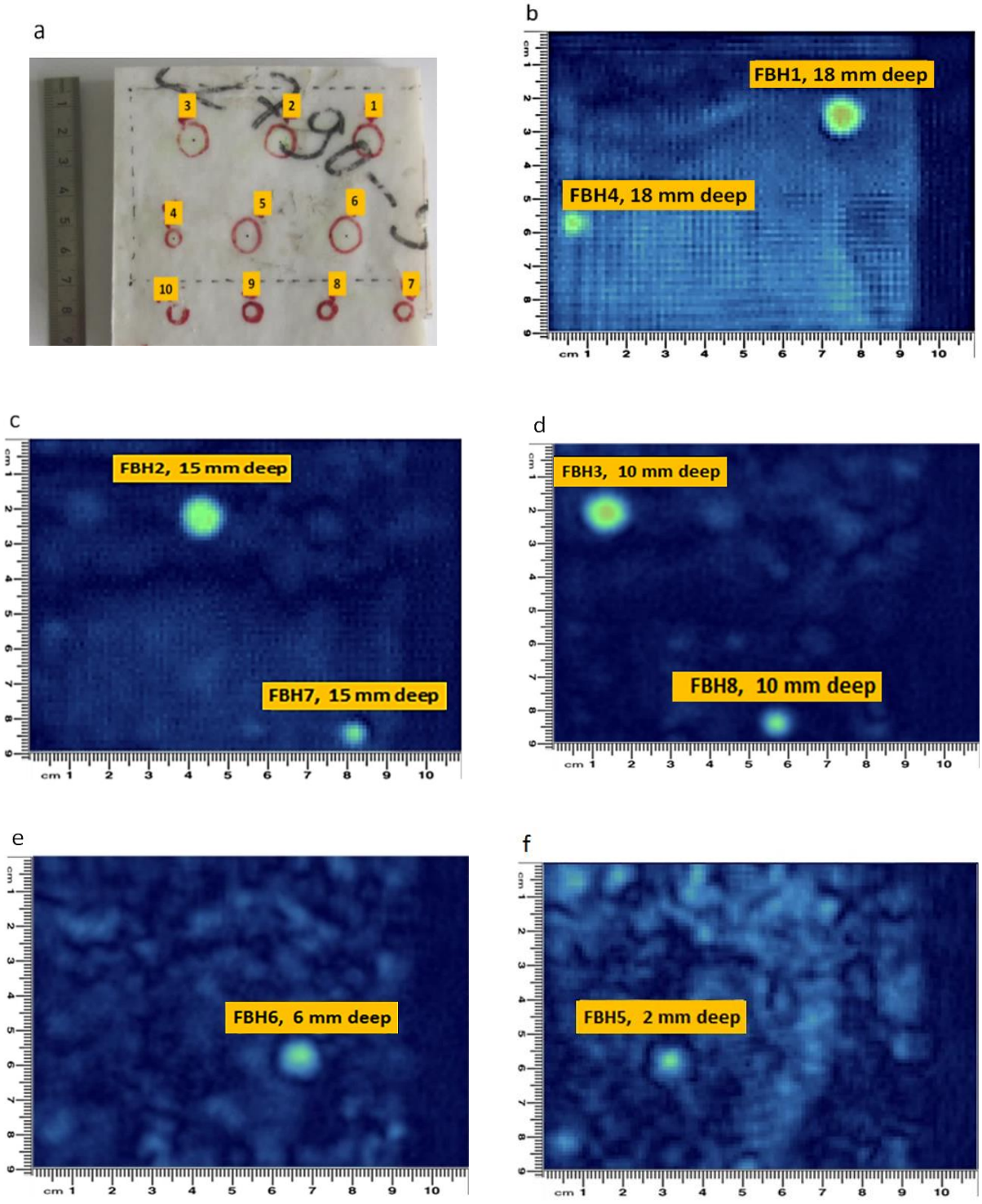

Fig. 61: Surface image perpendicular to the beam axis, represents the C-scan, a) sample surface, b) FBHs with 18 mm depth, c) FBHs with 15 mm depth, d) FBHs with 10 mm depth, e) FBH with 6 mm depth with 10 mm diameter, f) FBHs with 2 mm depth with 10 mm diameter.

Cross sectional images parallel to the beam axis (B-scan) can distinguish the FBHs in 3 rows (Fig. 62a). The bottom horizontal strip in Fig. 62b, c and d is the reflection of the antenna. The second strip

represents the front-wall echo of the sample and the top strip is the back-wall echo of the sample. The noise of the back-side (see Fig. 61e, f) can be seen here also obviously in comparison to the front-side.

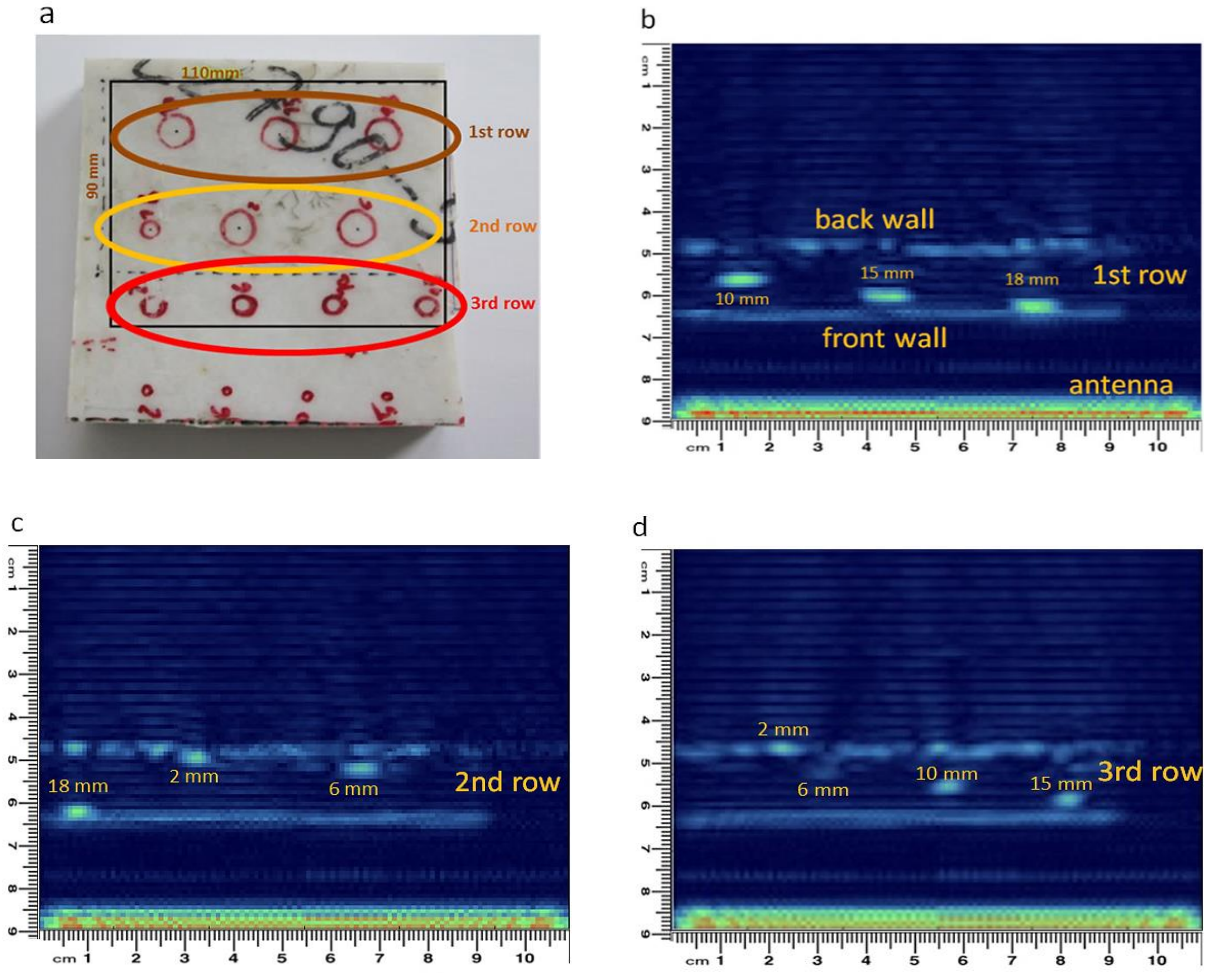

Fig. 62: Sectional image parallel to the beam axis, represents the B-scan, a) sample surface with the marked scan area, b) echoes of the front and back-wall including the first row of FBHs, c) echoes of front and back-wall including the second row, d) echoes of front and back-wall including the third row.

Between the front-wall and the back-wall, the FBHs can be detected. The first row consists of the 10 mm diameter FBHs with 18, 15, 10 mm depths (Fig. 62b). The second row (Fig. 62c) shows that the diameter size of the FBH with 2 mm depth is not easy to distinguish. The same problem can be seen in Fig. 61f. The third row (Fig. 62d) shows the 5 mm diameter FBH with different depths. The 15 and 10 mm depths are detectable in diameter and depth. It is strange to find out that the FBH with 2 mm depth is more distinguishable than the 6 mm one. This can be because the FBH 6 has not been drilled exactly flat and the microwaves are not reflected to the antenna, but in different directions. However, the diameter of FBHs 6 and 2 mm depth is not possible to be measured.

5.4.3 Curing

Because of the low velocity of microwave measurement (25 GHz bandwidth), not an area scan but a diagonal line measurement in reflection mode from the partial cured part to the complete cured part has been done here (Fig. 63a). 11 points along the line measurement in Fig. 63b show the increase of the magnitude while moving towards the cured part. It is seen that the microwave testing is able to distinguish the insufficient curing process in the sample. This test has been done two times, and the results were the same.

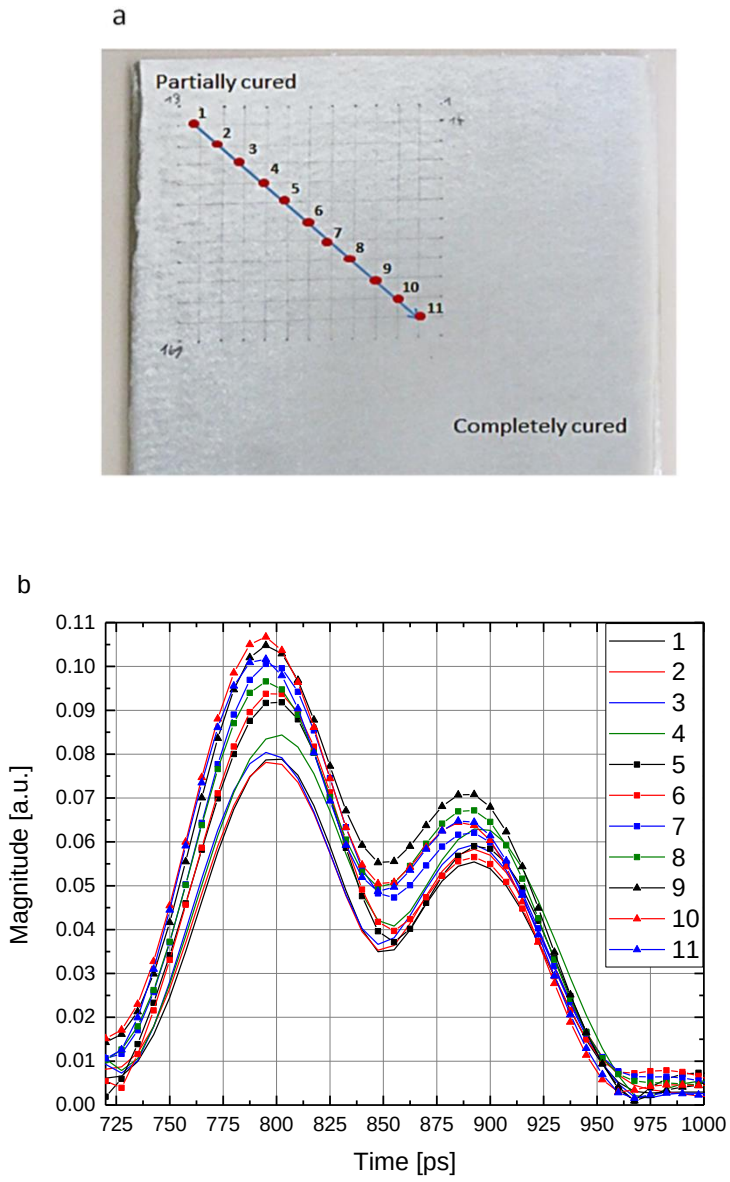

Fig. 63: a) Schematic of the microwave line scan testing on partially cured sample, b) line microwave reflection measurement in time domain mode reflection mode of partially cured sample. The magnitude has arbitrary units.

5.5 **Results of terahertz**

In order to discuss and realize the results of THz system, it should be first explained, how the signals are processed.

THz signal processing

The received THz pulse from the emitter saved as a time domain signal is shown in Fig. 64. A simple Fast Fourier Transform (FFT) analysis is therefore enough to obtain the spectrum of the measured time pulse. Fig. 64 represents also the calculation of some signal processing parameters of the time signal, which has been used in this thesis. In these measurements, the values of the amplitude are displayed in arbitrary units.

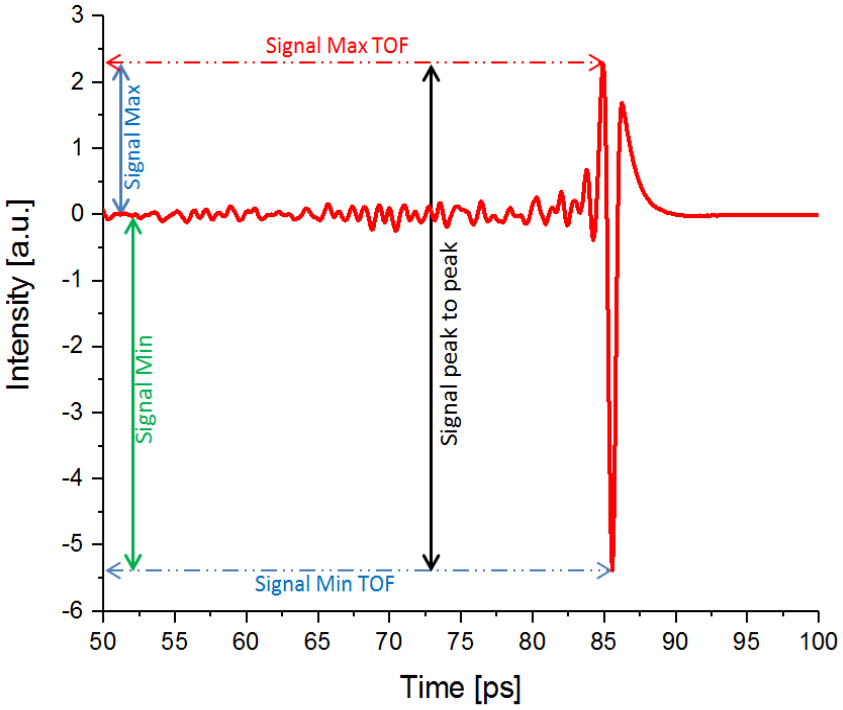

Fig. 64: Signal processing of the THz time signal in this thesis

The time signal analysis has been performed through the calculation of the envelope of the pulse (Fig. 65).

Eq. 40

$$E(t) = \sqrt{f(t)^2 + H(f(t))^2}$$

where

E(t) is the envelope of the time pulse [a.u.],

f(t) is the function of time pulse [ps], and

H(f(t)) is the Hilbert transform of the time pulse [a.u.].

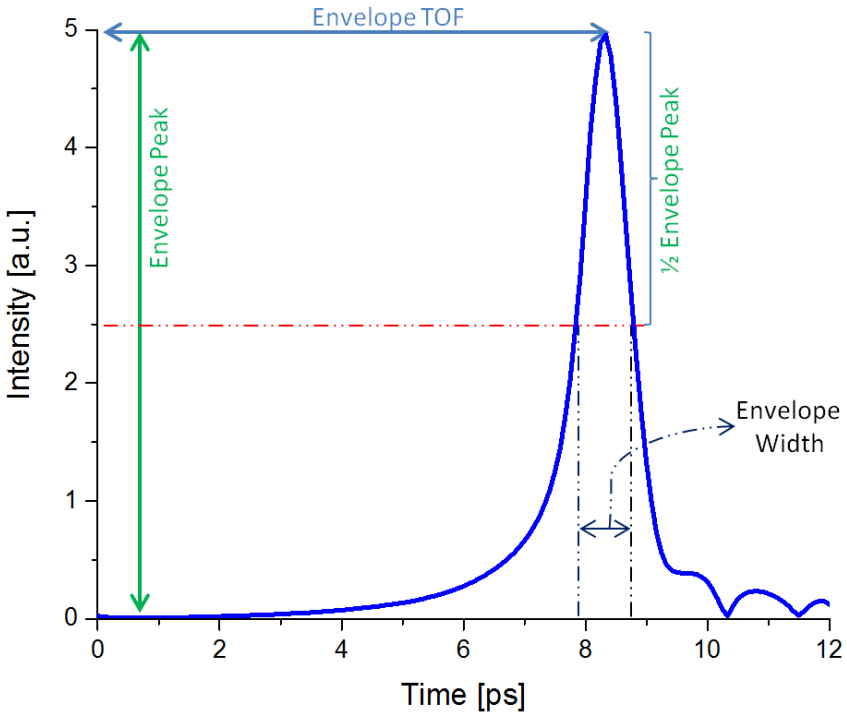

Fig. 65: Calculation of the envelope of the THz time signal in this thesis

Fig. 65 shows the envelope of the time signal and the calculation of TOF. In the diagram also the calculation of the envelope peak and the envelope width are shown.

5.5.1 Aging

In order to investigate the aged samples with the terahertz system at first three wet aged samples and one unaged sample were tested. After that the wet samples were dried and the test was repeated again including an unaged sample. Fig. 66 and Fig. 67 show the C-scans' evaluations in transmission mode for different parameters of the THz signal transmitted through the three wet aged samples (left) in comparison to one unaged sample (right). It is seen that all of the parameters in these figures can distinguish the wet aged samples from the unaged sample. Fig. 66 shows that the wet aged samples have more attenuation compared to the unaged sample. Fig. 67 shows that the time of flight of wet aged samples is higher than the unaged sample. It has been shown before that the terahertz time domain spectroscopy is an important device for moisture detection, moisture tomography and in depth analysis of THz approaches for moisture related aging characterization in polymers [Szielasko 2017].

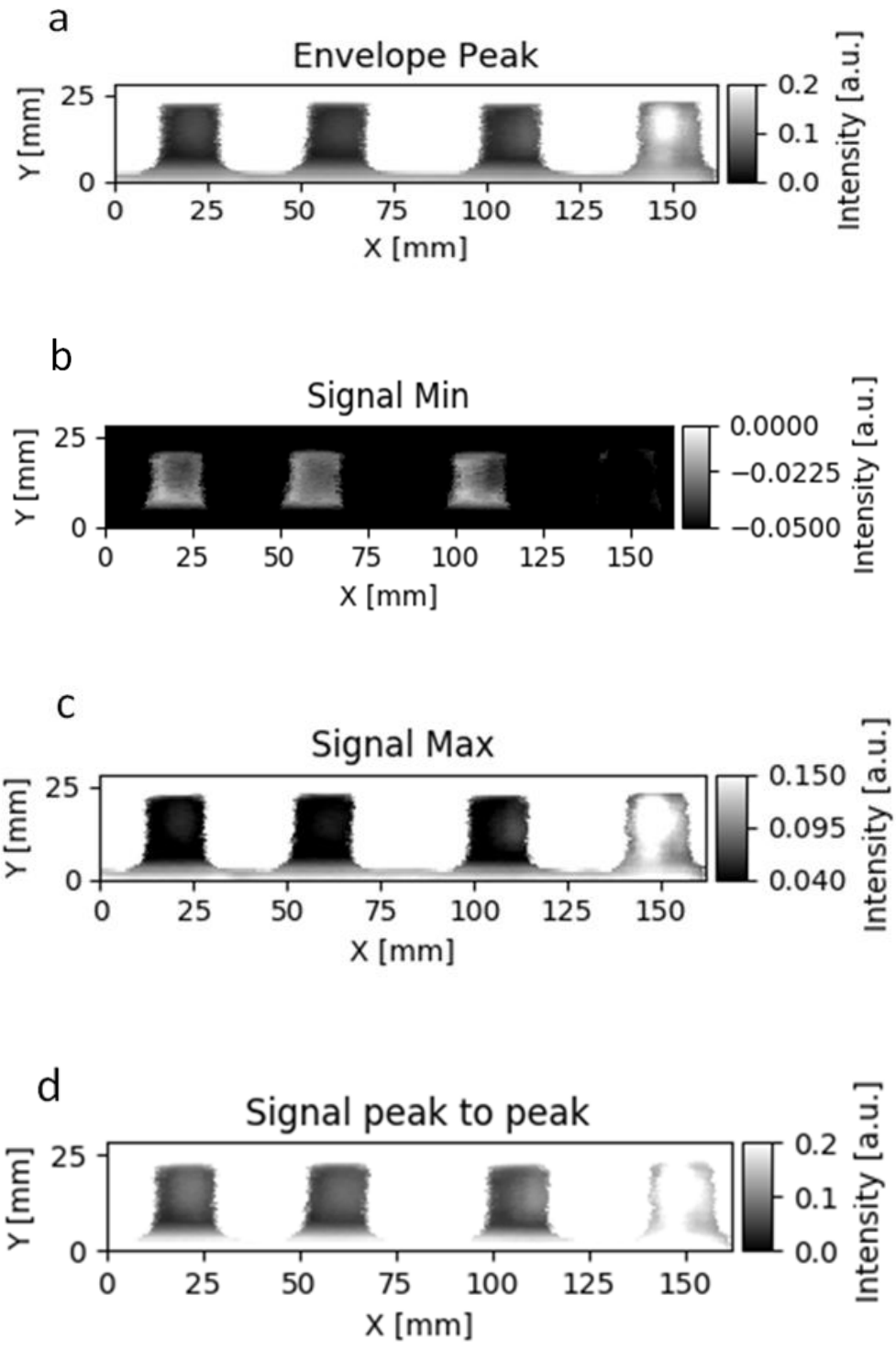

Fig. 66: THz scan surface of three wet aged (left) and one unaged (right) samples. Analysis with different parameters in intensity

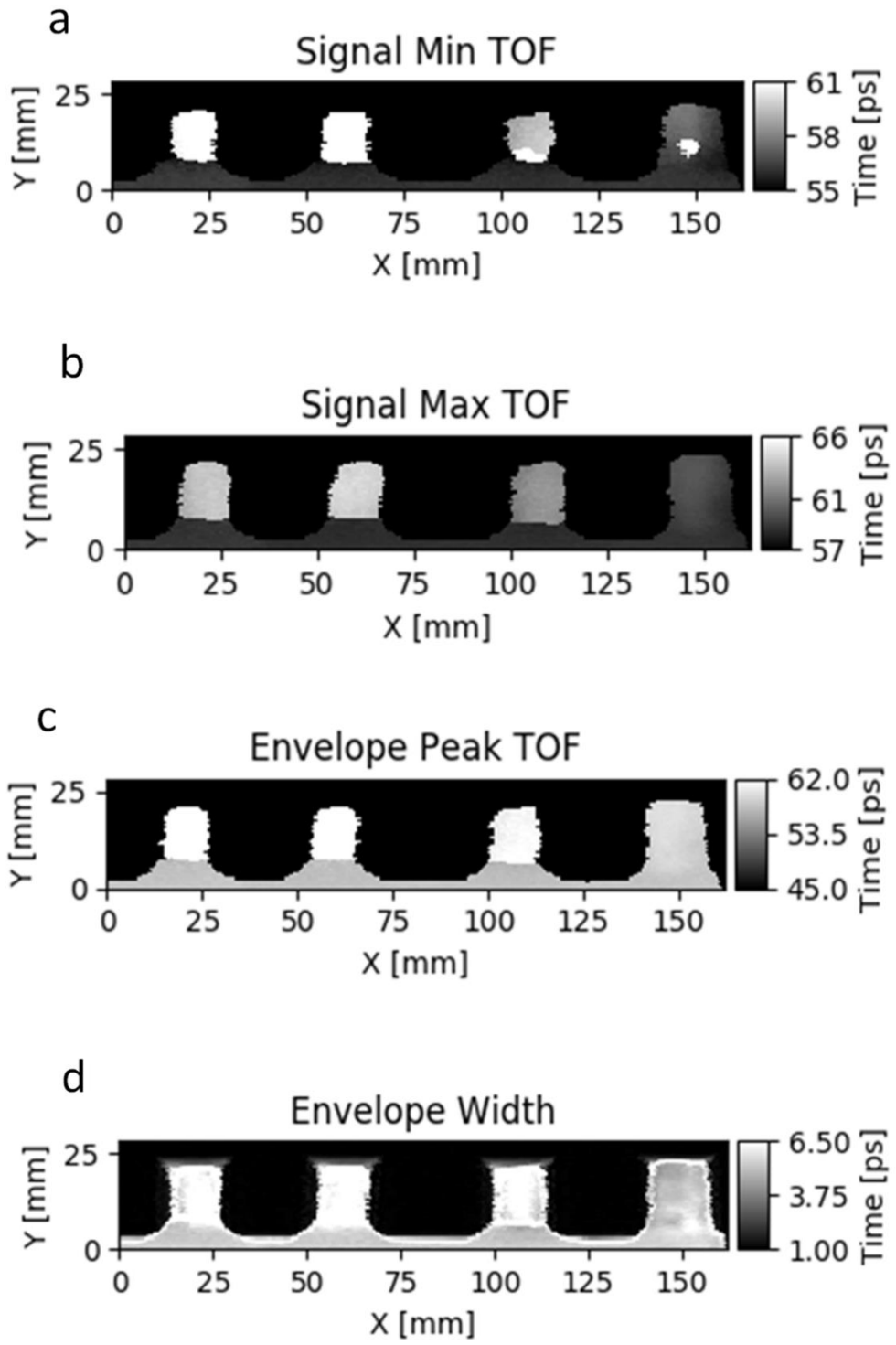

Fig. 67: THz scan surface of three wet aged (left) and one unaged (right) samples. Analysis with different parameters in TOF

Fig. 68 and Fig. 69 show the C-scans' evaluation respectively in intensity and in TOF, for different parameters of the THz signal transmitted through three aged dry samples (left) and one unaged sample (right). It is seen that in Fig. 68 the intensities in different parameters cannot distinguish the aging process but in Fig. 69 except the TOF analysis shown in Fig. 69b, d the other parameters can distinguish the aging process on the CIPP samples. In Fig. 69a, c the signal minimum time of flight

and the envelope peak time of flight show that the aged samples have a time delay to the unaged sample.

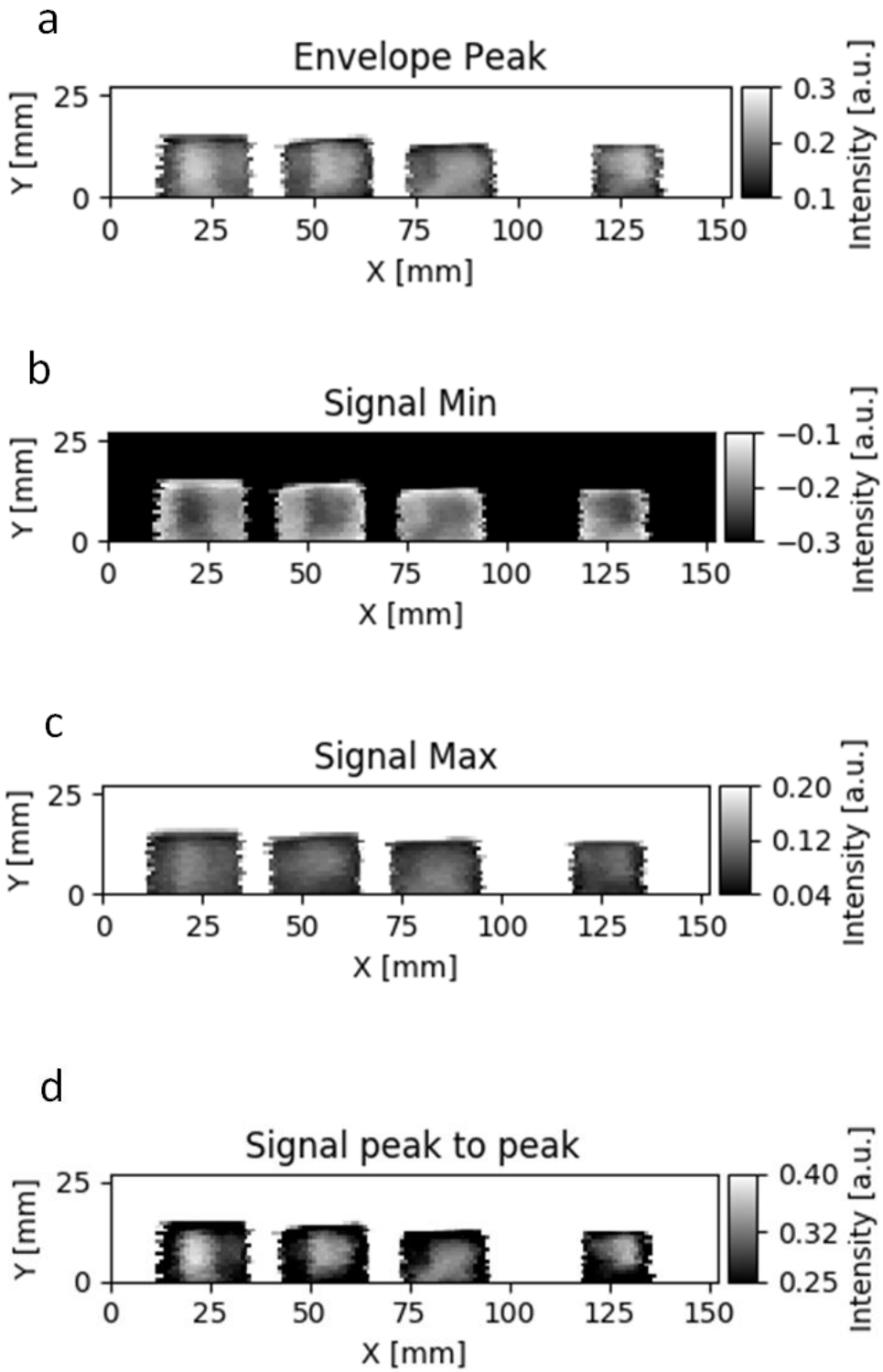

Fig. 68: THz scan surface of three dry aged (left) and one unaged (right) samples. Analysis with different parameters in intensity

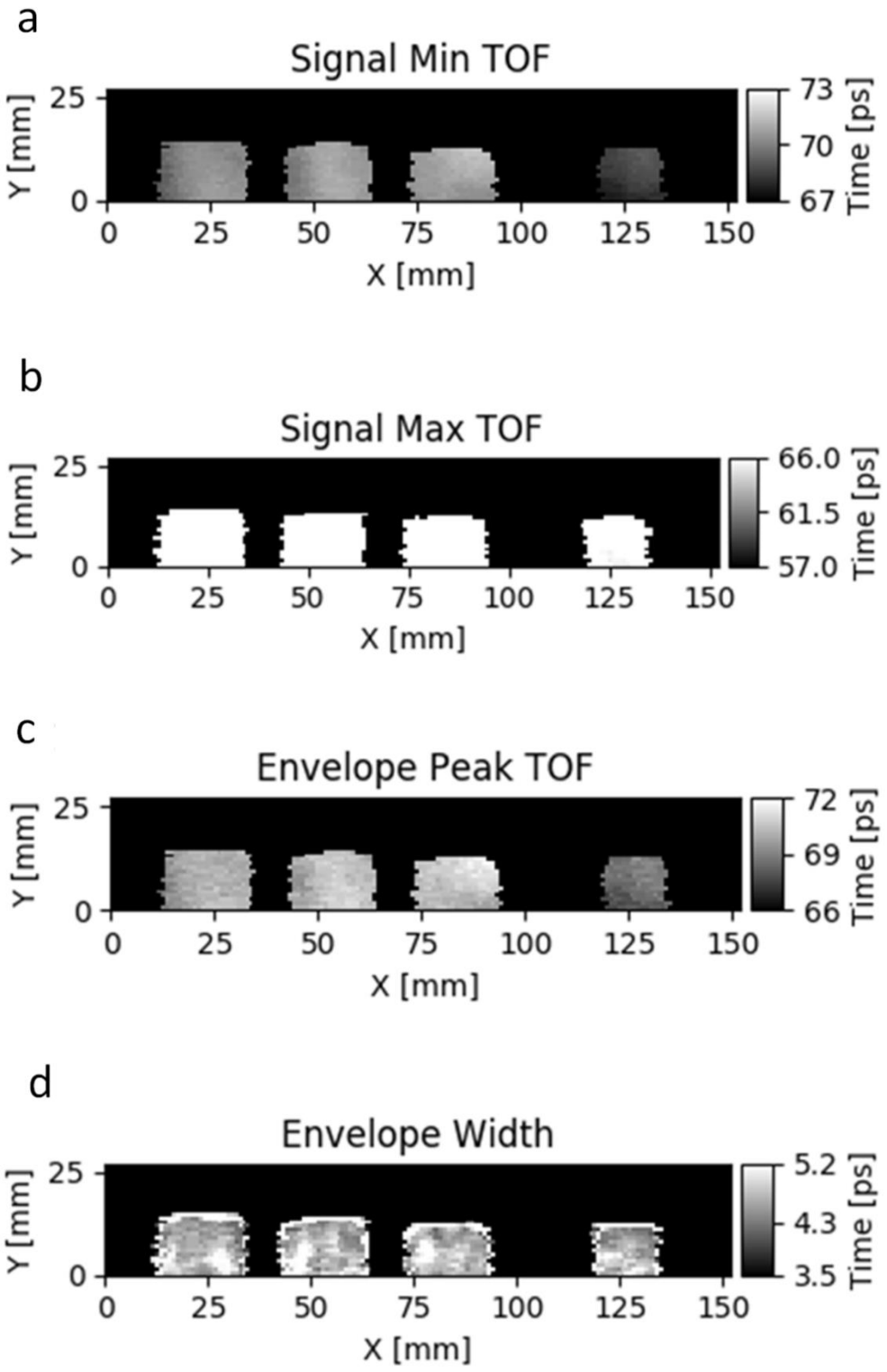

Fig. 69: THz scan surface of three dry aged (left) and one unaged (right) samples. Analysis with different parameters in TOF

5.5.2 Geometrical defects

The machined geometrical defects with different depths and diameters as shown in Fig. 70 have been inspected by means of the terahertz time domain spectroscopy method. The details of defects are available in Fig. 38 and Table 3 respectively.

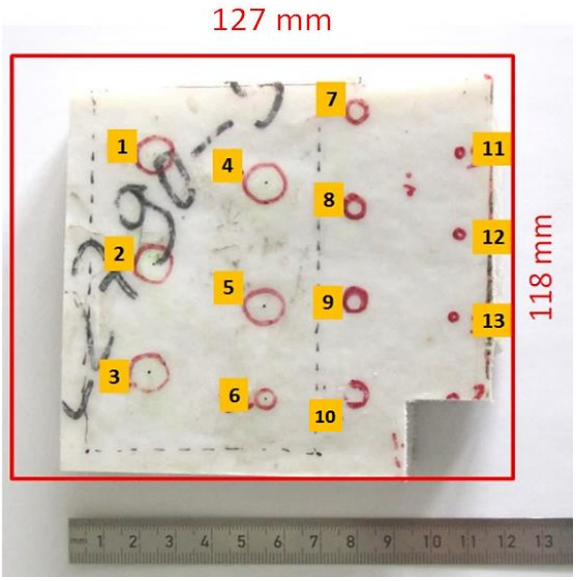

Fig. 70: Front side of the sample with the marked scan area

Fig. 71 shows the signal amplitudes in different parameters of the scanning surface. In Fig. 71a, c, d, f and g the three first columns of defects with 10 mm and 5 mm in diameters are visible with the exception of FBHs 9 and 10. It is observed that the air around the sample has always the highest amplitude and with respect to the thickness of the sample at the different FBHs, the deepest FBHs have the higher amplitude when compared to the FBHs with lower depth or the area without FBHs.

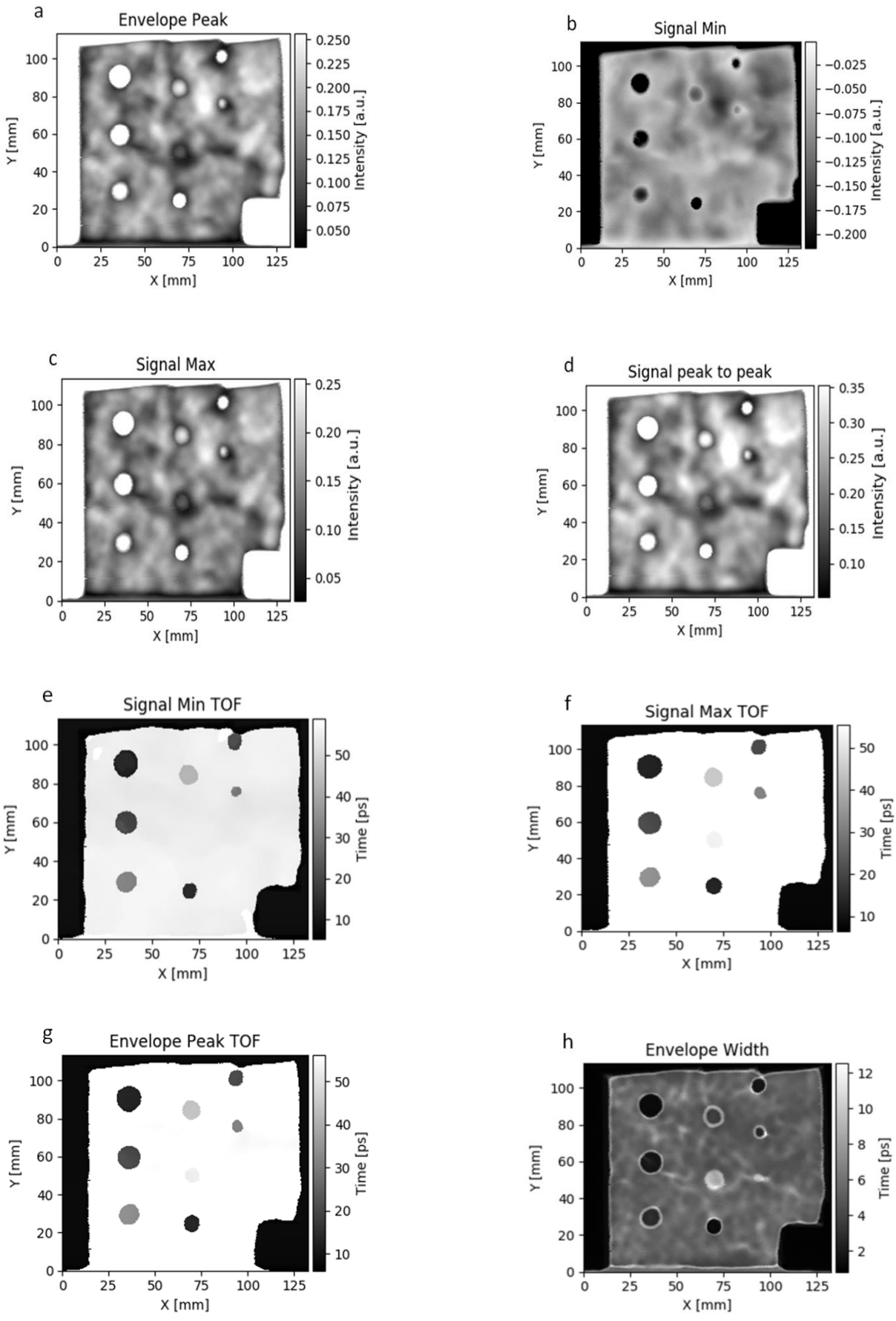

Fig. 71: THz scan surface of 127 mm×118 mm of FBH machined sample. Analysis with different parameters

In Fig. 71b and e one can see the same results but the FBH number 5 is not observable. Fig. 71h represents the best results, in which the FBHs 1 to 8 are observable and the existences of the FBHs 9 and 10 is detectable. The amplitude is considered in an arbitrary unit [a.u.].

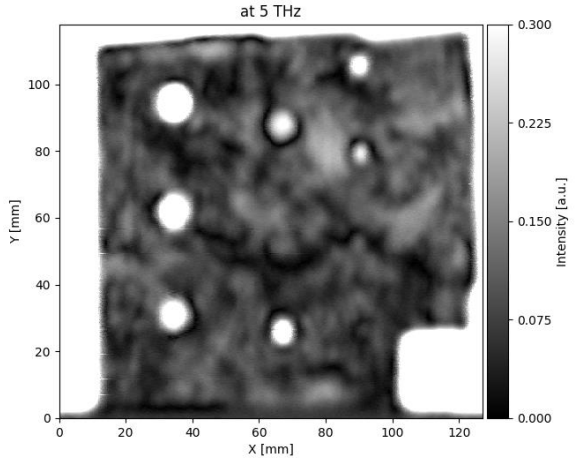

Fig. 72: THz scan surface of 127 mm×118 mm of FBH machined sample. Analysis of the spectrum signal at frequency 5 THz

Fig. 72 shows the spectrum analysis at 5 THz, in which the first 8 FBHs except number 5 are easy to evaluate in existence and diameter. However, this evaluation is not able to characterize the depth of the FBHs.

Fig. 73 refers to the time signal analysis of the bore machined sample showing the cross section of the sample surface perpendicular to the signal propagation in different time intervals. As it can be seen from Fig. 73 the FBHs with the same depth appear together and the appearance of the FBHs begins with the deepest FBHs 18 mm. Gradually the FBHs disappear and the next two FBHs will come until to 2 mm in depth, which appear with some noise because of the roughness of the sample's back-side. In any case the FBHs with the 3 mm diameters do not appear even in the time signal. It means the lateral resolution of the THz inspection is not enough to characterize two points with 3 mm or less distance.

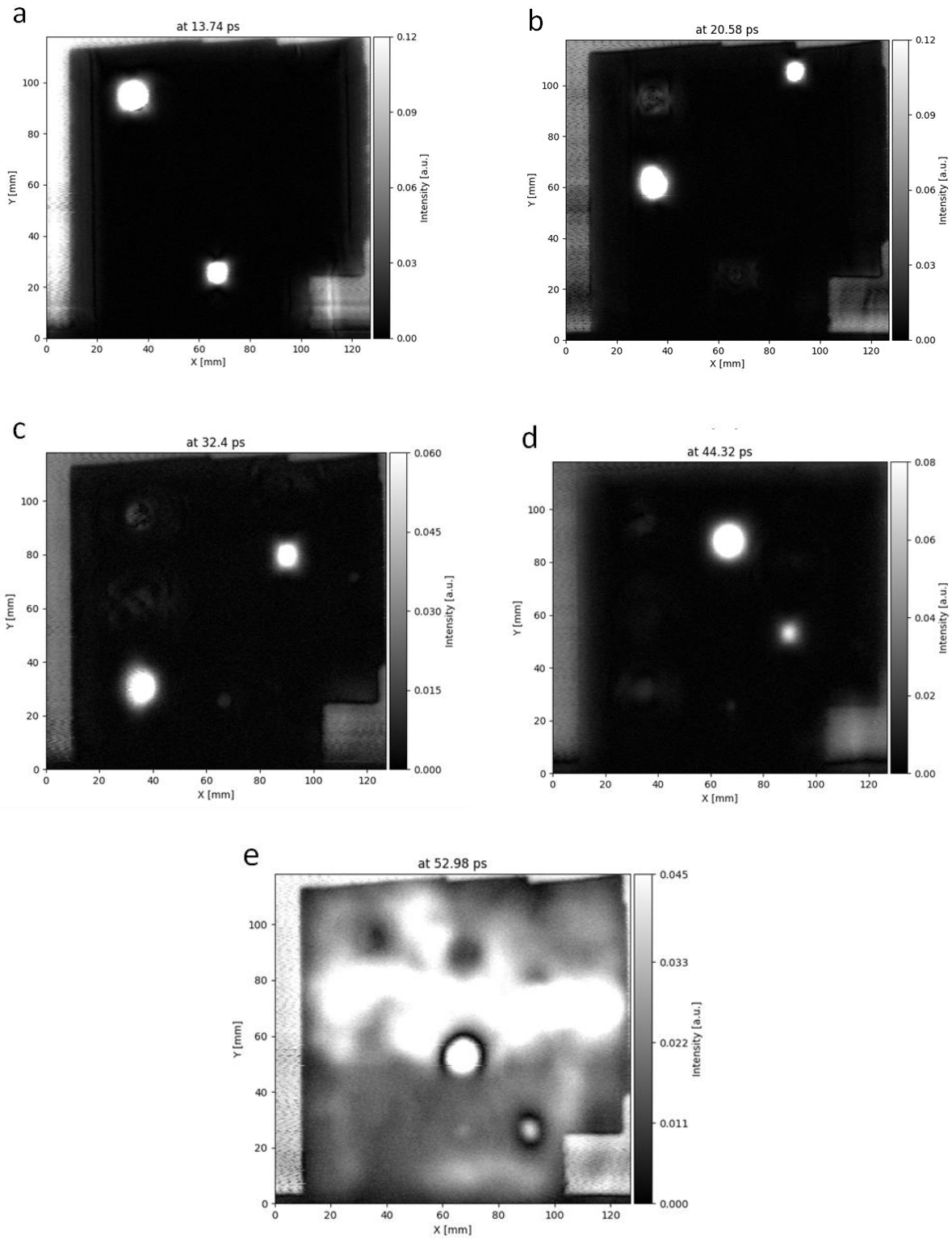

Fig. 73: THz scan surface of 127 mm×118 mm of FBH machined sample. Cross sections of envelope analysis, perpendicular to the signal propagation, in time domain at different time intervals, a) 18 mm FBHs at 13.74 ps, b) 15 mm FBHs at 20.58 ps, c) 10 mm FBHs at 32.4 ps, d) 6 mm FBHs at 44.32 ps, e) 2 mm FBHs at 52.98 ps

5.5.3 Curing

As explained in 5.4.3 the crosslinking and curing process in thermosetting polymers cause the variation of dielectric properties which is detectable with microwaves and also THz inspection. Due to the dilution of the resin with styrene in UP changes the dielectric parameter. This change as seen in 5.4.3 is visible through microwaves tests in time domain. In this section a surface of 140 mm×220 mm marked in Fig. 74, has been scanned and the signals measured can be shown in time and frequency domain.

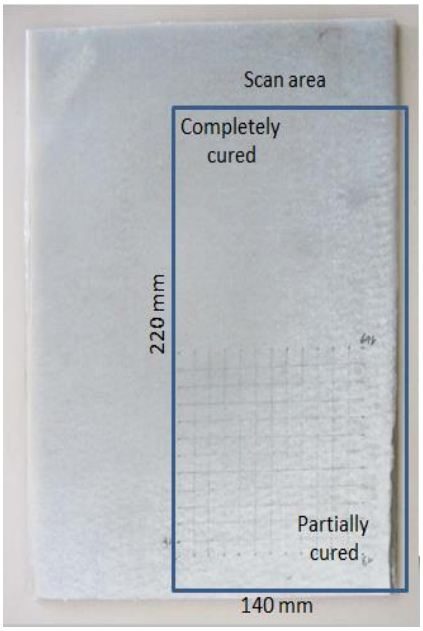

Fig. 74: THz transmission method, testing on partially cured sample

In this section different parameter analyses have been applied on the signal amplitude to figure out, which analysis can differentiate the dielectric parameter between partially and completely cured areas. Fig. 75 and Fig. 76 show these parameters respectively in intensity and in TOF. In between, only the time of flight parameters in Fig. 76a, b and c can present these different parts in terms of a difference in time except the envelope width.

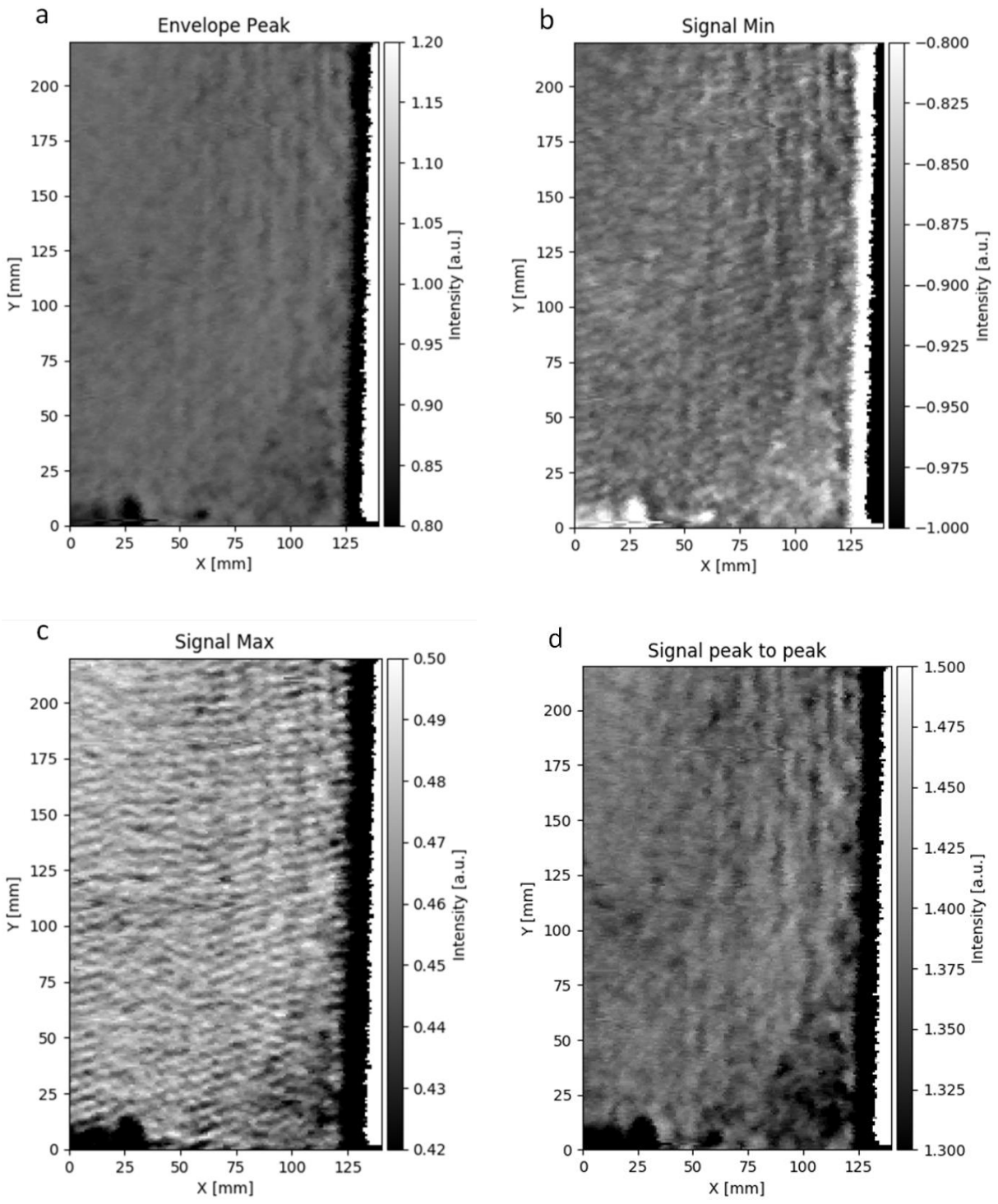

Fig. 75: THz scan surface of 140 mm×220 mm of partially cured sample. Analysis with different parameters in intensity

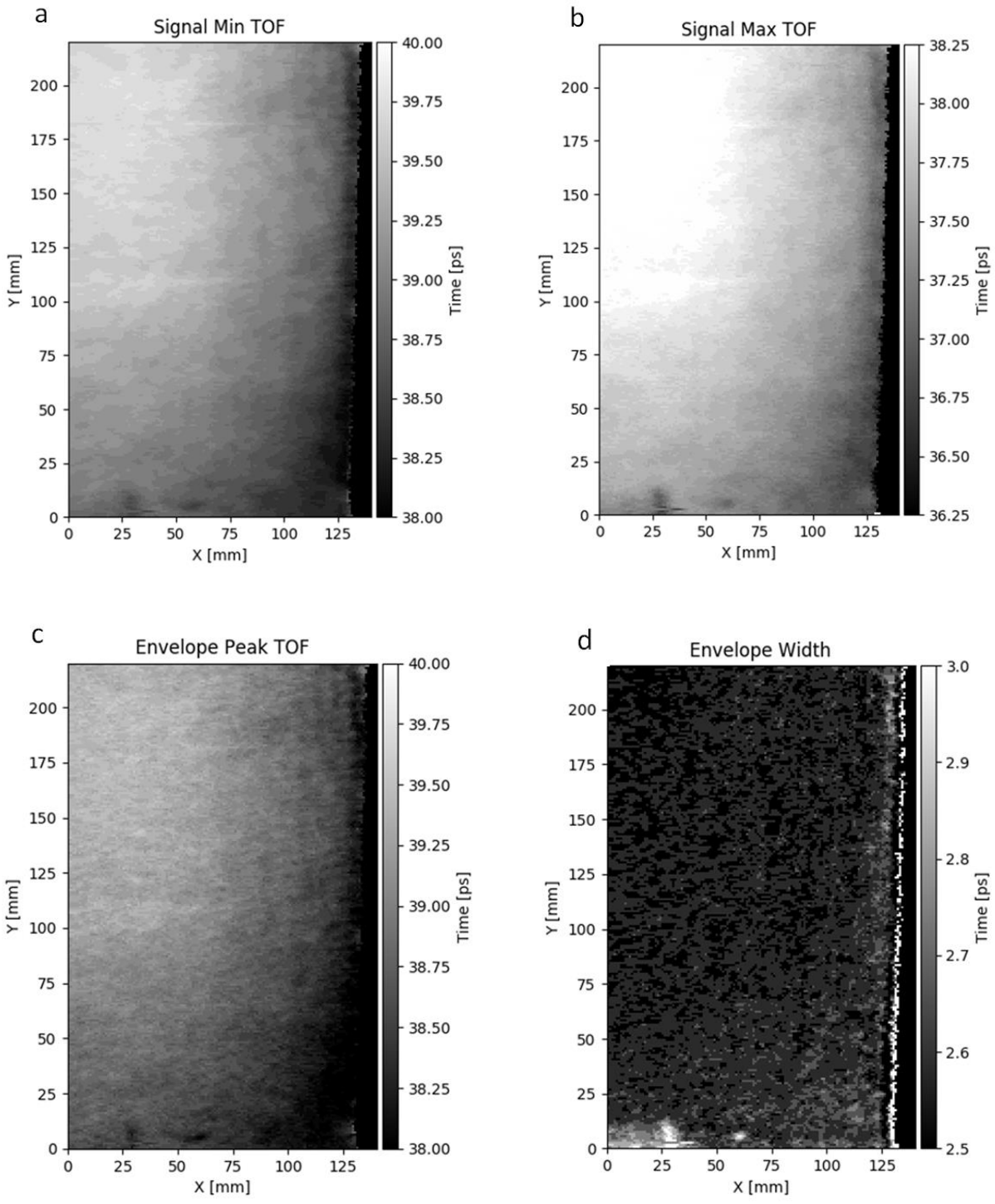

Fig. 76: THz scan surface of 140 mm×220 mm of partially cured sample. Analysis with different parameters in TOF

It is seen that the partially cured part has a shorter TOF than the completely cured one. This means that the real part of permittivity of the sample increases with the curing process but as no difference in two-dimensional analysis is seen in intensity, the curing process may have no effect on the imaginary part or the effect is too small to be detected with this type of analysis.

The interesting point is that one can also see the trend of curing with different times of flight. When the electromagnetic waves need more time to pass through a medium, this means that the medium has more real part permittivity (ε′). More specifically, the material has more ability to resist an electric field forming in the material.

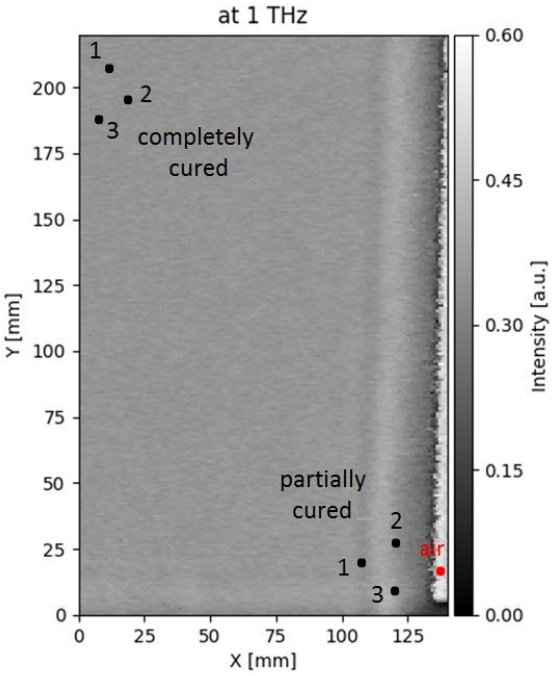

Fig. 77: THz scan surface of 140 mm×220 mm of partially cured sample. Analysis of the spectrum signal at 1 THz

The two-dimensional analysis of the spectrum in Fig. 77 shows no differences between the signals for the partially cured and the completely cured part.

5.6 **Results of ultrasound**

5.6.1 Aging

For the ultrasound testing, the aging samples were investigated in two conditions:

1. Comparison of three wet aged samples with one unaged sample and

2. Comparison of three dry aged samples with one unaged sample

The aim of this measurement is to determine if the effect of the hydrothermal aging on the CIPP samples is detectable with the ultrasound technique. Therefore, the aged samples were tested with an unaged sample for a better comparison. Fig. 78a shows the B-scan of the measurement immediately after aging, while the samples are still saturated with water. It is seen that in the wet aged samples the back-wall echo is observable. Fig. 78b shows the B-scan of dry samples, in which no echo of the back-wall is distinguishable. It is observed that the plasticization of water in CIPP samples facilitates the

detection of the back-wall echo. In other words it is possible to measure the thickness of the CIPP samples.

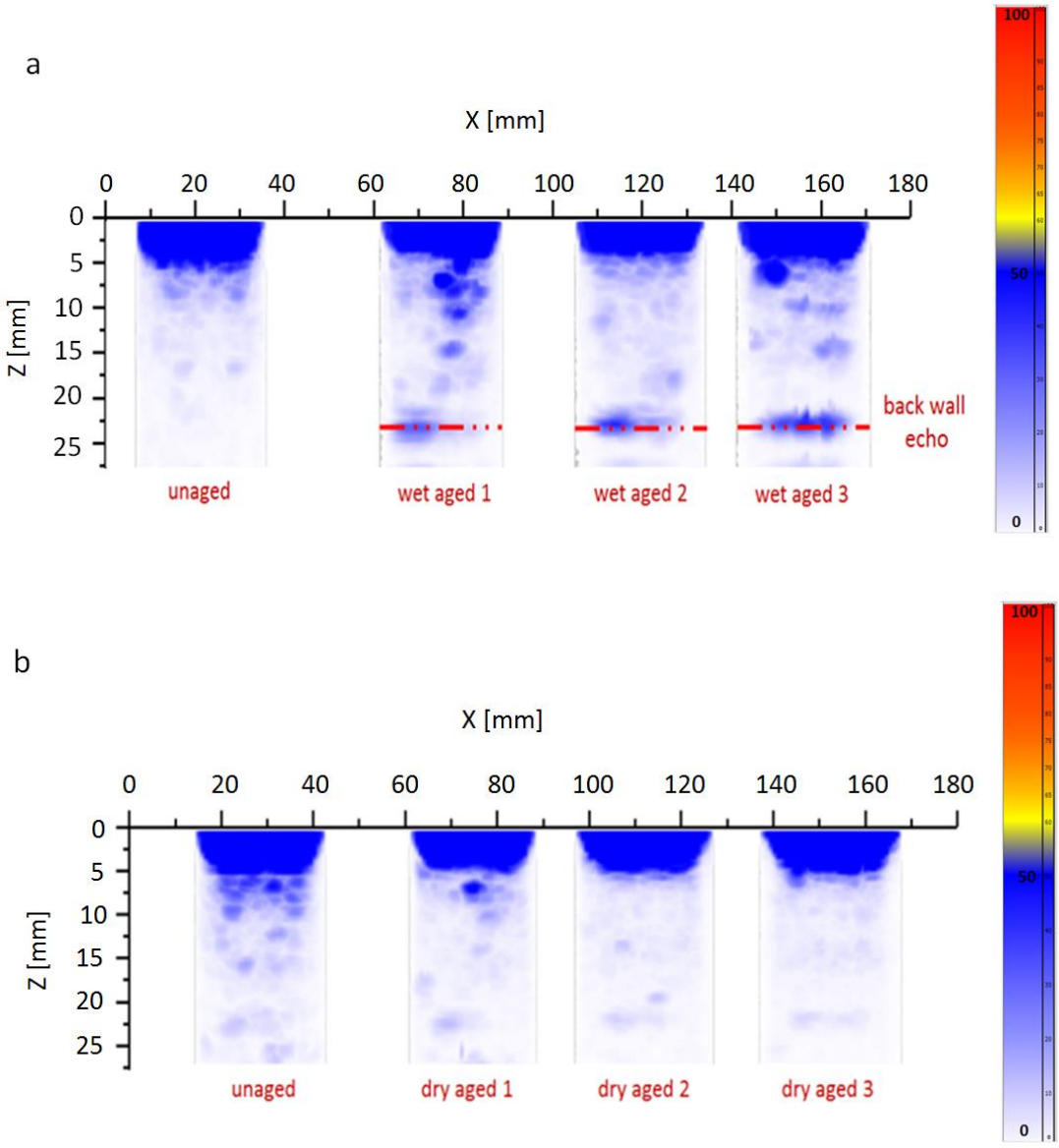

Fig. 78: Ultrasound B-scan measurement of aged and unaged samples with frequency 2.25 MHz, a) three aged wet samples and one unaged sample, b) three aged dry samples and one unaged sample

5.6.2 Geometrical defects

Fig. 79b shows the ultrasound C-scan and presents the amplitudes of the CIPP surface. The FBHs are detectable when compared to the results shown in Fig. 79a. The first bottom row with the FBHs of 10 mm in diameter and 18 to 10 mm in depth are distinguishable. In the second and third row the same depth FBHs with 5 mm in diameter are observed but among FBHs with 6 and 2 mm in depth, only the existence of the 6 mm in depth FBH with a large diameter in the second row is visible. The important point in this chapter is in contrary to the results of the microwave and the THz testing, where one of the FBH with 3 mm in diameter and 15 mm in depth is shown in the top row and can be recognized.

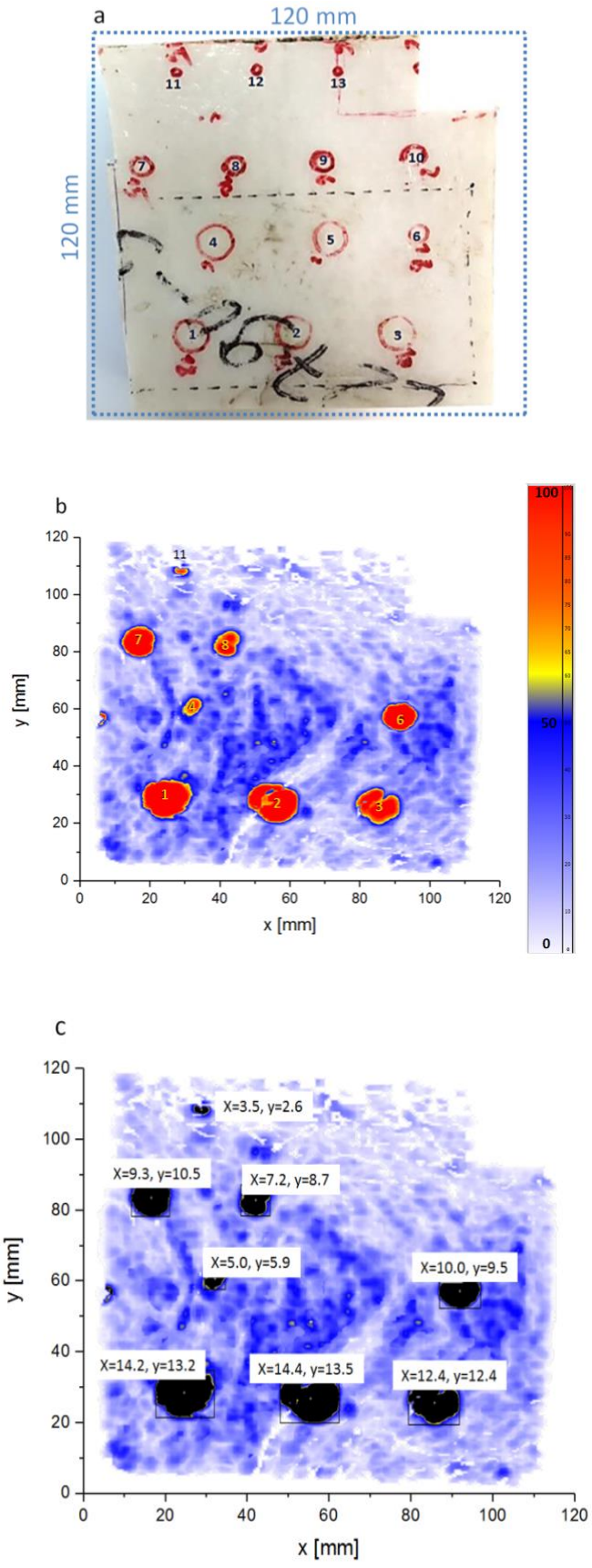

Fig. 79: a) Surface of the CIPP tested sample, scan area marked within the dotted area, b, c) ultrasound C-images, amplitude of the input echo on the CIPP sample with geometrical defects determined at 2.25 MHz frequency.

In order to inspect how this technique has been successful in detecting the size of the FBHs, as shown in Fig. 79c, the size of the FBHs has been measured. It is seen that the FBHs appear in Fig. 79b and c larger than the real size with the exception of FBH number 4. FBHs 3 and 11 have the best measured size related to the real size (see Table 4).

Table 4: Results of the C-Scan of the ultrasound measurement on sample with FBHs

FBH	Existence visible?	Real size	C-scan size
1	yes	10 mm×10 mm	14 mm×13 mm
2	yes	10 mm×10 mm	14 mm×13 mm
3	yes	10 mm×10 mm	12 mm×12 mm
4	yes	10 mm×10 mm	5 mm×6 mm
5	no	10 mm×10 mm	-
6	yes	5 mm×5 mm	10 mm×10 mm
7	yes	5 mm×5 mm	9 mm×10 mm
8	yes	5 mm×5 mm	7 mm×9 mm
9	no	5 mm×5 mm	-
10	no	5 mm×5 mm	-
11	yes	3 mm×3 mm	4 mm×3 mm
12	no	3 mm×3 mm	-
13	no	3 mm×3 mm	-

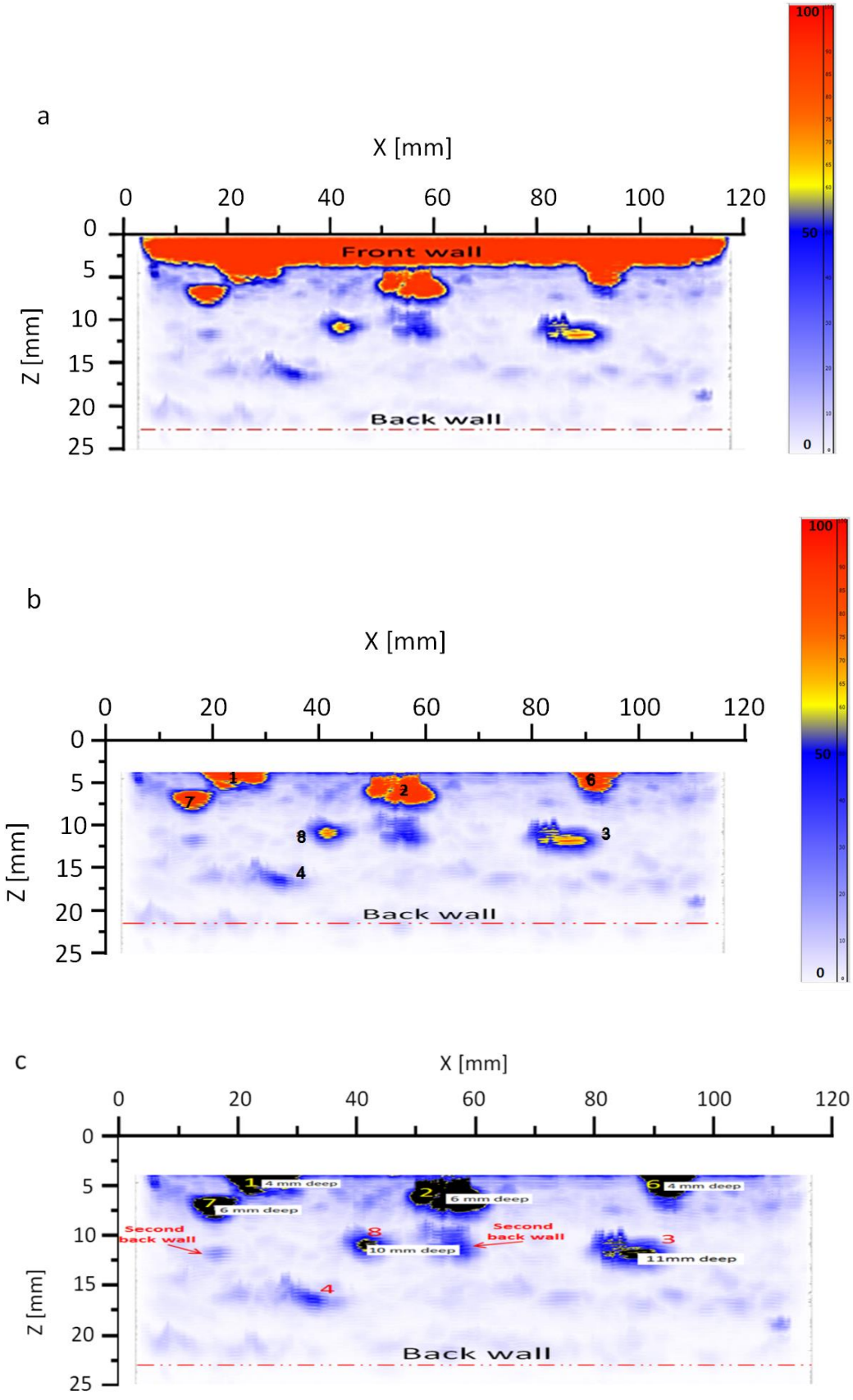

Fig. 80: Ultrasound B-scan, amplitude of the input echo of the CIPP sample with geometrical defects inspected with 2.25 MHz frequency, a) with front-wall echo, b) without front-wall echo, c) front-wall echo with depth of the FBHs

Fig. 80a shows the B-scan of the CIPP sample with FBHs. It is seen that the front-wall echo is so strong that it does not allow the echoes of the FBHs to be detected. In Fig. 80b the front-wall echo is cut for better investigation of the FBHs. B-scan evaluation helps to investigate the depth of the FBHs, which is not possible in a C-scan analysis. Fig. 80 shows that the back-wall is difficult to distinguish.

5.6.3 Curing

Fig. 81 shows the results of measured speed of sound at the different 11 points shown in Fig. 82a.

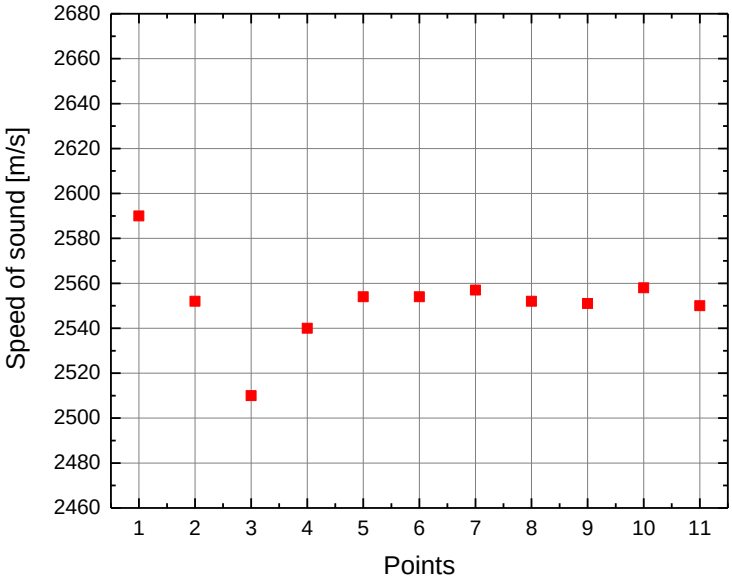

Fig. 81: Speed of sounds of the 11 different points of the partially cured sample

It is observed that the sound velocity decreases at first, followed by a slight increase in sound velocity and then stays constant after that.

Since there is only a slight difference between the sound velocities of partially and completely cured area of the sample, with assumption of a constant velocity, a two-dimensional scan of the partially cured sample is possible. In order to investigate the damping of the sample, an area of 190 mm×170 mm (shown in Fig. 82a) with a speed of sound of 2560 m/s has been scanned.

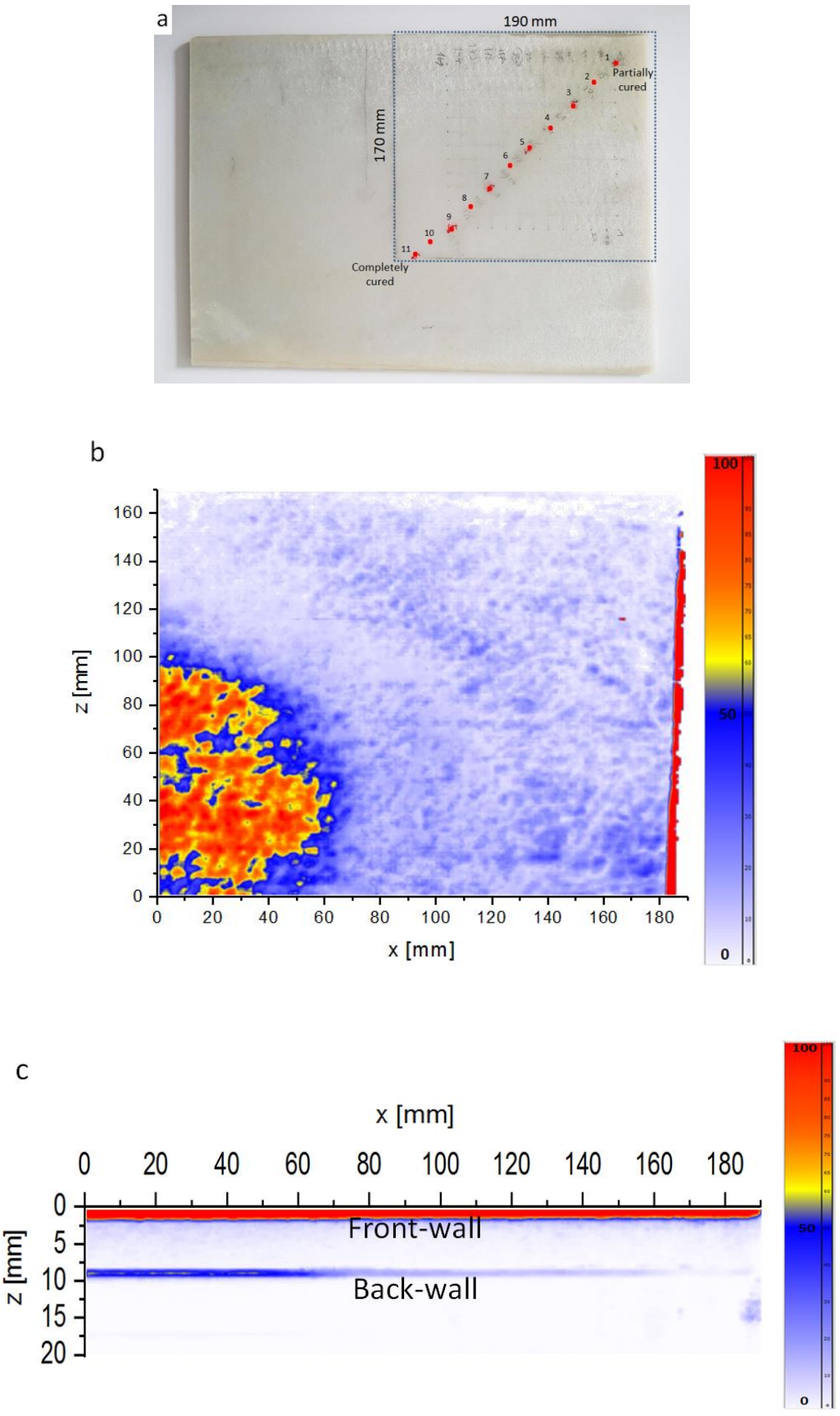

Fig. 82: a) The partially cured sample prepared for ultrasonic testing immersed in water with the scan area marked with a dotted line, b) ultrasound C-scan measurement within the dotted area with 5 MHz frequency, c)) ultrasound B-scan measurement

It is obvious from Fig. 82 b and c that the damping in the partially cured area is higher than the completely cured area. Fig. 82b shows a C-scan of the dotted line area in Fig. 82a. More intensity of the ultrasound echo on the cured area is visible. Fig. 82c is a B-scan, which shows that in the cured area the back-wall echo at 8.5 mm is distinguishable but towards to the partially cured area the detection of the back-wall echo becomes more difficult. It is verified that the curing process decreases the damping in the material.

6 Discussion

6.1 Analysis by weighing

Increasing the temperature may raise water uptake and accelerates the saturation but in this thesis applied temperature is 65 °C, because the CIPPs are not exposed to higher temperature. If hydrolysis occurs during aging, this leads to weight loss in the polymer. The hydrolysis in polymer happens in high temperatures according to T_g of polymers (usually at more than 90 °C). Hydrolysis of the UPRs is therefore out of question when considering conventional sewer lines. The only weight loss that exists under the latter operational conditions is due to dissolution of the coupling agent at the matrix-fiber interface, which has been measured after drying the wet aged samples in the oven.

The weight gain behavior of the randomly oriented PET carrier and UPR is a result of the water absorption in the matrix, fiber and their interface. The weight increase in percentage is calculated according to Eq. 41 and plotted versus square root of time (Fig. 83).

$$\%\ increase\ in\ weight\ (Ma) = \frac{wet\ weight\ (W_w) - conditioned\ weight(W_0)}{conditioned\ weight\ (W_0)} \times 100 \qquad \text{Eq. 41}$$

The total weight increase in the three samples has been between 0.0887 g to 0.1033 g. The samples were weighted again after drying to measure the weight loss (see Table 5).

Table 5: Calculation of increasing weight in three samples

Samples	Total increase in weight [g]	$\frac{(Ave.\times 100)}{\text{total increase in weight}}$	final M_a	Total decrease in weight [g]
Sample 1	0.0963	0.976116%	0.62157103%	0.0109
Sample 2	0.1033	0.816392%	0.64237299%	0.0113
Sample 3	0.0887	0.98835%	0.59113629%	0.0105

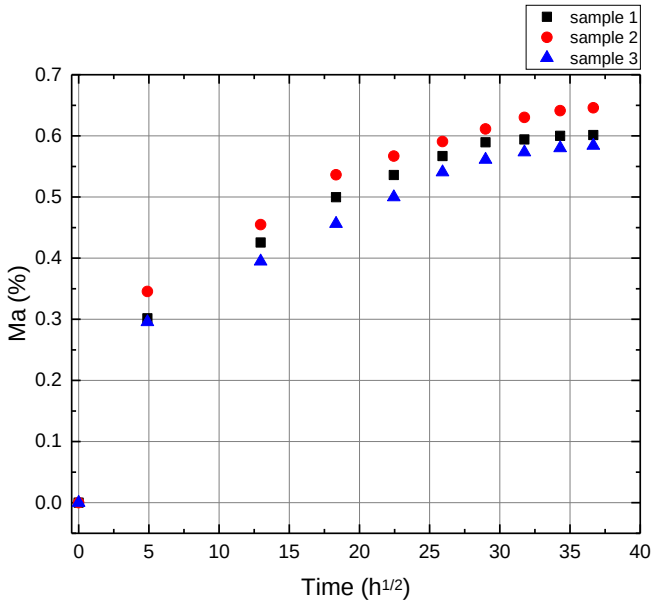

Fig. 83: Weight gain curves at 65 °C of three aging samples, M_a vs. time$^{1/2}$

When the mass uptake reaches an apparent equilibrium, the M_a ceases at 0.6% as can be seen in Fig. 83. Water absorption of polyester resin does not usually exceed this amount, according to the references [Apicella 1983].

The thickness of the samples was checked again after aging and a swelling of 0.3 mm up to 0.6 mm has been observed in wet condition and also after drying. This deviation in thickness has 1 to 2 ps time of flight of electromagnetic waves, then a delay in TOF of the microwave and the THz from 1 to 2 ps refers to this swelling. If the time delay is different from this amount, it represents the changing in the dielectric constant after aging.

6.2 **Analysis by optical microscopy**

During the exposure of CIPP to water, significant damage may occur in the form of micro-cracks. It has actually been observed that during the absorption stage such damage occurs mostly in the interior of the composite, while more intense micro-cracking is observed in the interface between the fibers and the matrix. It is therefore believed that the degradation effect of water absorption on the matrix of the composites is only secondary, compared to the damage at the fiber/matrix interface.

Hence two types of degradation after the hydrothermal aging are distinguished:

1. Matrix osmotic cracking (Fig. 53c)
2. Interfacial debonding (Fig. 53d)

Both degradations may be induced by differential swelling or by osmotic cracking and debonding at the fiber/matrix interface because of water accumulation. In fact the interfacial zone constitutes a suitable site for the osmosis processes because of stress concentration and the coupling agent leaching out. The binder-dissolving in water at the fiber/matrix interface may cause the debonding [Manavipour 2016].

To explain the degradation of the CIPP, the material and the curing process need to be investigated. Styrene is added to accelerate the curing process. It acts as a solvent [Sokoll 2009] which creates crosslinking units by reacting with the UPR. In the case that the polymers are incompletely polymerized, low heat stability, low resistance to hydrolysis and greater degree of swelling would appear. If aging in water promotes further reaction of the residual styrene monomer, it increases the T_g. Weight loss of polymers during water immersion is related to the leach-out of some of the components or portions of the macromolecular segments initially present in the resin [Apicella 1983].

The cured isophthalic polyester used in this research has $T_g = 120$ °C. The hydrolysis behavior is highly dependent on the temperature. The higher the temperature and the nearer it is to T_g, the higher the possibility of hydrolysis becomes. At 65 °C no hydrolysis is expected in UPRs. Hence, the only irreversible phenomenon that can occur as a result of hydrothermal aging is osmotic cracking and debonding [Gautier 1999]. On the other hand, since the UPR does not have high cationic charge (H-bonding), it is not a hydrophobic polymer and water plays a role of plasticizer, but not of a solvent. Therefore UPRs cannot be categorized as water-soluble but water-sensitive materials.

Microscopic observation of the samples before and after hydrothermal aging makes it possible to find out the reason behind the mechanical properties degradation of CIPPs. This degradation of elastic modulus and flexural stress in a three-point bending flexural test [Sterling 2016] may be dependent on the existence of micro-cracks in the matrix and debonding at the fibre/matrix interface, which appeared during the aging.

The main question regarding the existence of chemical aging in the material, being also a reason behind the mechanical degradation of CIPP, is answered in the next section. With the help of nanoindentation measurements, it is possible to characterize the mechanical behavior of small volumes of the matrix and fiber with spatial resolutions in the nanometer range. Therefore, the mechanical properties, assessed by means of nanoindentation tests (such as hardness and elastic modulus) are not affected by osmotic cracks and debonding, but rather by the structure of the matrix and fiber materials depending on their status of chemical aging.

6.3 **Analysis by nanoindentation**

6.3.1 Frequency sweep test

An increase in storage modulus with frequency in wet condition has been seen in Fig. 55a, b, which may result from the existence of waer in material, which leaves the sample during the time.

The storage modulus decreases after exposure of the composite material to an aging process in wet condition and it reverses back to the initial amount after drying. Fig. 55 shows also that the matrix has a higher storage modulus in comparison to fibers and in both the matrix and the fiber the water absorption causes reduction of the storage modulus. The water molecules interpose themselves between the UPR chains. This increases the distance between the chains and one can therefore say that the water absorption reduces the strength of the molecular bonds, which is the reason for the reduction of the storage modulus. Importantly the results show a complete recovery of the storage modulus after drying the wet samples in both cases in terms of the matrix and the fiber. It shows that at the aging temperature of 65 °C no hydrolysis happened and only mechanical aging consisting of cracks and debonding could cause mechanical deterioration of the samples.

On the contrary in Fig. 56a, b the aging increases the loss modulus in wet condition and after drying E″ reverses back to the primary amount. This behavior is indicative of the beginning of certain internal damping or energy dissipating effects by an increase in the amount of water. It illustrates that the higher amount of moisture enters the network of the CIPP samples and shifts the interchain distance up to the maximum. It shows that in this thesis, water as a plasticizer acts as a lubricant to reduce the rigidity and by doing so it increases the deformability of the polymer. Hence, water is not a substance in the polymer and the intermolecular bonds are not broken, because this phenomenon is irreversible. The diffusion of water molecules throughout the polymer chains causes plasticization, which results in a reduction of the T_g [Marais 2000]. The increase of the loss modulus after aging can be explained with the large interchain distance because of the water diffusion, which increases the internal damping being reflected in the loss modulus, which is an indication of damping. This indicates that an energy dissipation has occurred in the material with the absorbed water, that leads to increase the loss factor and it contributes to the damping of the material. This result supports the idea that both the reduction in storage modulus and increase in loss factor are due to the presence of absorbed water in the matrix and the fiber. It is also seen that the frequency decreases the loss modulus, which can be interpreted as a reduction of the intermolecular friction and at the 200 Hz the loss modulus of the unaged and aged dry samples goes to zero. The decrease of tanδ with frequency (Fig. 57a, b) means that the material acts more elastic and by applying a load, it has more potential to store the load rather than dissipating it.

It is known that a slow degradation process takes place when physical aging process due to water molecules is occurred in UPRs [Apicella 1981; Apicella 1982]. Moisture acts as both a plasticizer and

hydrolysis promoting the agent, decreasing the mechanical integrity of the ester matrix to a degree being dependent upon the temperature to which the material has been previously exposed. However, while plasticization is a reversible phenomenon, which disappears upon drying, chemical degradation is irreversible. As the mechanical properties after drying are reversed to the initial properties, it is confirmed that the only phenomenon during the aging process has been plasticization and it has been a physical aging process and not a chemical one.

Fig. 55, Fig. 56 and Fig. 57 indicate also the frequency response of the viscous behavior. As the frequency and time being inversely related, hence at low frequency viscous behavior is more pronounced. The increase in the storage and decrease in the loss modulus when related to frequency can be attributed also to the junctions between the polymer molecules, which are temporary entanglements within the various stages of the material's lifetime. In mechanical spectroscopy there are two relevant kinds of timescales: one is the timescale of measurement equal to 1/ ω and the other one is the lifetimes of the entanglements. At high frequency (ω), the timescale of measurement is shorter than at the lifetime of the entanglements, such that the entanglements behave as 'permanent'. It may increase the molecular chain rigidity and decrease the polymer chains' mobility and the friction among them. Therefore a rise of storage and reduction of loss modulus happens. At increasing time (decreasing ω), the timescale of measurement becomes of the order of the lifetimes of the entanglements. Hence, less junctions remain effective. Therefore the rigidity of the polymer decreases and the polymer chains' mobility and the friction increase, hence a reduction of E′ and increasing of E″ occur.

6.3.2 Creep test

As mentioned earlier the thermal drift can have a destructive influence on the validity of the measured displacement. Therefore all the values presented in this thesis are corrected using the method mentioned in chapter 4.1.4. Hence, the vertical axis has been named as ref. indentation displacement in Fig. 58 and ref. hardness in the Fig. 59.

A reduction of hardness has been observed in both matrix and fiber after hydrothermal aging in the wet condition related to the plasticization process as shown in Fig. 59a, b. Absorption of water molecules increases the reference indent displacements. The steepest ascent at the early times of measurements in the case of wet samples could be attributed to the effect of water, which lessens the intermolecular Van der Waals' force. However, the reduction is more in case of the matrix, which shows more water absorption in the matrix when compared to the fibers. Certain solvents can cause a material to soften, while they are exposed to the material. Others can chemically react with and harden the material. Both of these effects can cause failure. However, the results show that the hardness of dry saturated samples returned to that of the unconditioned state. It verifies the existence of the

plasticization phenomenon. Therefore, this hydrothermal aging is assumed to have not caused permanent damage like hydrolysis of the matrix and the fiber.

As mentioned earlier quantification of the results from creep measurements is made under the assumption that the samples show a linear viscoelastic behavior, which may not be correct specially in the case of pyramidal tips (like the tip used in this thesis) [Díez-Pascual 2015]. A generalized model of the viscoelastic–plastic behavior has been proposed by introducing an additional plastic element in the dashpot-spring model of viscoelasticity [Oyen 2003]. One simple way to compare the time-dependent deformation of polymers is to fit the variation of depth as a function of time during the hold period to the following equation [Beake 2006]:

$$h = h_0 + \zeta ln\left(1 + \frac{t}{\tau}\right) \qquad \text{Eq. 42}$$

where

h is the indent displacement [nm],

h_0 is the initial penetration at the beginning of the hold period [nm],

ζ is a characteristic of the asymptotic regime and proportional to the initial penetration [nm],

t is the creep time [s], and

τ is the characteristic time [s].

In other words, the characteristic of the creep time is equal to τ which is achieved in Table 6 after curve fitting (see Appendix).

Table 6: Characteristic of the creep time for three conditions

Condition	τ in matrix	τ in fiber
Unaged	4.18131	1.92639
Aged wet	9.37751	10.29215
Aged dry	5.3032	4.14909

For the case of a conventional relaxation test and for a linear inelastic deformation the variation of the strain versus time can be depicted as follows (Fig. 84):

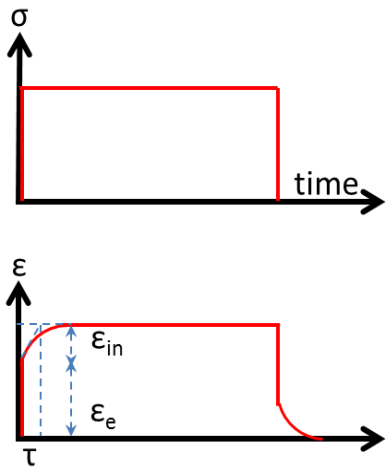

Fig. 84: Schematic presentation of the elastic and inelastic deformation of a linear viscous material.

The first sudden change of strain during the application of the constant stress is due to the pure elastic deformation, which follows with a time dependent inelastic deformation. If a tangent at the time zero is plotted, the constant τ can be calculated, which represents the time of the damping properties of a sample. The most frequently used equation for evaluation of the viscosity properties of polymers is as follows:

$$\tau = \frac{\eta}{E_{storage}} \qquad \text{Eq. 43}$$

where

η is the viscosity [Pa.s].

It can be observed from Table 6 that the τ values due to the water absorption both in the fiber and the matrix increases dramatically and then after drying it reduces again. It presents the influence of absorbed water on the damping properties of the polymers in both matrix and fiber. As explained before the viscosity property of the polymers is related to the loss modulus. The higher the viscosity the more energy dissipates in the polymer because of the loss modulus. Increasing τ in wet condition and reversing to the initial amount after drying shows that the viscosity of the CIPP samples increases in the aged wet condition. Therefore the damping and loss modulus increase. It has been shown before in 5.3.1 that the storage modulus decreases in the aged wet condition, while the loss modulus increases and after drying both theses constants reverse to their initial values. The reversing of the τ values shows that the hydrothermal aging on the CIPP samples in this thesis is due to the reversible plasticization.

Fig. 58 and Fig. 59 also show the dependency of the ref. indent displacement and ref. hardness vs. time of testing. It is seen for the fiber and the matrix in three conditions that increasing the time up to

200 seconds increases the ref. indent displacement. After 200 seconds the strain rate $\frac{\Delta(\text{indent displacement})}{\Delta t}$ reaches zero. As explained in 6.3.1 this time dependency can be related to the temporary junctions between polymer molecules with different lifetimes. As the timescale of measurement increases and it is longer than the lifetimes of the junctions, it may decrease the molecular chain rigidity, therefore increases the ref. indent displacement and decreases the ref. hardness.

6.4 **Analysis by microwaves**

6.4.1 Aging

Existence of water molecules in the material changes the permittivity (ε_r) and permeability (μ_r) properties. Since the variation of μ_r, as a result of the dielectric material being negligible in the frame of this study, it is assumed that $\mu_r = 1$.

The speed of microwaves in CIPP samples can be calculated by knowing the thickness (x) of the sample and the TOF.

$$c = \frac{x}{TOF} \quad \text{Eq. 44}$$

Assuming that the speed of the microwave propagation in vacuum is:

$c_0 = 2.998 \times 10^8 \text{m/s}$

then ε'_r can be determined from:

$$\varepsilon_r^{'} = \left(\frac{C_0 \Delta TOF}{2x}\right)^2 \quad \text{Eq. 45}$$

where

C_0 is the speed of light [m/s],

ΔTOF is the time of flight in the material from which the time of flight in air has been subtracted [s], and

x is the thickness of the material [m].

Eq. 45 is equal to Eq. 16. The factor 2 exists because of the reflection mode and the thickness needs to be inserted with factor 2 as well. A time domain measurement reveals the effects of all individual discontinuities due to permittivity changes, as a function of time or distance. Here, a discontinuity means a change of medium.

In the aged wet condition, the presence of free water in the CIPP sample increases the imaginary part of permittivity, which causes a high absorption of the signal resulting in no back-wall echo to be visible. The absorption of electromagnetic waves by water depends on the state of the water. Liquid water has a broad absorption spectrum in the microwave and THz regions, which can be explained in terms of changes in the hydrogen bond [Nyfors 1989].

The water molecule consists of one oxygen (O) and two hydrogen (H) atoms. These HOH nonlinear molecules have an angle of 104.5° and the OH distance is 0.95718×10^{-10} m. The chemical bonds are such that the electrons are closer to the oxygen atom than the hydrogen atoms, therefore the oxygen atom is more negatively charged than the hydrogen atoms. Because of the electronic and atomic polarizability the bent structure of the molecule produces a permanent dipole moment. Water molecules bounded by more than one H-bond are prevented from reorientational motions. Therefore, only the molecules, which are non- hydrogen or single hydrogen bonded can rotate around the direction of their permanent electric dipole moment into the direction of an external electric field, accordingly to contribute to the orientational polarization. As the water molecules are provided with a permanent electric dipole moment, their reorientational motions will produce electrical polarization noise. In principle this noise could be used to measure the dielectric properties of the moist systems [Kaatze 1989; Kupfer 2005; Lunkenheimer 2017].

The amplitude of the peak of the front-wall shows the difference of permittivity between air and sample. An increase in the front-wall echo amplitude is related to the increase of permittivity because of water absorption. It is observed that after drying the samples (condition “aged”), the front-wall and back-wall echo are almost the same when compared to the unaged samples. With access to the echo of the front-wall and the back-wall, the TOF can be calculated (Fig. 60). By knowing the permittivity of the CIPP, the speed of microwaves in the material can also be calculated (Eq. 45). It is then possible to measure the thickness of the sample. It means that the microwaves technique has the potential of a thickness measurement of the CIPP samples. The only point is that the CIPP should not be wet. Since one of the noticeable problems of a CIPP is its reduction in thickness, this method may help to detect the area of the CIPP where the thickness is unacceptable.

By knowing the thickness and the TOF, it is possible to calculate the ε_r' from Eq. 45. Fig. 60b shows that the front-walls of the unaged and aged samples appear at 831.70 ps and 833.06 ps respectively, and the back-wall echoes show up for the unaged condition at 1073.06 ps and for the aged condition at 1075.68 ps respectively. Since a swelling of 0.3 to 0.6 mm has been seen in the aged samples, which is equal to 1 to 2 ps and the ΔTOF here is 1.26 ps, it means that this delay is the effect of the variation of thickness. Therefore no change in the permittivity has been seen between the unaged and aged dry samples.

Since for the aged wet condition the back-wall echo is not detectable, a calculation of the TOF in this case is not possible. It is shown that the microwave technique can detect the different times of flight between unaged and aged conditions. It is also seen that this technique can differentiate between the intensities of wet and dry conditions.

The absorption of electromagnetic waves by water can be quantified by the imaginary part of permittivity (ε″), which reveals a strong peak at frequency of about 20 GHz (corresponding to a cooperative relaxation of long-range hydrogen-bond-mediated dipole-dipole interactions) and a gradual tailing off towards higher frequencies (Fig. 85). Although the peak of ε″ in Fig. 85 appears at 20 GHz but it is seen that ε″ in the frequency range above 5 to 100 GHz is still considerable.

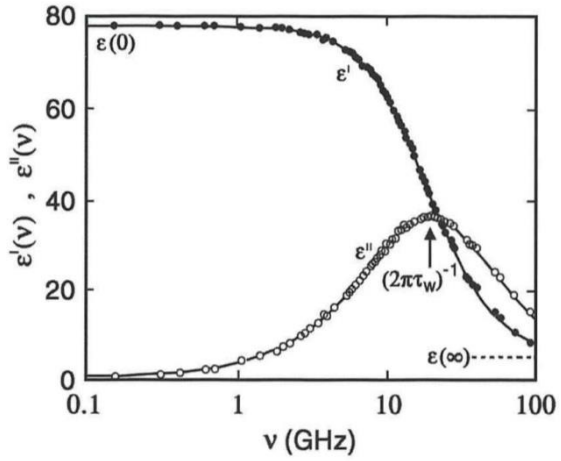

Fig. 85: Real part and imaginary part of the complex permittivity spectrum of water at 25 °C [Kupfer 2005].

6.4.2 Geometrical defects

In 5.4.1 it is seen that with the help of the B-scan evaluation, the back-wall of the CIPP sample is distinguishable. It enables the measurement of the thickness of the CIPPs. The main problem with regard to thickness measurement is the roughness of the back-wall, which complicates the determination of the exact position of the back-wall. It should also be considered that the sample in this test was dry but in reality, the CIPPs are either immersed in water or exposed to a humid atmosphere, which both have a high absorption of microwaves.

6.4.3 Curing

Microwave dielectric measurements are sensitive and are a valuable tool for studying the crosslinking and monitoring the curing process in thermosetting polymers [Bovtun 2001]. The change of microwave dielectric parameters reflects the curing and crosslinking process in materials. Not only the crosslinking process but also using the additives to accelerate the curing process can change the dielectric properties. For example, in unsaturated polyesters the dilution of the resin with styrene changes dielectric properties. Adding styrene to the resin causes a small increase of the polymers

relative dielectric constant as well as the loss factor, which is detectable at low frequency between 0.1 to 10 MHz [Hanemann 2010].

In case the traditional low frequency dielectric methods cannot detect the crosslinking process, the high accuracy of microwave methods enables even slight changes such as 1%, of the polymer dielectric parameters to be detected [Bovtun 2005].

In Fig. 63b the two peaks of each signal illustrate first the front and then the back-wall of the sample respectively. It is shown that when the material is better cured the magnitude is increased. As such the imaginary part is less in the cured condition. This means that a progression in crosslinking decreases the ε'' of the UPR.

It is known that the thermal crosslinking procedure affects the dielectric property in carbon-black epoxy composites. The dielectric constant depends on the contribution of the interfacial, dipole, electronic and atomic polarizations. The dielectric constant of the material also depends upon the polarizability, in other words, the greater the polarizability of the molecule, the higher is the dielectric constant [Trihotri 2015].

The time of flight (time difference between 2 peaks) among points 1 to 11 has a variation of 2 ps (from 92 ps to 94 ps). It shows that the variation of the dielectric constant is equal to 0.001. This small variation means that either the real part of the dielectric constant has not been changed or the microwave technique is not able to detect this variation. To answer this question, the sample has also been inspected through the THz system described in 5.5.3. The increase of the magnitude with progression of the curing process shows in Fig. 63b that the imaginary part of the dielectric constant decreases with the curing procedure and therefore the absorption of the electromagnetic waves in the sample decreases during the curing process. The absorption relates to the friction accompanying the orientation of the dipoles in the material. Since the polarization in the polyester as a polar polymer occurs because of the carbonyl oxygen atom driving the orientational polarization, this means that the orientation of the cured and saturated polymer molecules, in the external electrical field, accompany lower friction. It may explain why there is less collision between the large crosslinked molecules compared to the smaller molecules before crosslinking in the process of the orientation.

6.5 **Analysis by terahertz**

6.5.1 Aging

As it is seen in 5.5.1 the THz technique is able to distinguish between the aged and unaged samples. Fig. 66 and Fig. 67 have shown that the wet aged samples have more attenuation and time delay when compared to the unaged sample. In order to verify this amount of time delay, the C-scan of the time signal of the wet samples at 57.73 ps has been shown in Fig. 86 and Fig. 87 indicates the A-scan of 4 time domain signals of the marked points. The more obvious difference is the attenuation of the wet samples of 0.15 [a.u.]. It is also seen that there is a delay in TOF between wet aged samples and dry

aged and unaged samples (see Table 7). In this table the ΔTOF is calculated, which is the TOF in the material from that the time of flight in air has been subtracted. The TOF in the air in all the tests is 18.83 ps, but because of its high intensity it is not shown in Fig. 87 and Fig. 89 to better show the differences between the unaged and aged signals.

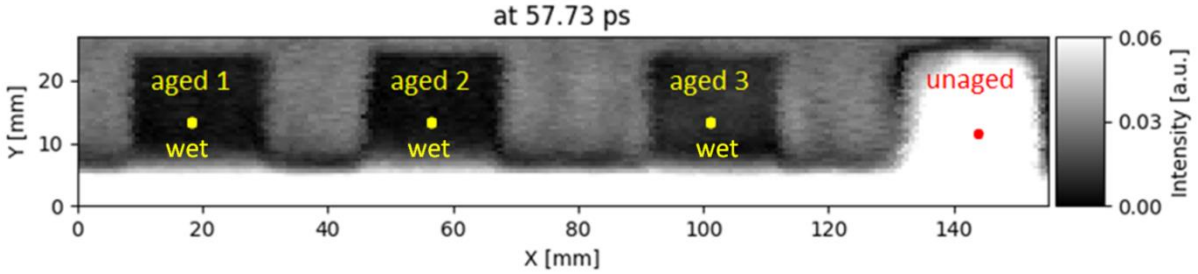

Fig. 86: THz scan surface of three wet aged and one unaged CIPP samples. Analysis of the time signal at time of 57.73 ps.

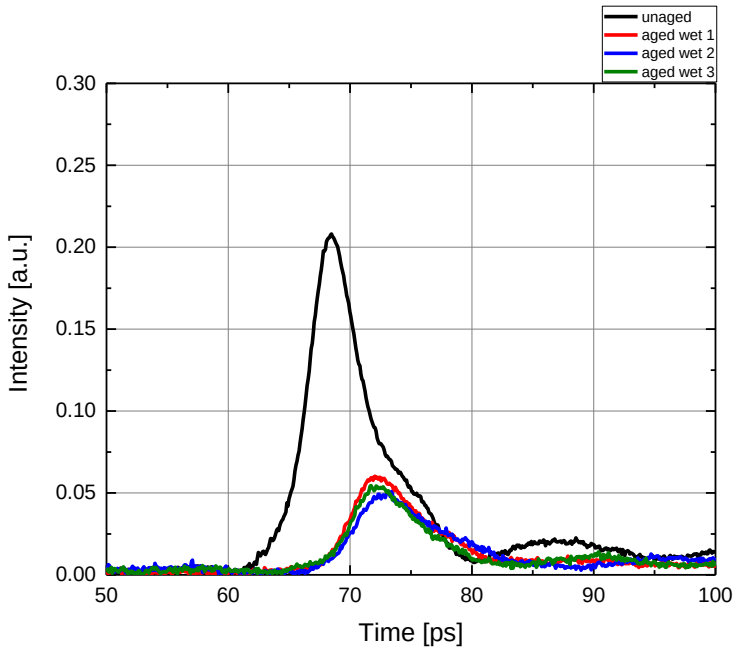

Fig. 87: THz time signal received in transmission mode revealing the characteristic absorption behavior of the 4 chosen points on the unaged and the wet aged samples.

It has been shown in 5.5.1 that the dry aged samples are distinguishable through the THz technique in TOF (Fig. 69). Fig. 88 and Fig. 89 show the same evaluation as Fig. 86 and Fig. 87 of the dry aged samples when compared to the unaged sample. It is seen that the aged samples have a maximum time delay of 1.83 ps in comparison to the unaged sample, but no differences in the intensity can be observed (Fig. 89, Table 7). Since this delay of time is less than 2 ps, it is assumed that this variation belongs to the change in the thickness.

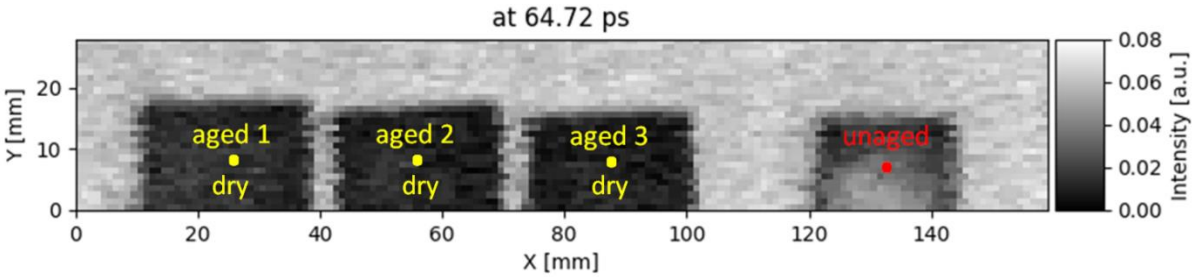

Fig. 88: THz scan surface of three dry aged and one unaged CIPP samples. Analysis of the time signal at time of 64.72 ps.

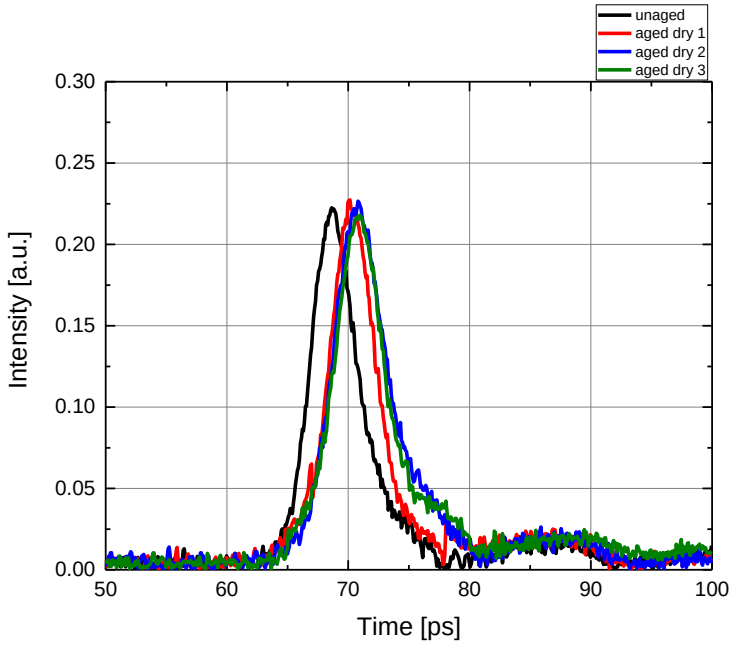

Fig. 89: THz time signal received in transmission mode revealing the characteristic absorption behavior of 4 chosen points on unaged and dry aged samples.

Table 7: ΔTOF of 4 points of CIPP samples in wet and dry aged conditions

Point	ΔTOF [ps]	ΔTOF [ps]
Unaged	50.15	49.98
aged 1	51.81 (wet)	51.81 (dry)
aged 2	53.28 (wet)	51.48 (dry)
aged 3	53.64 (wet)	51.48 (dry)

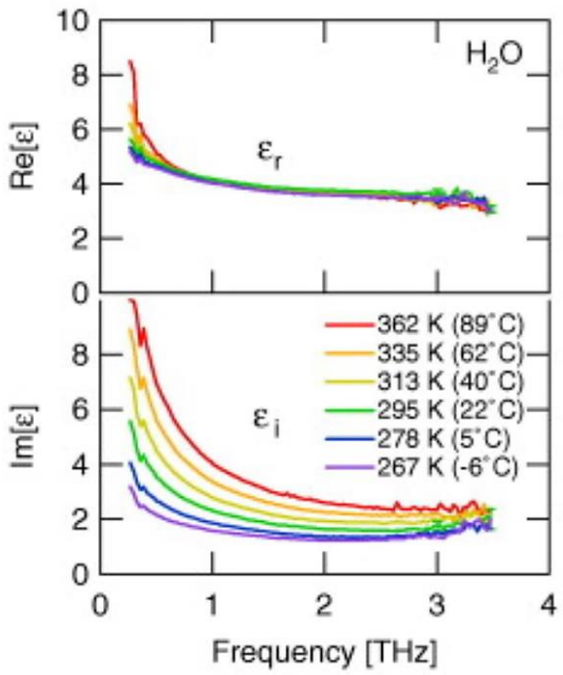

Fig. 90: Complex dielectric constants of liquid water at several temperatures as a function of the frequency [Yada 2008]

Fig. 90 shows the complex dielectric constant of water as a function of the frequency. At a room temperature of 22 °C, both the real and imaginary parts decreased exponentially with increasing frequency below 1 THz. It is possibly associated with dipole-dipole interactions due to the free rotation of water molecules having no more than one hydrogen bond, and then stay almost constant beyond 2 to 3 THz. It confirms that the THz system in the frequency range less than 1 THz is a reliable method to detect the existence of water in the material.

The spectrum analysis at the frequency of 1 THz in wet condition is shown in Fig. 91 and in dry condition is shown in Fig. 93. Fig. 91 shows the difference in intensity in the spectrum of wet and unaged samples. In order to better investigate the spectrum with respect to similarity in the time domain signal, 4 points were chosen to show the spectrum signal in the A-scan shown in Fig. 92. This figure indicates an attenuation of 0.4 [a.u.] in the wet samples.

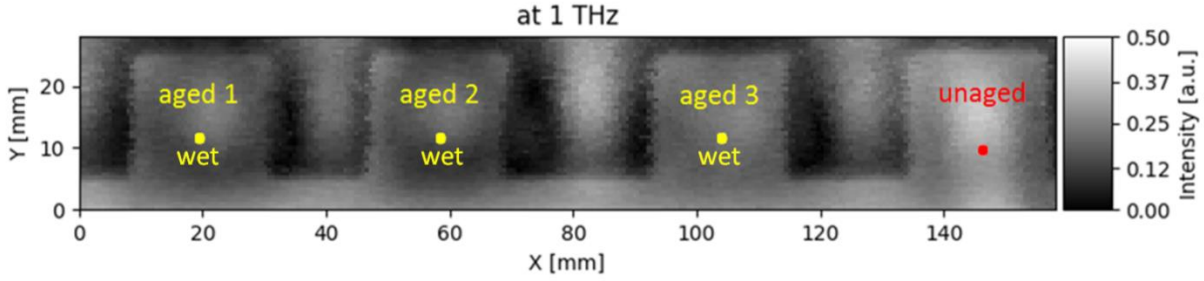

Fig. 91: THz scan surface of three wet aged and one unaged CIPP samples. Analysis of the spectrum signal at frequency of 1 THz

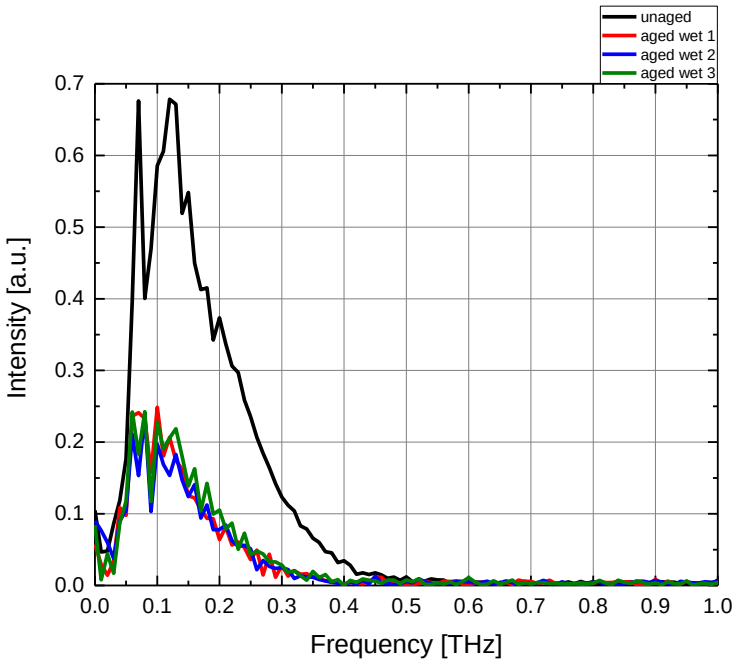

Fig. 92: Frequency spectra of THz signals received in transmission mode revealing the characteristic absorption behavior of 4 chosen points on unaged and wet aged samples.

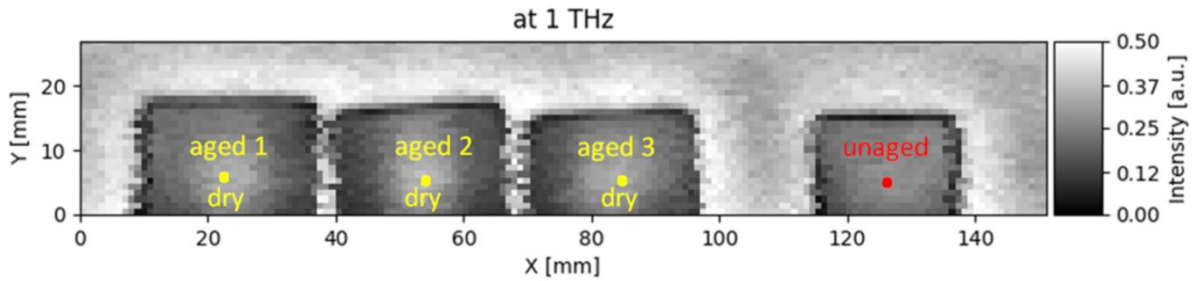

Fig. 93: THz scan surface of three dry aged and one unaged CIPP samples. Analysis of the spectrum signal at frequency of 1 THz

Fig. 93 shows the spectrum analysis of the dry aged samples at frequency of 1 THz. It is seen that the intensity cannot distinguish between the dry aged and unaged CIPP samples. The A-scan of the 4 points marked in Fig. 93 is shown in Fig. 94. In this figure the differences of spectrum signals between unaged and dry aged samples cannot be differentiated from each other.

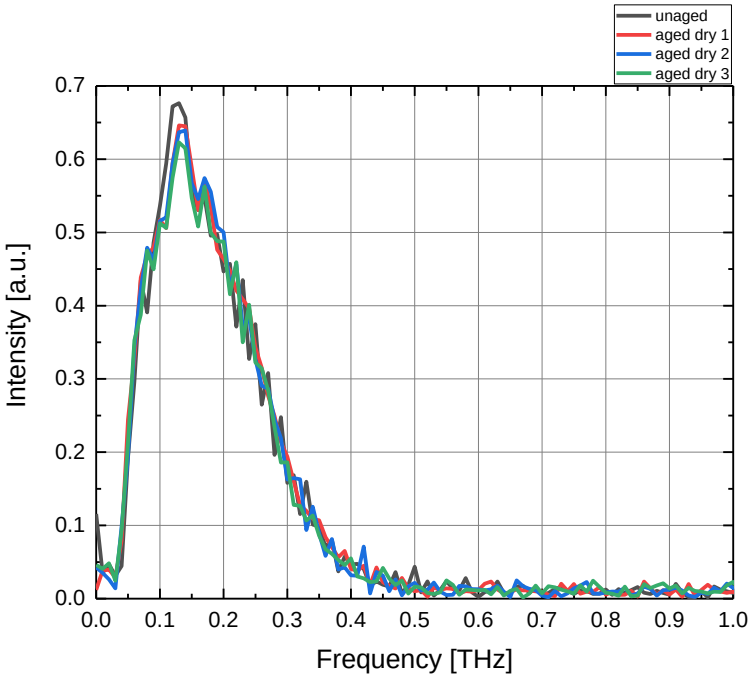

Fig. 94: Frequency spectra of THz signals received in transmission mode revealing the characteristic absorption behavior of 4 chosen points on unaged and dry aged samples.

6.5.2 Geometrical defects

It has been shown in 5.5.2 that when considering the time of flight evaluation, it is possible to characterize more defects. The time of flight increases according to the permittivity and thickness of the material. It means that the air contributes to the shortest portion within TOF and parts of the sample without any FBHs have the longest TOF. The TOF depends on the distance between emitter and detector. As it can be seen in Fig. 71f and g, three first columns are distinguishable with the exception of FBHs 9 and10. The parameter Signal Min TOF has the same results but the FBH 5 is not detectable. The FBHs with the same depths are expected to appear in the same colors. It is seen from Fig. 71 that the represented depths of the FBHs match the real depths of the FBHs but for the not deep FBHs the presented diameters are not reliable. It is shown that the diameters of FBHs with depth of 6 and 2 mm appear smaller than the real size. The envelope width analysis helps to detect all the first 8 FBHs in Fig. 71h but this analysis is just suitable to detect the existence of the FBHs 9 and 10 but not with regard to their size and depth. Comparatively, the TOF parameters are more suitable for the evaluation allowing the depth of the defects to be distinguished. The fourth column with 3 mm diameter is not visible with any parameter analysis. It is shown that the lateral resolution is more than 3 mm.

6.5.3 Curing

In 5.5.3 the spectrum and different parameters in two-dimensional analysis were investigated. In order to better compare the spectrum signal, three points of both areas, marked in Fig. 77 have been investigated and discussed in chapter 6.5.3, where the results are shown in Fig. 95. It is seen that there is a little bit of attenuation between the spectra in two parts and the attenuation at the partially cured points is more but it is too small to be detected in a C-Scan. This small attenuation was therefore not detectable in parameters considered for the analysis. In this context, the importance of different signal processing analysis methods is understandable.

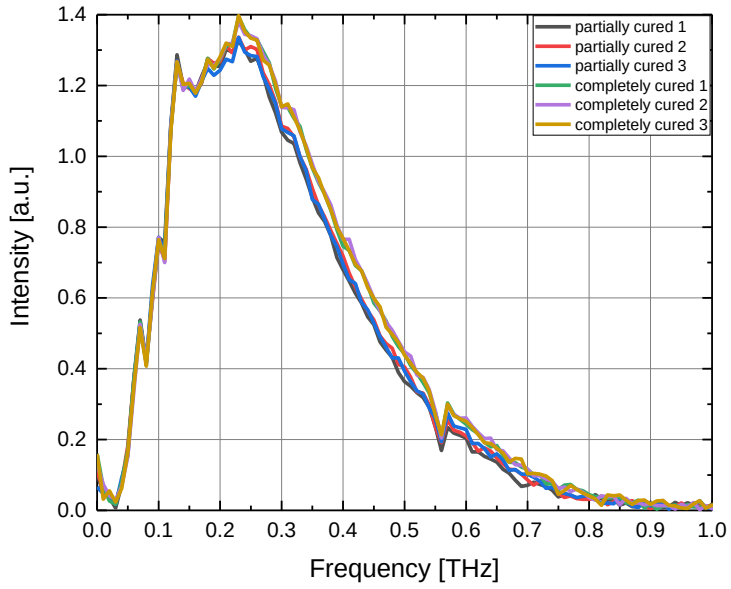

Fig. 95: Frequency spectrum of THz signals at 1 THz received in transmission mode revealing the characteristic absorption behavior of the cured and not cured part

Considering the time domain signal Fig. 96 clearly shows the difference of intensities of the envelope and the TOF. The cross section of the surface image not only presents the cured and not cured parts but also the trend of the curing process in different amounts of amplitude at the time of 43.4 ps.

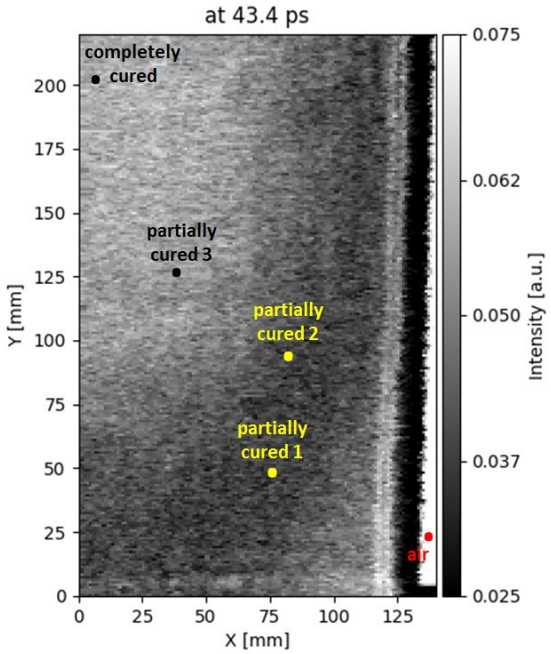

Fig. 96: THz scan surface of 140 mm×220 mm of the partially cured sample. The cross section of the analysis of the time signal, perpendicular to the signal propagation at 43.4 ps.

In order to better compare the TOF, 5 points in different ranges of grey color scale being analogous to different amplitudes have been chosen in Fig. 96. Fig. 97 indicates the time signals of these 5 points. It is observed that the peaks of the envelope at different positions of the sample appear in time around 39 ps. It is therefore the optimum range with respect to time to inspect the time domain signal as shown in Fig. 96. This figure shows that the THz signal needs 18.76 ps to transmit between the emitter and the detector. Points 1 to 3 have a TOF of 38.28, 38.79, 39.18 ps respectively compared to 39.47 ps in the completely cured part.

Fig. 97 also indicates that moving from point 1 towards the cured part; the intensity of the signal rises and shows that the dissipation of the signal decreases with improvement of the curing and crosslinking process. The high attenuation in the partially cured area confirms the results of Fig. 96 and the increasing time of flight in the fully cured section proves the results shown in Fig. 76a, b and c. The reason that the results shown in Fig. 76d cannot differ between the cured and uncured areas becomes obvious from Fig. 97. The envelope width of both areas is almost the same and only the time of flight of the envelope peak changes. This can be explained through the real part (ε') and the imaginary part (ε'') of the dielectric parameter. ε' measures the amount of the energy from the external electric field stored in the material but ε'' refers to the dissipation of the energy in the medium. In this case, it can be assumed that the uncured and partially cured CIPP has less ε' and higher ε''.

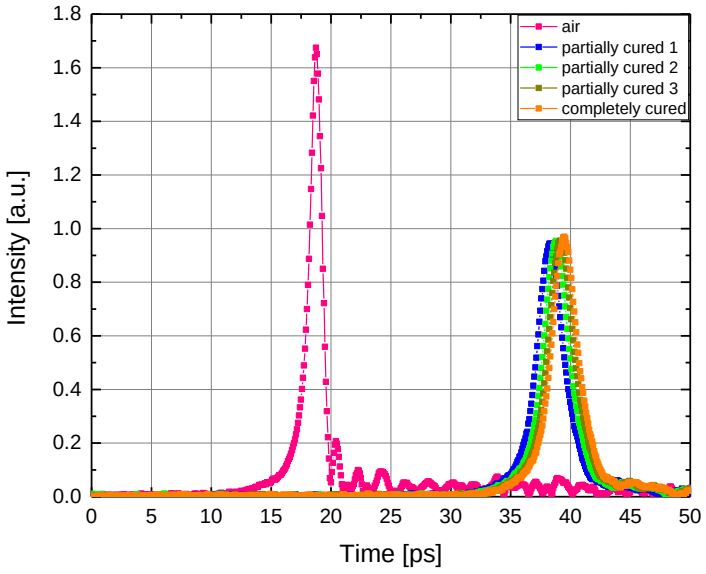

Fig. 97: THz scan surface of 140 mm×220 mm of partially cured sample. Analysis of the time signal of 5 points at different locations on the sample.

By knowing the time delay of every point compared to air, it is possible to calculate ε'_r with the following equation:

$$\varepsilon_r^{'} = \left(\frac{C_0 \Delta TOF}{x} + 1\right)^2 \qquad \text{Eq. 46}$$

where

C_0 is the speed of light [m/s],

ΔTOF is the time of flight in the material subtracted by the time of flight in air [s] and

x is the thickness of the material [m].

The results of the ε'_r calculation are shown in Table 8.

Table 8: ε'_r calculation of 4 points of the partially cured sample

Point	ΔTOF [ps]	ε'_r
Partially cured 1	19.52	2.85
Partially cured 2	20.03	2.91
Partially cured 3	20.42	2.96
Completely cured	20.71	2.99

As observed with the THz system, the variation of the real permittivity is detectable, whereas with the microwaves method, it was only possible to differentiate the signal intensities of the cured and partially cured material.

6.6 **Analysis by ultrasound**

6.6.1 Aging

In section 5.6.1 with comparing the Fig. 78a, b, a reduction of attenuation in the wet condition after aging could be shown. Attenuation is defined from the ratio of the reflected signal amplitudes from the interfaces. The two main mechanisms, which cause the attenuation of ultrasound energy, are absorption and scattering. As a material is exposed to a wave, an amount of the energy of the wave is stored and some of the energy is lost and converted to heat. This is referred to as energy dissipation or absorption. The fraction of the lost energy over stored energy is known as loss factor or damping coefficient, which signifies the degree to which a material dissipates or absorbs energy. The damping coefficient is found to be dependent on temperature and frequency of the wave. It increases with the frequency while it is almost constant at temperatures under T_g [Krautkrämer 1969; Krautkrämer 1990]. Another reason for attenuation is scattering, which is a consequence of inhomogeneity in a material such as crystal discontinuities, grain boundaries, inclusions, particles and voids. It causes the conversion of the coherent, collimated waves into incoherent, divergent waves through reflection and refraction. The scattering is a function of the wavelength. Therefore, it increases when the frequency increases. The scattering from inclusions in a medium becomes significant only when the dimensions of the inclusions are comparable to the wavelength of sound in the medium. For polycrystalline metals and ceramics, scattering is the main mechanism that causes attenuation. Though, for liquids and polymers, absorption dominates [Krautkrämer 1969; Krautkrämer 1990].

Changing the frequency while the speed of sound is fixed will result in changing the wavelength of the sound. The wavelength of the used ultrasound has an important effect on detecting a discontinuity. A general rule of thumb is that a discontinuity should be larger than one-half of the wavelength to have a chance of being detected. Sensitivity and resolution are two terms that are usually used in ultrasonics. Sensitivity is the ability to locate small discontinuities and generally increases with higher frequency (shorter wavelengths). Resolution is the ability to locate discontinuities that are close together within the material or located near the part surface. The resolution also generally increases, when the frequency increases. However choosing a high frequency lowers the penetration of the ultrasound waves because of higher scattering.

The plasticization increases the speed of sound in CIPP samples, because the water molecules diffuse between the UPR's molecules and chains as a plasticizer and they fill the micro-cracks, debonding and pores by replacing the air molecules in the material. Increasing the speed while the frequency is fixed, increases the wavelength with the same resolution and sensitivity but less scattering and therefore

more penetration. The less scattering and more penetration enable the detection of the back-wall of the CIPP samples in the wet aged condition. As it is seen, even after aging in wet condition, the back-wall echo is still difficult to be detected. It shows that the rise of the speed and increase of the wavelength was not that much large.

6.6.2 Geometrical defects

The resolution in the C-scan depends on the step size of the manipulator. In the test described in chapter 5.6.2 steps of 0.55 mm were entered in both directions x and y. The resolution in depth is equal to the wavelength of the sound wave, which means that the resolution in depth depends on the applied frequency and the speed of sound in the material. Since the speed of sound in this CIPP sample has been determined to be 2650 m/s, the resolution calculated resulted in 1.1 mm. This amount of resolutions is the best resolution that can be achieved under ideal conditions. Certainly the resolution is affected by the test conditions, the material of the samples, the accuracy of FBHs, etc..

The ultrasound pulse generated by the transducer runs perpendicular to the surface and in the material. The pulse is then totally or partially reflected from the back-side of the CIPP sample. For this reason the back-side should be perpendicular to the propagation direction of the ultrasound wave. Since neither the front-wall nor the back-wall of the CIPP is totally flat, the echo can therefore not be completely reflected to the transducer, thus the back-wall echo is weak (see Fig. 80). The back-wall echo is reflected and travels opposite to the initial direction to reach the transducer after a certain TOF. In other cases, a part of the ultrasonic wave runs back and forth through the sample and once more generates a second back-wall echo with the double distance of the first back-wall echo (in the double TOF).

It is seen in Fig. 80 that the back-wall is not well detectable because of the absorption of the ultrasonic waves in the material, but when the sample is thinner, for example at FBH 2 and 7, it is not only possible to detect the back-wall of the FBHs, but also the second back-walls (FBHs 7 and 2) appear (see Fig. 80c). The second echoes are not definitive defects in the material, because their position is in the depth of about 11 mm exactly under the FBH 2 and 7, where there is water in the FBHs. The appearance of these echoes in the double depth of the FBHs 2 and 7 also confirms this assumption. These results show that the ultrasound technique is more suitable to investigate the thinner CIPP samples. It is due to the lower damping and attenuation of ultrasound waves in the material.

6.6.3 Curing

If the curing process in thermosetting polymers begins in the liquid or soft gel state there is an initial decrease in sound speed because of the change in viscosity, where the reduction in viscosity is due to a temperature increase. After a while, as the temperature is increased and material cures, the speed of sound increases, because the molecular structure is constrained and supports a higher acoustic wave

velocity. The rate of increase in sound speed then slows down as the rate of cure slows down as well and the reaction nears completion. Initially the polymer is viscous and has a high compressibility. The curing process decreases the compressibility and raises the sound velocity [Shepard 1997].

When the curing process proceeds in the solid composite, the state of the matter does not change at the start and after curing. The change in the velocity is therefore not very significant (see Fig. 81). The initial reduction in velocity can be associated with a reduction of density as a result of the production of voids in the matrix, which leads to a reduction in the sound velocity. As the curing proceeds, these voids are eventually removed and the velocity is once more observed to increase. It can be also related to the residual unreacted styrene monomer, which is not reacted during the curing because of insufficient temperature.

Fig. 82 shows that the curing process decreases the attenuation of the ultrasound waves and makes it even possible to detect the back-wall of the sample. The attenuation is strongly affected by the amount of curing agent present in the resin [Lionetto 2008]. The curing process causes the reaction of the remaining styrene in the matrix. This process follows the reduction of the ultrasound scattering in the material and this increases the amplitude. Also as the cure process proceeds, the length of the elements covalently linked, increases in the formation in the three-dimensional network, which increases the rigidity of the matrix.

7 Conclusion and future work

The phenomenon, which occurs in the cured in place pipe samples during the aging, refers to mechanical aging through the observation of cracks in the matrix and debonding in the matrix/fiber interface. This phenomenon occurs due to the plasticization of the material and exposure to water as a plasticizer. The effect of the plasticization on the polymer structure is temporary and the mechanical properties of the material will reverse after drying. The nanoindentation tests showed that the mechanical properties of cured in place pipe samples after aging only change in the saturated condition and after drying the properties reversed back to their initial amount again. Only using a local method like nanoindentation for characterization of the mechanical properties makes it possible to confirm that the hydrothermal aging acts as a mechanical aging and not as a chemical one, because this method is independent of debonding and crack formation in the material.

The results of this study have shown that during the hydrothermal aging, the weight of a CIPP sample totally increases. In that case there is weight increasing because of the absorbed water but also simultaneously loss of weight due to the dissolution of the coupling agent, which is shown after drying. The effect of aging was verified not only via nanoindentation testing but also via optical microscopic analysis.

Three different non-destructive methods namely microwaves, terahertz and ultrasound were used to inspect the hydrothermal aging, curing process and geometrical defects in the cured in place pipe samples. The investigation of hydrothermal aging through the non-destructive testing shows that before aging the thickness of the samples is measurable through microwaves and terahertz methods, while ultrasound testing can detect the back-wall echo of the samples only when they are saturated with water. In the saturated condition, the microwave method was unable to detect the back-wall echo because of the high absorption of microwaves. It can be concluded that terahertz, microwave and ultrasound testing can show the existence of water in cured in place pipe samples. The microwave and terahertz systems were also successful to distinguish the aged dry samples from the unaged samples via different time of flight because of the swelling during the hydrothermal aging in the material, which is irreversible. As a conclusion, a combination of electromagnetic and ultrasound testing makes the thickness measurement of the cured in place pipe samples possible.

Considering the geometrical defects, the terahertz technique had better results than microwaves, both in detecting the flat bottom holes and distinguishing their size. Although it has been shown that the ultrasound technique was a better choice to find the flat bottom holes when compared to terahertz, the ultrasound technique appeared to be a weaker method when it came to distinguish the size of the flat bottom holes.

Investigation of the curing process of the cured in place pipe sample through non-destructive methods shows that these methods are successful in detecting the curing trend. The terahertz and ultrasound techniques could distinguish the curing process both in terms of difference of time of flight and attenuation, while the microwave method could only differentiate this term through different attenuation. All of these detected parameters through the NDT methods can be seen in Table 9.

Table 9: Detected parameters through the NDT methods of CIPP samples

NDT methods	Detected parameters in unaged sample	Detected parameters in aged wet sample	Detected parameters in aged dry sample	Detected geometrical defects	Detected insufficient curing
Optical microscopy	Fibers and matrix	Fibers and matrix, osmotic cracks in matrix and debonding in interface of matrix and fibers		-	-
Nanoindentation	Loss and storage modulus, tan δ, hardness, indent displacement			-	-
Microwaves	Thickness, permittivity	Existence of water	Thickness, permittivity	FBHs with 10 mm diameter up to 2 mm depth and FBHs with 5 mm diameter up to 10 mm depth	yes
Terahertz	Thickness, permittivity	Existence of water, thickness, permittivity	Thickness, permittivity	FBHs with 10 and 5 mm diameters	yes
Ultrasound	Speed of sound	Existence of water, thickness, speed of sound	Speed of sound	See Table 4	yes

As mentioned above, this work has presented several original results about microwave, terahertz, ultrasound and nanoindentation measurements. However, it also opens many new doors for further work which could assist in investigation of additional features of this thesis. It is advised for future research, that the different amounts of absorbed water to be tested using non-destructive testing, to figure out at which amount absorbed water becomes detectable. It is also suggested to investigate other defects such as delamination, cracks, inclusion, etc. through these methods.

It is recommended for a next step to try non-destructive methods in a large pipeline, in which in situ manually performed measurements are possible. After that the results need to be verified in the laboratory. A step to follow would then be the automation of the measurement using pigging

technique, which can make measurement of the cured in place pipe in the pipes not being humanely accessible, possible.

8 References

[Ahmad 2010] Ahmad, M. R., Nakajima, M., Kojima, M., Kojima, S., Homma, M., & Fukuda, T. (2010). Fabrication and application of nanofork for measuring single cells adhesion force inside ESEM. In I. Staff (Ed.), *2010 International Conference on Enabling Science and Nanotechnology* (pp. 1–2). [Place of publication not identified]: IEEE. https://doi.org/10.1109/ESCINANO.2010.5700976

[Al-Kadhemy 2016] Al-Kadhemy, M. F. H., Rasheed, Z. S., & Salim, S. R. (2016). Fourier transform infrared spectroscopy for irradiation coumarin doped polystyrene polymer films by alpha ray. *Journal of Radiation Research and Applied Sciences*, *9*(3), 321–331. https://doi.org/10.1016/j.jrras.2016.02.004

[Allouche 2012] Allouche, E., Alam, S., Simicevic, J., Sterling, R., Condit, W., Headington, B., Downey, D. (2012). *A Retrospective Evaluation of Cured-in-Place Pipe (CIPP) Used in Municipal Gravity Sewers*. United states. Retrieved from Environmental Protection Agency website: https://nepis.epa.gov/Exe/ZyPDF.cgi/P100DQFP.PDF?Dockey=P100DQFP.PDF

[Allouche 2014] Allouche, E., Alam, S., Simicevic, J., Sterling, R., Condit, W., Matthews, J., & Selvakumar, A. (2014). A pilot study for retrospective evaluation of cured-in-place pipe (CIPP) rehabilitation of municipal gravity sewers. *Tunnelling and Underground Space Technology*, *39*, 82–93. https://doi.org/10.1016/j.tust.2012.02.002

[Apicella 1982] Apicella, A., Migliaresi, C., Nicodemo, L., Nicolais, L., Iaccarino, L., & Roccotelli, S. (1982). Water sorption and mechanical properties of a glass-reinforced polyester resin. *Composites*, *13*(4), 406–410. https://doi.org/10.1016/0010-4361(82)90151-3

[Apicella 1983] Apicella, A., Migliaresi, C., Nicolais, L., Iaccarino, L., & Roccotelli, S. (1983). The water ageing of unsaturated polyester-based composites: Influence of resin chemical structure. *Composites*, *14*(4), 387–392. https://doi.org/10.1016/0010-4361(83)90160-X

[Apicella 1981] Apicella, A., Nicolais, L., Astarita, G., & Drioli, E. (1981). Hygrothermal history dependence of equilibrium moisture sorption in epoxy resins. *Polymer*, *22*(8), 1064–1067. https://doi.org/10.1016/0032-3861(81)90293-7

[Bakeer 2007] Bakeer, R. M., & Firat Sever, V. (2008). Quantification of annular flow in lined pipelines. *Tunnelling and Underground Space Technology*, *23*(6), 727–733. https://doi.org/10.1016/j.tust.2007.12.008

[Bao 2002] Bao, L., & Yee, A. (2002). Effect of temperature on moisture absorption in a bismaleimide resin and its carbon fiber composites. *Polymer*, *43*(14), 3987–3997. https://doi.org/10.1016/S0032-3861(02)00189-1

[Beake 2006] Beake, B. (2006). Modelling indentation creep of polymers: a phenomenological approach. *Physics D: Applied Physics*, *39*(20), 4478–4485.

[Bélan 1997] Bélan, F., Bellenger, V., Mortaigne, B., & Verdu, J. (1997). Relationship between the structure and hydrolysis rate of unsaturated polyester prepolymers. *Polymer Degradation and Stability*, *56*(3), 301–309. https://doi.org/10.1016/S0141-3910(96)00203-0

[Bellenger 1995] Bellenger, V., Ganem, M., Mortaigne, B., & Verdu, J. (1995). Lifetime prediction in the hydrolytic ageing of polyesters. *Polymer Degradation and Stability*, *49*(1), 91–97. https://doi.org/10.1016/0141-3910(95)00049-R

[Bergeret 2009] Bergeret, A., Ferry, L., & Ienny, P. (2009). Influence of the fibre/matrix interface on ageing mechanisms of glass fibre reinforced thermoplastic composites (PA-6,6, PET, PBT) in a hygrothermal environment. *Polymer Degradation and Stability*, *94*(9), 1315–1324. https://doi.org/10.1016/j.polymdegradstab.2009.04.009

[Blitz 1997] Blitz, J. (1997). *Electrical and Magnetic Methods of Non-destructive Testing*. [S.l.]: Springer Netherlands.

[Blitz 1996] Blitz, J., & Simpson, G. (1996). *Ultrasonic methods of non-destructive testing* (1. ed.). *Non-destructive evaluation series*. London [u.a.]: Chapman & Hall.

[Bolt 1995] Bolt, R. H., & Hueter, T.F. (1995). *Sonics: Techniques for the use of sound and ultrasound in engineering and science*. New York: Wiley & Sons.

[Born 1980] Born, M., & Wolf, E. (1980). *Principles of optics : Electromagnetic theory of propagation, interference and diffraction of light*. Oxford: Pergamon Press.

[Bosseler 2009] Bosseler, B. (2009). *Abnahme von Liningmaßnahmen: Materialnachweise und Bewertung der Linerqualität*. Germany, Gelsenkirchen. Retrieved from Institut für Unterirdische Infrastruktur (IKT) website: http://www.ikt.de/website/down/f0150anhang.pdf

[Bovtun 2001] Bovtun, V., Stark, W., Kelm, J., Pashkov, V., & Yakimento, Y. (2001). Microwave characterisation of the crosslinking process: Cure of thermosets and vulcanisation of elastomers. *Materialprüfung*, *43*(1), 35–41.

[Bovtun 2005] Bovtun, V., Stark, W., Kelm, J., Pashkov, V., & Yakimenko, Y. (2005). Characterisation of carbon black filled rubber compounds by the Microwave Coaxial Method. *Materialprüfung*, *47*(3), 118–122. https://doi.org/10.3139/120.100642

[Brückner 2010] Brückner, C. (2010). THz-Optiken für Bildgebungssysteme (Dr.-Ing.). Friedrich-Schiller-Universität, Germany, Jena. Retrieved from https://www.db-thueringen.de/servlets/MCRFileNodeServlet/dbt_derivate_00023849/Br%C3%BCckner/Dissertation.pdf

[Carey 2002] Carey, J. (2002). Near-field effects of terahertz pulses (Ph.D.). University of Strathclyde, Schottland, Glasgow. Retrieved from http://www.chem.gla.ac.uk/wynne/pubs/theses/2002-John-Carey.pdf

[Carter 1978] Carter, H. G., & Kibler, K. G. (1978). Langmuir-Type Model for Anomalous Moisture Diffusion In Composite Resins. *Journal of Composite Materials, 12*(2), 118–131. https://doi.org/10.1177/002199837801200201

[Cartz 1995] Cartz, L. (1995). *Nondestructive Testing: Radiography, Ultrasonics, Liquid Penetrant, Magnetic Particle, Eddy Current*: ASM International.

[Chakravartula 2006] Chakravartula, A., & Komvopoulos, K. (2006). Viscoelastic properties of polymer surfaces investigated by nanoscale dynamic mechanical analysis. *Applied Physics Letters, 88*(13), 131901. https://doi.org/10.1063/1.2189156

[Chan 2007] Chan, W. L., Deibel, J., & Mittleman, D. M. (2007). Imaging with terahertz radiation. *Reports on Progress in Physics (Rep. Prog. Phys.), 70*(8), 1325–1379. https://doi.org/10.1088/0034-4885/70/8/R02

[Chen 2013] Chen, Z., & Diebels, S. (2013). Parameter re-identification in nanoindentation problems of viscoelastic polymer layers: small deformation: ZAMM.Z.Angew.Math.Mech. *ZAMM - Journal of Applied Mathematics and Mechanics / Zeitschrift für Angewandte Mathematik und Mechanik, 93*(2-3), 88–101.

[Cheng 2000] Cheng, L., Xia, X., Yu, W., Scriven, L. E., & Gerberich, W. W. (2000). Flat-punch indentation of viscoelastic material. *Journal of Polymer Science Part B: Polymer Physics, 38*(1), 10–22. https://doi.org/10.1002/(SICI)1099-0488(20000101)38:1<10::AID-POLB2>3.0.CO;2-6

[Chieruzzi 2013] Chieruzzi, M., Miliozzi, A., & Kenny, J. M. (2013). Effects of the nanoparticles on the thermal expansion and mechanical properties of unsaturated polyester/clay nanocomposites. *Composites Part A: Applied Science and Manufacturing, 45*, 44–48. https://doi.org/10.1016/j.compositesa.2012.09.016

[Christian 2012] Christian, S. J., & Billington, S. L. (2012). Moisture diffusion and its impact on uniaxial tensile response of biobased composites. *Composites Part B: Engineering, 43*(5), 2303–2312. https://doi.org/10.1016/j.compositesb.2011.11.063

[Cohen 2013] Cohen, S., & Kalfon-Cohen, E. (2013). Dynamic nanoindentation by instrumented nanoindentation and force microscopy: A comparative review. *Beilstein journal of nanotechnology, 4*, 815–833. https://doi.org/10.3762/bjnano.4.93

[Dai 2013] Dai, K., Song, L., Jiang, S., Yu, B., Yang, W., Yuen, R. K.K., & Hu, Y. (2013). Unsaturated polyester resins modified with phosphorus-containing groups: Effects on thermal properties and flammability. *Polymer Degradation and Stability*, *98*(10), 2033–2040. https://doi.org/10.1016/j.polymdegradstab.2013.07.008

[Deuschle 2007] Deuschle, J., Enders, S., & Arzt, E. (2007). Surface detection in nanoindentation of soft polymers. *Journal of Materials Research*, *22*(11), 3107–3119. https://doi.org/10.1557/JMR.2007.0394

[Deutsch 2002] Deutsch, V., Platte, M., Schuster, V., & Deutsch, W. (2002). *Measurements with Ultrasound : NDT-Compact and understandable*. Germany, Wuppertal: Castell.

[Deutsch 1999] Deutsch, V. (1999). *Informationsschriften zur zerstörungsfreien Prüfung: ZfP kompakt und verständlich*. Wuppertal: Castell-Verl.

[Díez-Pascual 2015] Díez-Pascual, A. M., Gómez-Fatou, M. A., Ania, F., & Flores, A. (2015). Nanoindentation in polymer nanocomposites. *Progress in Materials Science*, *67*, 1–94. https://doi.org/10.1016/j.pmatsci.2014.06.002

[Dilg 2007] Dilg, R. (2007). Schlauchlining im Sammler: Verfahren, Regelwerke, Materialien, Einbau-/Aushärtetechniken und Entwicklungen. *3R Zeitschrift für die Rohrleitungspraxis*. Retrieved from http://www.aarsleff-gmbh.de/uploads/tx_nxttcontentadditionalfields/rsv-sonderteil_10_07_Schlauchlining.pdf

[Doherty 2005] Doherty, I. (2005). *Quality Controls Are Key To Successful CIPP Lateral Lining Applications*. Germany, Bochum. Retrieved from Stein & Partner GmbH website: http://old.unitracc.de/aktuelles/artikel/quality-controls-are-key-to-successful-cipp-lateral-lining-applications-en

[Dokukin 2015] Dokukin, M., & Sokolov, I. (2015). High-resolution high-speed dynamic mechanical spectroscopy of cells and other soft materials with the help of atomic force microscopy. *Scientific reports*, *5*, 12630. https://doi.org/10.1038/srep12630

[Dub 2008] Dub, S., & Trunov, M. (2008). Determination of viscoelastic material parameters by step-loading nanoindentation. *Physics D: Applied Physics*, *41*(7).

[Duersch 2004] Duersch, M. (2004). BYU micro-SAR: a very small, low-power LFM-CW synthetic aperture radar (Master of Science). Brigham Young University, United States, Utah.

[Fink 2013] Fink, J. (2013). *Reactive polymers fundamentals and applications: A concise guide to industrial polymers* (Second edition). *PDL handbook series*. Norwich, N.Y., London: William Andrew; Elsevier Health Sciences [distributor].

[Fitzgerald 2005] Fitzgerald, A. J., Cole, B. E., & Taday, P. F. (2005). Nondestructive analysis of tablet coating thicknesses using terahertz pulsed imaging. *Journal of pharmaceutical sciences*, *94*(1), 177–183. https://doi.org/10.1002/jps.20225

[Foulc 2005] Foulc, M. P., Bergeret, A., Ferry, L., Ienny, P., & Crespy, A. (2005). Study of hygrothermal ageing of glass fibre reinforced PET composites. *Polymer Degradation and Stability*, *89*(3), 461–470. https://doi.org/10.1016/j.polymdegradstab.2005.01.025

[Gautier 1999] Gautier, L., Mortaigne, B., & Bellenger, V. (1999). Interface damage study of hydrothermally aged glass-fibre-reinforced polyester composites. *Composites Science and Technology*, *59*(16), 2329–2337. https://doi.org/10.1016/S0266-3538(99)00085-8

[Gautier 2000] Gautier, L., Mortaigne, B., Bellenger, V., & Verdu, J. (2000). Osmotic cracking nucleation in hydrothermal-aged polyester matrix. *Polymer*, *41*(7), 2481–2490. https://doi.org/10.1016/S0032-3861(99)00383-3

[González-Partida 2008] González-Partida, J.-T., Almorox-González, P., Burgos-Garcia, M., & Dorta-Naranjo, B.-P. (2008). SAR System for UAV Operation with Motion Error Compensation beyond the Resolution Cell. *Sensors (Basel, Switzerland)*, *8*(5), 3384–3405. https://doi.org/10.3390/s8053384

[Gottstein 2007] Gottstein, G. (2007). *Physikalische Grundlagen der Materialkunde* (3rd ed.). Germany, Berlin: Springer.

[Gurtin 1979] Gurtin, M. E., & Yatomi, C. (1979). On a Model for Two Phase Diffusion in Composite Materials. *Journal of Composite Materials*, *13*(2), 126–130. https://doi.org/10.1177/002199837901300204

[Han 2003] Han, M.-H., & Nairn, J. A. (2003). Hygrothermal aging of polyimide matrix composite laminates. *Composites Part A: Applied Science and Manufacturing*, *34*(10), 979–986. https://doi.org/10.1016/S1359-835X(03)00154-4

[Hanemann 2010] Hanemann, T., Schumacher, B., & Haußelt, J. (2010). Polymerization conditions influence on the thermomechanical and dielectric properties of unsaturated polyester–styrene-copolymers. *Microelectronic Engineering*, *87*(1), 15–19. https://doi.org/10.1016/j.mee.2009.05.014

[Herbert 2008] Herbert, E., Oliver, W., & Pharr, G. (2008). Nanoindentation and the dynamic characterization of viscoelastic solids. *Physics D: Applied Physics*, *41*(7). Retrieved from http://iopscience.iop.org/article/10.1088/0022-3727/41/7/074021/pdf

[HP8510 2001] HP8510 (2001): Agilent Technologies 8510C Network Analyzer System. Operating and Programming Manual. Online verfügbar unter http://literature.cdn.keysight.com/litweb/pdf/08510-90281.pdf.

[Hysitron 2014] Hysitron. (2014). nanoDMA III User Manual. Retrieved from https://engineering.unl.edu/downloads/files/UserManual-HystrionTriboIndenter-sm.pdf

[Immergut 1965] Immergut, E., & Mark, H. (1965). *Platzer, plasticization and plasticizer processes avdances in chemistry: Principles of plasticization* (Vol. 48). Washington, D.C.: AMERICAN CHEMICAL SOCIETY.

[Kaatze 1989] Kaatze, U. (1989). Complex permittivity of water as a function of frequency and temperature. *Chemistry Engineering Data*, *34*, 371–374. Retrieved from https://pubs.acs.org/doi/pdf/10.1021/je00058a001

[Kampbell 2011] Kampbell, E., Downey, D., & Condit, W. (2011). *Quality Assurance and Quality Control Practices for Rehabilitation of Sewer and Water Mains*. United states. Retrieved from Environmental Protection Agency (EPA) website: https://nepis.epa.gov/Exe/ZyPDF.cgi/P100AFGW.PDF?Dockey=P100AFGW.PDF

[Kandelbauer 2014] Kandelbauer, A., Tondi, G., Zaske, O. C., & Goodman, S. H. (2014). Unsaturated Polyesters and Vinyl Esters. In *Handbook of Thermoset Plastics* (pp. 111–172). Elsevier. https://doi.org/10.1016/B978-1-4557-3107-7.00006-3

[Karbhari 2013] Karbhari, V. M. (Ed.). (2013). *Non-destructive evaluation (Nde) of polymer matrix composites: Techniques and applications*. *Woodhead publishing series in composites science and engineering: Vol. 43*. Oxford: Woodhead publ.

[Kattan 2002] Kattan, M., Dargent, E., & Grenet, J. (2002). Three phase model in drawn thermoplastic polyesters: Comparison of differential scanning calorimetry and thermally stimulated depolarisation current experiments. *Polymer*, *43*(4), 1399–1405. https://doi.org/10.1016/S0032-3861(01)00719-4

[Kolano 2010] Kolano, M. (2010). Untersuchung zur Signalentstehung und Rauschunterdrückung in einem Terahertz Zeitbereichs Spektroskopie System (Diplomarbeit). Technischen Universität Kaiserslautern, Germany, Kaiserslautern.

[Krautkrämer 1969] Krautkrämer, H., & Krautkrämer, J. (1969). *Ultrasonic testing of materials*. Berlin: Springer.

[Krautkrämer 1986] Krautkrämer, H., & Krautkrämer, J. (1986). *Werkstoffprüfung mit Ultraschall*. Berlin: Springer.

[Krautkrämer 1990] Krautkrämer, J., & Krautkrämer, H. (1990). *Ultrasonic testing of materials* (4th fully rev. ed.). Berlin, New York: Springer-Verlag.

[Kupfer 2005] Kupfer, K. (2005). *Electromagnetic Aquametry : Electromagnetic Wave Interaction with Water and Moist Substances*. Berlin: Springer.

[Laoubi 2014] Laoubi, K., Hamadi, Z., Ahmed Benyahia, A., Serier, A., & Azari, Z. (2014). Thermal behavior of E-glass fiber-reinforced unsaturated polyester composites. *Composites Part B: Engineering*, *56*, 520–526. https://doi.org/10.1016/j.compositesb.2013.08.085

[Lassila 2002] Lassila, L.V.J., Nohrström, T., & Vallittu, P. K. (2002). The influence of short-term water storage on the flexural properties of unidirectional glass fiber-reinforced composites. *Biomaterials*, *23*(10), 2221–2229. https://doi.org/10.1016/S0142-9612(01)00355-6

[Launay 1999] Launay, A., Thominette, F., & Verdu, J. (1999). Hydrolysis of poly(ethylene terephtalate). A steric exclusion chromatography study. *Polymer Degradation and Stability*, *63*(3), 385–389. https://doi.org/10.1016/S0141-3910(98)00116-5

[Levine 1988] Levine, H., & Slade, L. (1988). Water as a plasticizer: Physico-chemical aspects of low-moisture polymeric systems. In F. Franks (Ed.), *Water Science Reviews 3* (pp. 79–185). Cambridge: Cambridge University Press. https://doi.org/10.1017/CBO9780511552083.002

[Lionetto 2008] Lionetto, F., & Maffezzoli, A. (2008). Polymer characterization by ultrasonic wave propagation. *Advances in Polymer Technology*, *27*(2), 63–73. https://doi.org/10.1002/adv.20124

[Liu 2013] Liu, J., Chen, J., Wang, T., Li, Y., Liu, F., Li, L.,. . . Wang, Z. (2013). High efficiency and high power continuous-wave semiconductor terahertz lasers at ∼3.1THz. *Solid-State Electronics*, *81*, 68–71. https://doi.org/10.1016/j.sse.2013.01.014

[Lunkenheimer 2017] Lunkenheimer, P., Emmert, S., Gulich, R., Köhler, M., Wolf, M., Schwab, M., & Loidl, A. (2017). Electromagnetic-radiation absorption by water. *Physical review. E*, *96*(6-1), 62607. https://doi.org/10.1103/PhysRevE.96.062607

[Ma 1993] Ma, S., & Yu, T. (1993). The glass transition temperature of crosslinked unsaturated polyester. *Polymer Engineering*, *12*, 179–195.

[Mafi 2005] Mafi, R., Mirabedini, S. M., Attar, M. M., & Moradian, S. (2005). Cure characterization of epoxy and polyester clear powder coatings using Differential Scanning Calorimetry (DSC) and Dynamic Mechanical Thermal Analysis (DMTA). *Progress in Organic Coatings*, *54*(3), 164–169. https://doi.org/10.1016/j.porgcoat.2005.06.006

[Manavipour 2014] Manavipour, M., Kurz, J., Sklarczyk, C., & Boller, C. 2014. *The Effect of Water Aging on Cured-In-Place Pipe (CIPP) Samples Using Non-Destructive Tests.*

[Manavipour 2016] Manavipour, M., Sklarczyk, C., Szielasko, K., Kurz, J., & Boller, C. 2016. *Detection of hydrothermal aging in Cured-In-Place Pipes (CIPP) based on microwave system*: Deutsche Gesellschaft für Zerstörungsfreie Prüfung e.V. (DGZfP).

[Marais 1999] Marais, S., Metayer, M., Labbe, M., Legras, M. T., & Saiter, J. M. (1999). Water diffusion in unsaturated polyester films. Effect of plasticization on the glass transition. *Polymer Engineering & Science*, *39*(8), 1508–1516. https://doi.org/10.1002/pen.11543

[Marais 2000] Marais, S., Metayer, M., Nguyen, T. Q., Labbe, M., & Saiter, J. M. (2000). Diffusion and permeation of water through unsaturated polyester resins—influence of resin curing. *European Polymer Journal*, *36*(3), 453–462.https://doi.org/10.1016/S0014-3057(99)00080-4

[Martin 2008] Martin, R. (2008). *Ageing of composites*. England: Cambridge : Woodhead.

[Matthews 2011] Matthews, J., Condit, W., & Mckim, R. (2011). *Decision Support for Renewal of Wastewater Collection and Water Distribution Systems*. United states. Retrieved from Environmental Protection Agency (EPA) website: https://nepis.epa.gov/Exe/ZyPDF.cgi/P100BWUR.PDF?Dockey=P100BWUR.PDF

[Matthews 2018] Matthews, J. C., Allouche, E., Vladeanu, G., & Alam, S. (2018). Multi-segment trenchless technology method selection algorithm for buried pipelines. *Tunnelling and Underground Space Technology*, *73*, 295–301. https://doi.org/10.1016/j.tust.2018.01.001

[McKeen 2014] McKeen, L. W. (2014). Polyesters. In *The Effect of Long Term Thermal Exposure on Plastics and Elastomers* (pp. 85–115). Elsevier. https://doi.org/10.1016/B978-0-323-22108-5.00005-9

[Moll 2013] Moll, J., Manavipour, M., Sklarczyk, C., Krozer, V., & Boller, C. 2013. *Millimeter-wave non-destructive testing of a cured in place pipe sample*: IEEE Transactions on Terahertz Science and Technology.

[Mortaigne 1999] Mortaigne, B., Bourbigot, S., Le Bras, M., Cordellier, G., Baudry, A., & Dufay, J. (1999). Fire behaviour related to the thermal degradation of unsaturated polyesters. *Polymer Degradation and Stability*, *64*(3), 443–448. https://doi.org/10.1016/S0141-3910(98)00149-9

[Muenchmeyer 2007] Muenchmeyer, G. (Ed.) 2007. *A Higher Level of Quality & Testing for CIPP Installations is a Reality.*

[Nava 2003] Nava, D., Salom, C., Prolongo, M. G., & Masegosa, R. M. (2003). Thermal properties and interactions in blends of poly(ε-caprolactone) with unsaturated polyester resins. *Journal of Materials Processing Technology*, *143-144*, 171–174. https://doi.org/10.1016/S0924-0136(03)00401-1

[Navab-Kashani 2014] Navab-Kashani, R. (2014). Productivity Analysis of Closed Circuit Television (CCTV) Sewer Mainline Inspection (Master of Science). University of Alberta. Retrieved from https://era.library.ualberta.ca/communities/db9a4e71-f809-4385-a274-048f28eb6814/collections/f42f3da6-00c3-4581-b785-63725c33c7ce

[Nogueira 2001] Nogueira, P., Ramrez, C., Torres, A., Abad, M. J., Cano, J., Lpez, J.,. . . Barral, L. (2001). Effect of water sorption on the structure and mechanical properties of an epoxy resin system. *Journal of Applied Polymer Science*, *80*(1), 71–80. https://doi.org/10.1002/1097-4628(20010404)80:1<71::AID-APP1077>3.0.CO;2-H

[Nyfors 1989] Nyfors, E., & Vainikainen, P. (1989). *Industrial microwave sensors*. *The Artech House Microwave Library*. Norwood, Massachusetts: Artech House.

[Oliver 2004] Oliver, W. C., & Pharr, G. M. (2004). Measurement of hardness and elastic modulus by instrumented indentation: Advances in understanding and refinements to methodology. *Journal of Materials Research*, *19*(01), 3–20. https://doi.org/10.1557/jmr.2004.19.1.3

[Oyen 2003] Oyen, M. L., & Cook, R. F. (2003). Load–displacement behavior during sharp indentation of viscous–elastic–plastic materials. *Journal of Materials Research*, *18*(01), 139–150. https://doi.org/10.1557/JMR.2003.0020

[Penders 2012] Penders, A., & Melendrez, D. (2012). *Environmental Effects of Cured-in-Place Pipe Repairs*. Retrieved from CTC & Associates LLC website: http://www.dot.ca.gov/research/researchreports/preliminary_investigations/docs/cured_in_place_pipe_preliminary_investigation_6-26-12.pdf

[Potiyaraj 2007] Potiyaraj, P., Klubdee, K., & Limpiti, T. (2007). Physical properties of unsaturated polyester resin from glycolyzed pet fabrics. *Journal of Applied Polymer Science*, *104*(4), 2536–2541. https://doi.org/10.1002/app.25923

[Ridzuan 2016] Ridzuan, M.J.M., Majid, M. A., Afendi, M., Mazlee, M. N., & Gibson, A. G. (2016). Thermal behaviour and dynamic mechanical analysis of Pennisetum purpureum /glass-reinforced epoxy hybrid composites. *Composite Structures*, *152*, 850–859. https://doi.org/10.1016/j.compstruct.2016.06.026

[Romanzini 2015] Romanzini, D., Frache, A., Zattera, A. J., & Amico, S. C. (2015). Effect of clay silylation on curing and mechanical and thermal properties of unsaturated polyester/montmorillonite nanocomposites. *Journal of Physics and Chemistry of Solids*, *87*, 9–15. https://doi.org/10.1016/j.jpcs.2015.07.019

[Rösler 2007] Rösler, J., Bäker, M., & Harders, H. (2007). *Mechanical Behaviour of Engineering Materials: Metals, Ceramics, Polymers, and Composites*. Berlin, Heidelberg: Springer.

[Sahu 2018] Sahu, S. K., Badgayan, N. D., Samanta, S., & Rama Sreekanth, P. S. (2018). Quasistatic and dynamic nanomechanical properties of HDPE reinforced with 0/1/2 dimensional carbon nanofillers based hybrid nanocomposite using nanoindentation. *Materials Chemistry and Physics*, *203*, 173–184. https://doi.org/10.1016/j.matchemphys.2017.09.063

[Sawpan, Pickering 2012] Sawpan, M. A., Pickering, K. L., & Fernyhough, A. (2012). Flexural properties of hemp fibre reinforced polylactide and unsaturated polyester composites. *Composites Part A: Applied Science and Manufacturing*, *43*(3), 519–526. https://doi.org/10.1016/j.compositesa.2011.11.021

[Sawpan, Holdsworth 2012] Sawpan, M. A., Holdsworth, P. G., & Renshaw, P. (2012). Glass transitions of hygrothermal aged pultruded glass fibre reinforced polymer rebar by dynamic mechanical thermal analysis. *Materials & Design*, *42*, 272–278. https://doi.org/10.1016/j.matdes.2012.06.008

[Shepard 1997] Shepard, D., Smith, K. (1997). A new ultrasonic measurement system for the cure monitoring of thermosetting resins and composites. *Thermal Analysis*, *49*(1), 95–100.

[Shtarkman 1983] Shtarkman, B., & Razinskaya, I. (1983). Plasticization mechanism and structure of polymers. *Acta Polymerica*, *34*, 514–520.

[Sokoll 2009] Sokoll, O., Diburg, B., & Beck, S. (2009). *Abnahme von Liningmaßnahmen-Materialnachweise und Bewertung der Linerqualität*. Germany, Gelsenkirchen. Retrieved from http://www.ikt.de/website/down/f0150kurzbericht.pdf

[Soumekh 1999] Soumekh, M. (1999). *Synthetic aperture radar signal processing with MATLAB algorithms*. New York: Wiley.

[Spathis 2012] Spathis, G., & Kontou, E. (2012). Creep failure time prediction of polymers and polymer composites. *Composites Science and Technology*, *72*(9), 959–964. https://doi.org/10.1016/j.compscitech.2012.03.018

[Srivastava 1999] Srivastava, V. K. (1999). Influence of water immersion on mechanical properties of quasi-isotropic glass fibre reinforced epoxy vinylester resin composites. *Materials Science and Engineering: A*, *263*(1), 56–63. https://doi.org/10.1016/S0921-5093(98)01037-5

[ASTM International D 570 – 98] ASTM International D 570 – 98. *Standard test method for water absorption of plastics*. England, Cambridge: Cambridge Univ. Press.

[Sterling 2010] Sterling, R., Simicevic, J., Allouche, E., Condit, W., & Wang, L. (2010). *State of Technology for Rehabilitation of Wastewater Collection Systems*. United states. Retrieved from Environmental Protection Agency (EPA) website: https://nepis.epa.gov/Exe/ZyPDF.cgi/P1008C45.PDF?Dockey=P1008C45.PDF

[Sterling 2016] Sterling, R., Alam, S., Allouche, E., Condit, W., Matthews, J., & Downey, D. (2016). Studying the Life-cycle Performance of Gravity Sewer Rehabilitation Liners in North America. *Procedia Engineering*, *165*, 251–258. https://doi.org/10.1016/j.proeng.2016.11.797

[Szielasko 2017] Szielasko, K., Stumm, C., Manavipour, M., & Sasaki, K. (2017). Nondestructive Characterization of Dielectric Materials with Scanning Terahertz Spectroscopy. *Electromagnetic Nondestructive Evaluation*, *42*, 61–66.

[Thomason 1995] Thomason, J. (1995). The interface region in glass fibre-reinforced epoxy resin composites: 2, Water absorption, voids and the interface. *Composite*, *26*, 477–485.

[Tredicucci 2004] Tredicucci, A., Köhler, R., Beltram, F., Beere, H.E., Linfield, E.H., Davies, A.G., & Ritchie, D.A. (2004). Terahertz quantum cascade lasers. *Physica E: Low-dimensional Systems and Nanostructures*, *21*(2-4), 846–851. https://doi.org/10.1016/j.physe.2003.11.137

[Trihotri 2015] Trihotri, M., Dwivedi, U. K., Khan, F. H., Malik, M. M., & Qureshi, M. S. (2015). Effect of curing on activation energy and dielectric properties of carbon black–epoxy composites at different temperatures. *Journal of Non-Crystalline Solids*, *421*, 1–13. https://doi.org/10.1016/j.jnoncrysol.2015.04.020

[Tsenoglou 2006] Tsenoglou, C. J., Pavlidou, S., & Papaspyrides, C. D. (2006). Evaluation of interfacial relaxation due to water absorption in fiber–polymer composites. *Composites Science and Technology*, *66*(15), 2855–2864. https://doi.org/10.1016/j.compscitech.2006.02.022

[Wang 2007] Wang, Y., & Hahn, T. H. (2007). AFM characterization of the interfacial properties of carbon fiber reinforced polymer composites subjected to hygrothermal treatments. *Composites Science and Technology*, *67*(1), 92–101. https://doi.org/10.1016/j.compscitech.2006.03.030

[Westaway 2001] Westaway, D. (2001). Cured-in-place pipe rehabilitates city sewers. *Reinforced Plastics*, *45*(12), 36–38. https://doi.org/10.1016/S0034-3617(01)80415-X

[Yada 2008] Yada, H., Nagai, M., & Tanaka, K. (2008). Origin of the fast relaxation component of water and heavy water revealed by terahertz time-domain attenuated total reflection spectroscopy. *Chemical Physics Letters*, *464*(4-6), 166–170. https://doi.org/10.1016/j.cplett.2008.09.015

[Yang 1991] Yang, Y., & Suspene, L. (1991). Curing of unsaturated polyester resins: viscosity studies and simulations in pre-gel state. *Polymer Engineering and Science*. (31), 321–332.

[Yousef 2006] Yousef, M., & Nassar, R. (2006). Analysis of accelerated failure times of rehabilitation liners subjected to a constant or variable pressure. *Tunnelling and Underground Space Technology*, *21*(1), 97–105. https://doi.org/10.1016/j.tust.2005.04.003

[Zamanzade, Vehoff 2014] Zamanzade, M., Vehoff, H., & Barnoush, A. (2014). Cr effect on hydrogen embrittlement of Fe3Al-based iron aluminide intermetallics: Surface or bulk effect. *Acta Materialia*, *69*, 210–223. https://doi.org/10.1016/j.actamat.2014.01.042

[Zamanzade & Barnoush 2014] Zamanzade, M., & Barnoush, A. (2014). An Overview of the Hydrogen Embrittlement of Iron Aluminides. *Procedia Materials Science*, *3*, 2016–2023. https://doi.org/10.1016/j.mspro.2014.06.325

[Zhao 2005] Zhao, W., Nassar, R., & Hall, D. (2005). Design and reliability of pipeline rehabilitation liners. *Tunnelling and Underground Space Technology*, *20*(2), 203–212. https://doi.org/10.1016/j.tust.2004.07.002

[Zoughi 2000] Zoughi, R. (2000). *Microwave non-destructive testing and evaluation*. *Non-destructive evaluation series: Vol. 4*. Dordrecht: Kluwer Academic Publishers.

[Zoughi 1995] Zoughi, R., & Ganchev, S. (1995). *Microwave nondestructive evaluation: State-of-the-art review*. Austin: The Nondestructive Testing Information Analysis Center (NTIAC).

9 Appendix

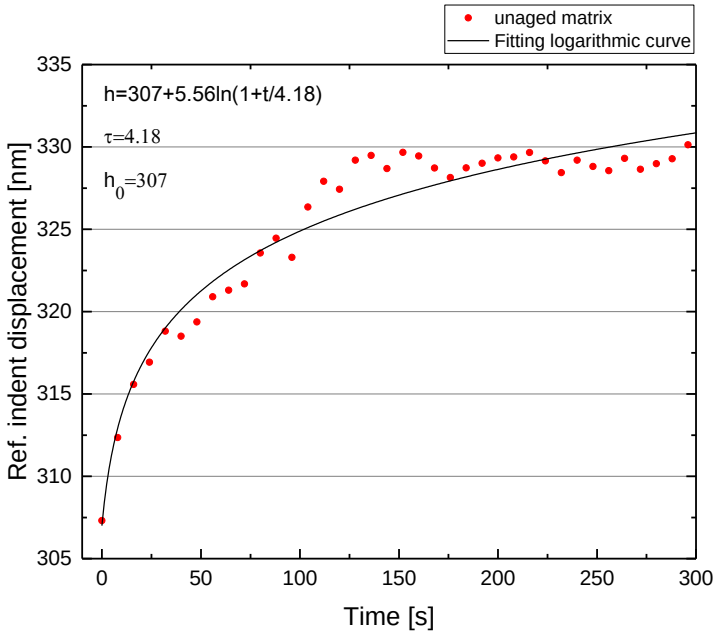

Fig. 98: Fitting logarithmic curve on ref. indent displacement vs. time test of unaged matrix

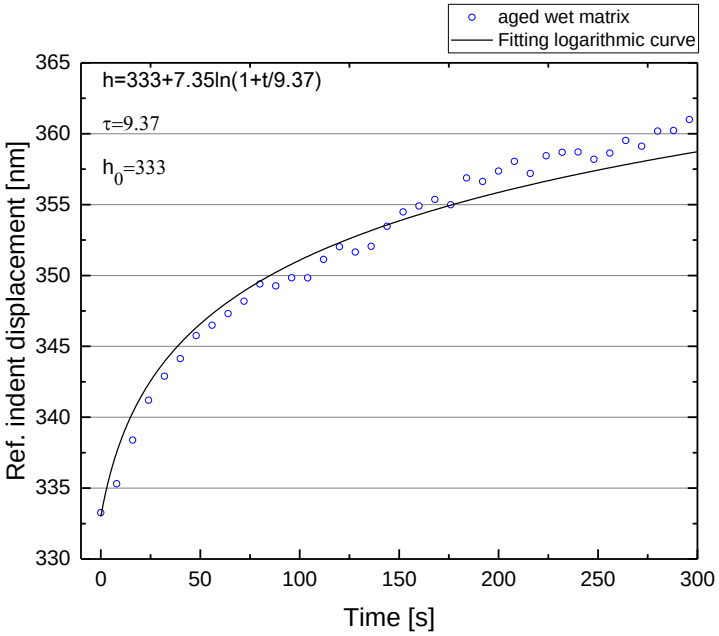

Fig. 99: Fitting logarithmic curve on ref. indent displacement vs. time test of aged wet matrix

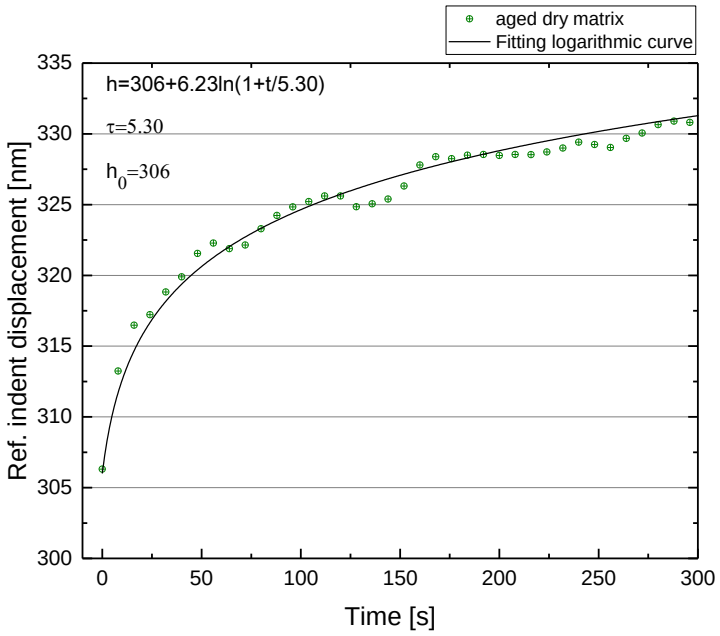

Fig. 100: Fitting logarithmic curve on ref. indent displacement vs. time test of aged dry matrix

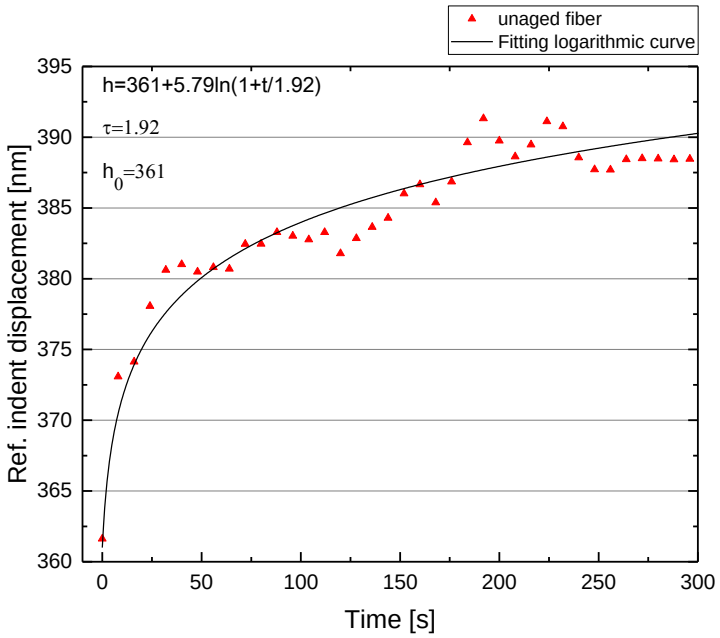

Fig. 101: Fitting logarithmic curve on ref. indent displacement vs. time test of unaged fiber

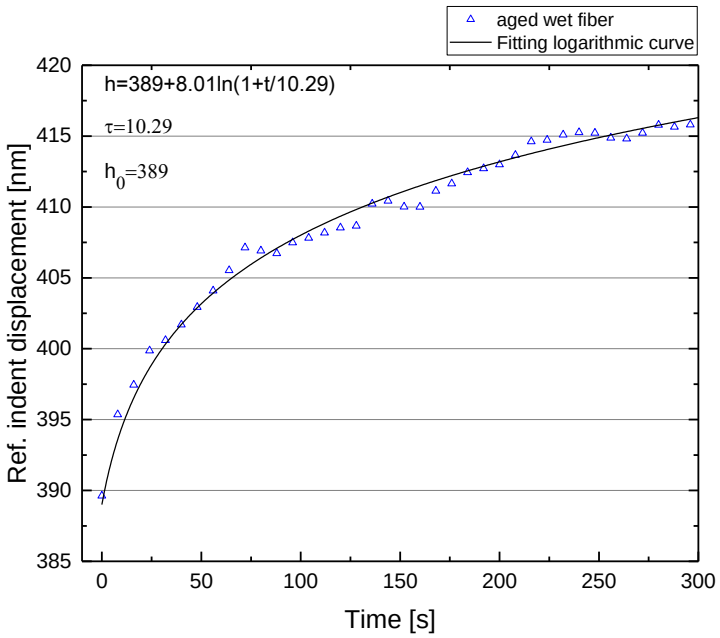

Fig. 102: Fitting logarithmic curve on ref. indent displacement vs. time test of aged wet fiber

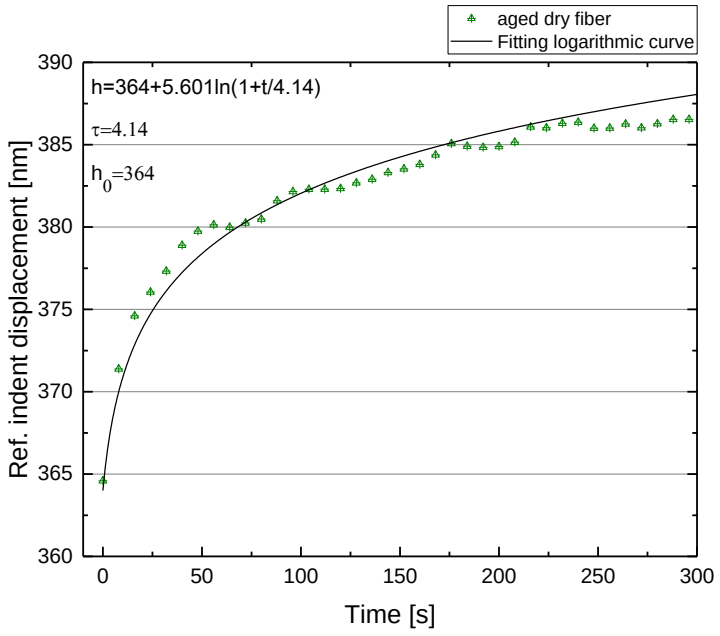

Fig. 103: Fitting logarithmic curve on ref. indent displacement vs. time test of aged dry fiber